# Al-Mukhtar Journal of Engineering Research

Voulme 8
Issue 1
DEC 2024

PUBLISHED BY : OMU

# Al-Mukhtar Journal of Engineering Research

**Peer-reviewed scientific journal, Volume Eight , Issue One, 2024**

**Published by Omar Al-Mukhtar University, Al-Bayda, Libya**

**Al-Mukhtar Journal of Engineering Research**

**5NL – LDN 281-201**



A peer-reviewed journal published by Omar Al-Mukhtar University, Al Bayda, Libya
Peer-reviewed scientific journal, Volume Eight , Issue One, 2024
Email: omu.j.eng@omu.edu.ly
To pour. Box 919 Al Bayda - Libya

# Al-Mukhtar Journal of Engineering Research 08: (1), 2024

Al-Mukhtar Journal of Engineering Research 08 (1): 01-10, 2024
Doi: https://doi.org/10.54172/ewrb3z72

Research Article

Open Access

# Design and Comparison of Symmetric Compensation Method for DWDM System and WDM by Using Optisystem

**Ali F. Kaeib [*], Lamia K. Amhimmed[2] , Sajeda J. Aldridi [3]**

***Corresponding author:** ali.kaeib@sabu.edu.ly Department of Electric and Electronic Engineering, Faculty of Engineering, Sabratha University, Libya.

[2] Department of Electric and Electronic Engineering, Faculty of Engineering, Sabratha University, Libya.

[3] Department of Electric and Electronic Engineering, Faculty of Engineering, Sabratha University, Libya.

**Received:**
09 October 2023

**Accepted:**
13 March 2024

**Publish online:**
31 December 2024

**Abstract**

Optical fibers are used in Wavelength Division Multiplexing (WDM) networks for transmitting data in the form of light pulses between the transmitter and the receiver. Multiple signals could potentially be transmitted at once using WDM systems. The light signals, however, lose strength as they move through the fiber over a significant distance. Therefore, to restore the original signal after a specific amount of time has passed since light propagation, all light signals must be amplified simultaneously. With increasing distance, the signal is exposed to less dispersion because of the employment of two different types of optical fibers, referred to as Dispersion fibers. The SMF type was enhanced with compensation fiber (DCF), and the outcomes of the two designs were contrasted to decide which is the greatest and most dependable. Using the Optisystem program, this study simulates a four-channel optical communication system and tests it at various distances to determine the ideal distance at which the most data may be communicated. Analysis of the data led to the calculation of crucial parameters such as the Q-factor, BER, and eye diagram, The results varied depending on the length of the cable and the rate of transmitted data.

**Keywords:** WDM, DWDM, DCF, Optisystem, BER, Q-Factor.

## INTRODUCTION

Because of several advantages such as low loss, cheap cost, easy amplification, low interference, and lightweight, optical fiber communication has been increasingly popular for long-distance data transport in recent years. A simple optical telecommunication system consists of a transmitter, a medium, and a receiver.

The optical network that applies wavelength division multiplexing (WDM) is currently widely used in existing telecommunication infrastructures and is expected to play a significant role in next-generation networks and the future Internet, Normal WDM, CWDM and DWDM are three types of WDM technology.

This paper then uses two types of these types: WDM and DWDM, where WDM can be created using a cable of the type SMF, but the transmission distance will be short. On the other hand, we can use DWDM, which can be created using DCF cable, which can transmit over long distances, almost twice the distance obtained on them using an SMF cable, so DWDM technology is better. (Vijayakumar, 2019)

## WAVELENGTH DIVISION MULTIPLEXING (WDM)

A wavelength division multiplexer (WDM), as demonstrated in figure 1 which is used in fiber-optic communications, is a different type of multiplexer. It's a technique for analog multiplexing. It's made for fiber cable with a high data rate capability. The communication channel's bandwidth should be bigger than the combined bandwidth of the different channels in this technique. Here, signals are transformed into light signals, which are then delivered across the same fiber connection with multiple wavelengths. (Vijayakumar, 2019)

WDM divides the optical fiber bandwidth into several no-overlapping optical wavelengths, which are referred to as WDM channels in the WDM transmission system. WDM combines and transmits all incoming signals with varied wavelengths over a single channel. A de-multiplexer reverses the process, separating the wavelengths. This multiplexing method increases the available transmission capacity significantly. (A.F. Kaeib, 2022)

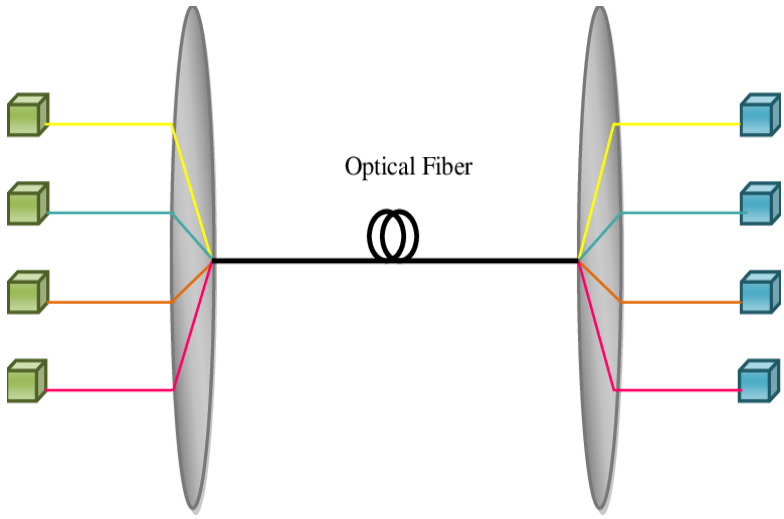


**Figure: (1)**. Wavelength-division multiplexing WDM (A.F. Kaeib, 2022)

## TYPES OF WDM

Today's WDM technology mostly falls into two categories:

### A. Coarse Wavelength Division Multiplexing (CWDM):

WDM systems with fewer than eight active wavelengths per fiber are referred to as CWDM. CWDM utilizes wide-range frequencies with widely separated wavelengths since it is employed for short-range communications. Standardized channel spacing allows for wavelength variation due to the operation-related heating and cooling of lasers. When spectral efficiency is not a crucial requirement, CWDM is a small and affordable solution. (Vijay akumar, 2019)

### B. Dense Wavelength Division Multiplexing (DWDM):

With its ultimate scalability and reach for fiber networks—establishing transport connections as short as tens of kilometers—DWDM is a form of WDM technique, an optical multiplexing technology used to improve bandwidth over existing fiber networks. WDM that uses closely spaced channels is known as dense WDM (A.F. Kaeib, 2022)

## CHARACTERISTIC OF AN OPTICAL FIBER

Signal attenuation is one of optical fiber's key characteristics. Another crucial characteristic of optical fiber is the distortion mechanism, which is also known as fiber loss or signal loss.

### A. Attenuation

As the light pulse moves from one end of the cable to the other, attenuation refers to a loss of light energy. It is also known as fiber loss or signal loss. It also determines how many repeaters thirty-six in total are needed between the transmitter and receiver. The cable's length is directly inversely correlated with attenuation. The ratio of optical output power to input power in a fiber of length L is known as attenuation (Bass, 2002)

$$\alpha = 10 * \log 10 \frac{Pi}{Po} [\ / km\ ] \ldots\ldots\ldots (1)$$

where:
α is the attenuation constant
$Pi$ : Input Power, $Po$: Output Power,
The cable's varied losses are caused by
• Absorption
• Bending Loss
• Scattering

### B. The dispersion

In an optical fiber, it is described as pulse spreading. A laser pulse broadens as it travels through a fiber due to factors like numerical aperture, core diameter, refractive index profile, wavelength, and laser line width. Along the fiber's length, dispersion grows. Inter-symbol Interference (ISI) refers to the overall impact of dispersion on a fiber optic system's performance. When dispersion-induced pulse spreading causes a system's output pulses to overlap, inter-symbol interference results. (Bass, 2002)

## DISPERSION COMPENSATION TECHNIQUES

These are the dispersion compensating methods that are most frequently used:

- Electronic dispersion compensation (EDC).
- Fiber Bragg Grating (FBG).
- Digital Filters.
- Dispersion Compensating Fibers (DCF).

## DISPERSION COMPENSATING FIBERS (DCF)

Dispersion compensating fibers (DCF) were first proposed as a method in 1980. Wide bandwidth and temperature do not readily alter the DCF component parts. One of the most used strategies for dispersion is DCF. A DCF is a fiber loop with a transmitting fiber's dispersion plus a negative amount. The terms pre-compensation, post-compensation, and symmetrical compensation can be used to describe it. It is the initial method of compensation for dispersion compensation. When the DCF is used between the amplifiers together with a combination of both ways called symmetrical compensation, this type of fiber can be used before the optical fiber called pre-compensation, or after the optical fiber called post-compensation. (Bass, 2002)

With single-mode fiber WDM systems that have high effective areas and low bit error rates, the DCF approach is frequently used. This is a very effective and dependable method, however, when the input power is high, it exhibits substantial insertion loss and nonlinear distortion. In addition to DCF, reverse dispersion fiber (RDF) and dispersion-managed cables (DM) are also used. (Vijay akumar, 2019)

## DISPERSION COMPENSATION FIBER ON A PATH

DCF, which reduces the positive dispersion of the transmission lines to make the residual dispersion zero, is one of the best ways to compensate for dispersion with tunable negative dispersion. By using the following equation to determine the length of the DCF, one can make the residual dispersion zero:

$$Dres = D_{TF} L_{TF} + D_{DCF} L_{DCF} \ldots\ldots (2)$$

Where $L_{TF}$ is the transmission length, $D_{DCF}$ is the negative dispersion of the DCF, $L_{DCF}$ is the length of the DCF compensator, and DTF stands for the positive dispersion of the transmission. The dispersion slope must also be corrected in order to account for the positive dispersion over a wide wavelength range. This is how the residual dispersion slope is written:

$$Sres = S_{TF} L_{TF} + S_{DCF} L_{DCF} \ldots. (3)$$

Where $S_{TF}$ is the transmission fiber's positive dispersion slope, $L_{TF}$ is the transmission length, SDCF is the DCF's negative dispersion slope, and $L_{DCF}$ is the DCF compensator's length. There are three alternative dispersion compensation approaches for DCF, as previously discussed. Post-compensation methods place the DCF after the Single Mode Fibre, while pre compensation schemes position the DCF on the side facing the EDFA amplifier. A pre-combination of and post-compensation employing DCF on both sides of a single-mode fibre (SMF) is known as symmetrical compensation . (Kaur, 2016).

## SYSTEM DESIGN AND SIMULATION

An optical communication system consists of three components: an optical transmitter, an optical receiver, communication channel, the following figure shows these components.

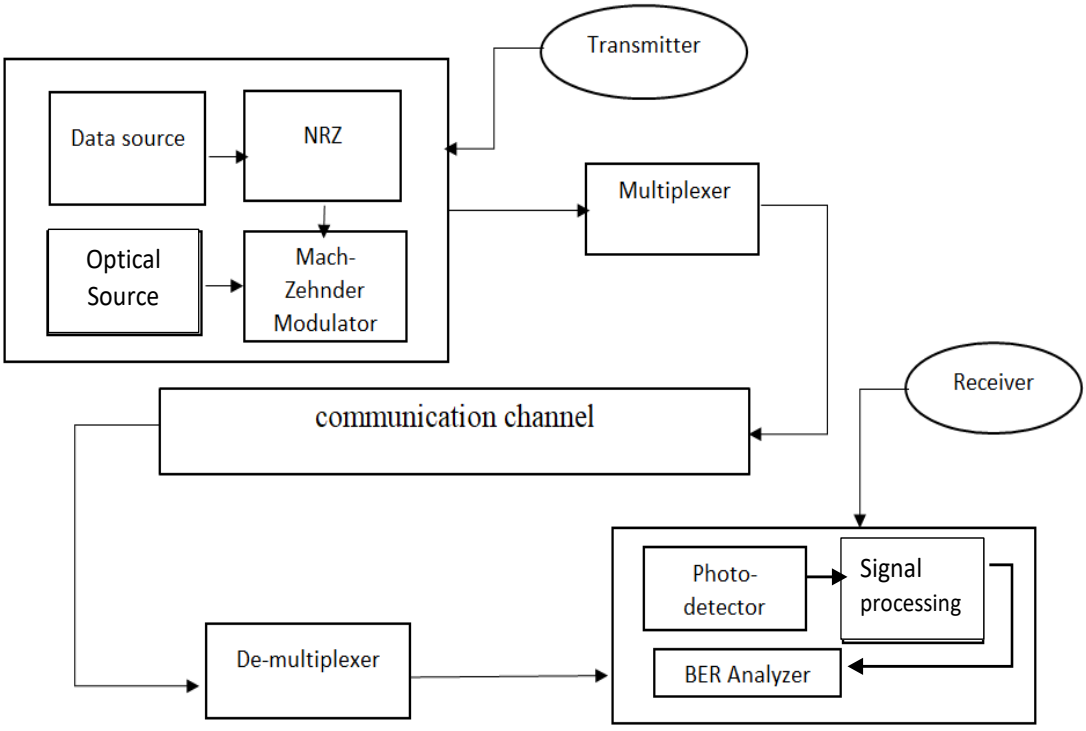


**Figure :(2).** Basic Optical System Components (Kaur, 2016)

### A. The transmitter

The optical transmitter's purpose is to transform an electrical input signal into the matching optical signal and then broadcast that signal across an optical fibre to another device. Table: (1) shows the transmitter's four parts: the data source, the pulse generator, the optical modulator, and the optical source. (Fauza Khair, 2018)

### B. The Communication channel

The communication channel's goal is to transmit information without distorting it. An information signal must travel through some kind of channel or medium to be transmitted over space. These "communication channels" can be broadly classified into directed and unguided pathways. Twisted-pair cable, coaxial cable, and fibre optic cable are examples of guided media. The unguided medium, free space, is unbounded and includes guided media. The unguided medium, free space, is unbounded and includes guided media such as microwave, satellite, radio, and infrared. In this project, the carrier is an optical signal that moves the optical signal from transmitter to receiver (Barry Elliott, 2002)

### A. The receiver:

The optical receiver is used to convert the optical signal received at the output end of the optical fiber back into the original electrical signal and recover the data transmitted through the light wave system. Its main components as shown in Figure (2) in addition to the BER analyzer are photodetector, and signal processing components as illustrated in Table (2).

**Table :(1)** Transmitting components

| Component name | Symbol | Function |
|---|---|---|
| CW laser |  | Generates optical signal which will be used as the optical carrier |
| Pseudo –Random Bit Sequence Generator |   | Generates a Pseude Random Binary Sequence (PRBS) according to different operation modes |
| NRZ pulse generator |  | Converts the binary input comes to it from the bit sequence generator into electrical pulses for modulation purposes |
| Mach-Zender modulator |  | Modulates the information signal with the optical carrier signal that comes from the light source . |

**Table :(2)** Receiving components

| Component name | Symbol | Function |
|---|---|---|
| Optical amplifier |  | Amplify the optical signal with pre-defined gain in the dB unit. |
| PIN photodetector |  | Converts the received optical signal into an electrical signal. |
| Low-pass filter |  | remove high-frequency noise and interference from the signal. |

The following figures display the circuit design.

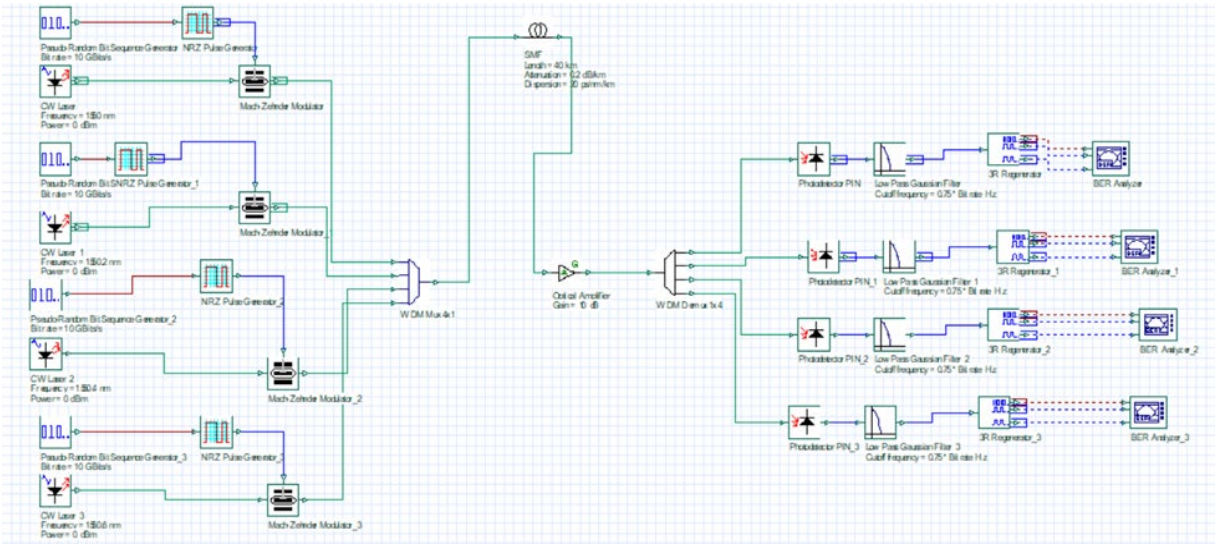

**Figure:(3).**system simulation scheme of SMF cable

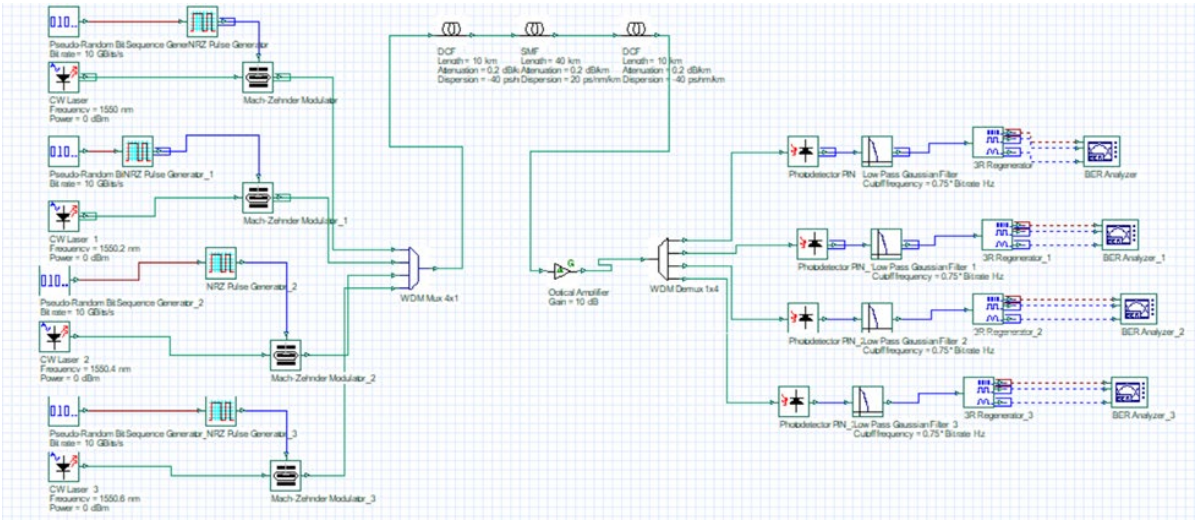

**Figure:(4).** System simulation scheme of SMF+DCF cables

The user can enter parameters that can be measured from actual equipment using the Optisystem program. To do this, double-click the component to bring up its associated parameters. Different parameters were utilized for the circuit depicted above; some of them vary based on each situation, while others will always be the same. The results table will include the variable parameters, while the constant parameters are an amplifier noise figure of 4 dB and a gain of 10 dB. The PIN photodetector will have a 1 A/W response rate and a 10 nA dark current. The low pass filter will have a depth of 100 dB and a cutoff frequency equal to 0.75 of the bitrate.

## RESULTS AND DISCUSSION

Using WDM and DWDM, various channel spacing characteristics were examined. These two scenarios are:
Case one WDM: The communication channel in this scenario is solely made up of Single Mode Fibre SMF and an amplifier EFDA, with no DCF.
Case two DWDM: Single Mode Fibre SMF, EFDA, and 2 -DCF are used as the communication route. In order to compare the two scenarios, examine the changes that take place when the DCF is added to the circuit's communication channel, and estimate the appropriate operating distance for the system, we will use two cases. The laser frequency values between 1550 and 1550.6 were set to four channels with a range of laser input power 2 dBm to 6 dB and varied bit rates 5 Gbit/s, 10 Gbit/s, and 15 Gbit/s and their efficacy was compared in terms of the distance to be covered.

The parameters of the fiber have been set as follows in Table (3):

**Table: (3)** Fiber parameters

| Parameter | DCF | SMF |
|---|---|---|
| Length | (25-60) km | (50-120) km |
| Attenuation | 0.2 dB/Km | 0.2dB/Km |
| Dispersion | -40 ps/nm/km | 20ps/nm/km |

The following tables illustrate the various bit error rates (BER) and Q factors at various distances when the communication channel is consisting of SMF+DCF with EFDA.

**Table : (4)** SMF results of the Q-factor and BER in 5Gbps and 6dbm

| Length (KM) | 5Gbps -6dbm | | | | | | | |
|---|---|---|---|---|---|---|---|---|
| | 1550 nm | | 1550.2nm | | 1550.4nm | | 1550.6nm | |
| SMF cable | Q Factor | BER | Q-Factor | BER | Q-Factor | BER | Q-Factor | BER |
| 30km | 12.351 | $1.901\times10^{-35}$ | 11.597 | $1.649\times10^{-31}$ | 12.016 | $1.124\times10^{-33}$ | 12.636 | $4.587\times10^{-37}$ |
| 50km | 9.303 | $5.674\times10^{-21}$ | 9.0452 | $6.141\times10^{-20}$ | 9.305 | $5.491\times10^{-21}$ | 9.694 | $1.1817\times10^{-22}$ |
| 80km | 4.327 | $7.555\times10^{-7}$ | 3.928 | $4.235\times10^{-5}$ | 3.997 | $3.175\times10^{-5}$ | 4.3762 | $5.945\times10^{-6}$ |

**Table: (5)** SMF results of the Q-factor and BER in 10 Gbps and 2dbm

| Length (KM) | SMF cable 10Gbps -2dbm | | | | | | | |
|---|---|---|---|---|---|---|---|---|
| | 1550 nm | | 1550.2nm | | 1550.4nm | | 1550.6nm | |
| SMF | Q Factor | BER | Q-Factor | BER | Q-Factor | BER | Q-Factor | BER |
| 30km | 8.15637 | $1.406\times10^{-16}$ | 7.1014 | $5.201\times10^{-13}$ | 8.1147 | $2.129\times10^{-16}$ | 7.54029 | $1.872\times10^{-14}$ |
| 50km | 5.9203 | $1.427\times10^{-9}$ | 4.98542 | $2.765\times10^{-7}$ | 5.61738 | $8.941\times10^{-9}$ | 5.5018 | $1.613\times10^{-8}$ |
| 80km | 3.835 | $5.896\times10^{-5}$ | 3.67728 | 0.0001116 | 3.43676 | 0.0002733 | 3.87003 | $5.251\times10^{-5}$ |

**Table: (6)** SMF+DCF results of the Q-factor and BER in 5Gbps and 2dbm

| Length (KM) | | 5Gbps-2dbm | | | | | | | |
|---|---|---|---|---|---|---|---|---|---|
| | | 1550 nm | | 1550.2nm | | 1550.4nm | | 1550.6nm | |
| SMF | DCF | Q-Factor | BER | Q-Factor | BER | Q-Factor | BER | Q-Factor | BER |
| 50 | 25 | 15.601 | $2.683\times10^{-55}$ | 14.948 | $5.858\times10^{-51}$ | 15.174 | $1.852\times10^{-52}$ | 16.226 | $1.07\times10^{-59}$ |
| 80 | 40 | 12.200 | $1.374\times10^{-34}$ | 11.624 | $1.322\times10^{-31}$ | 11.434 | $1.210\times10^{-30}$ | 11.479 | $6.886\times10^{-31}$ |
| 100 | 50 | 5.227 | $8.495\times10^{-8}$ | 4.991 | $2.928\times10^{-6}$ | 5.3281 | $4.920\times10^{-8}$ | 4.892 | $4.77\times10^{-7}$ |

The next figures show the eye diagram for the best and the worst result for 5Gp,10Gp bit rate with SMF cable only:

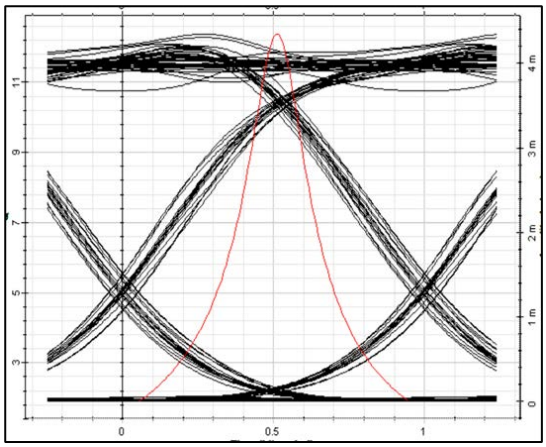

**Fig :(5)** eye diagram of the best result at 5Gpbs with SMF cable

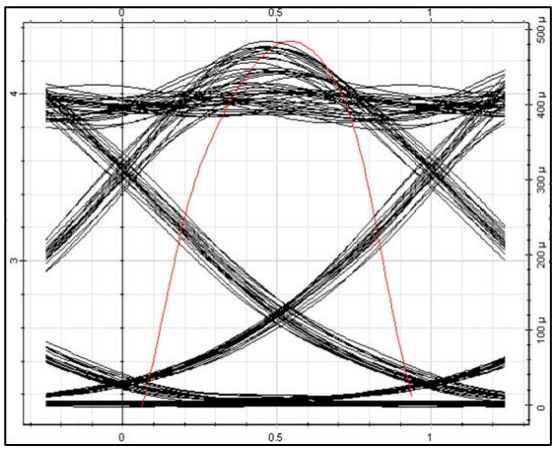

**Fig: (6)** eye diagram of the worst result at 5Gpbs with SMF cable

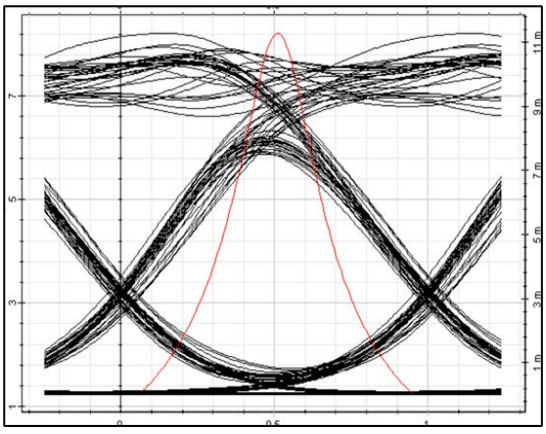

**Fig :(7)** eye diagram of the best result at 10Gp with SMF cable

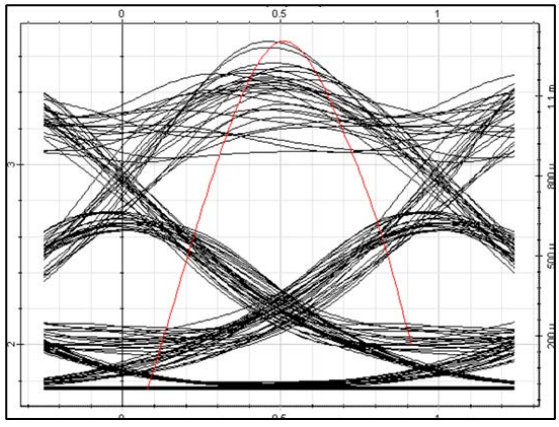

**Fig :(8)** eye diagram of the worst result at 10Gpbs with SMF cable

At a bit rate (15Gbps) The results were poor and the data transmission mechanism was inefficient. The system is clearly reliable up to 50 km, The best values of Q-FACTOR were at bit rates of 5

Gbps, and the bit rate 10 Gbps, the values of FACTOR somewhat fell, and at 15 Gbps, the Q-FACTOR was not excellent.

The next figures show the eye diagram for the best and the worst result for 5Gp,10Gp bit rate with SMF and DCF cables :

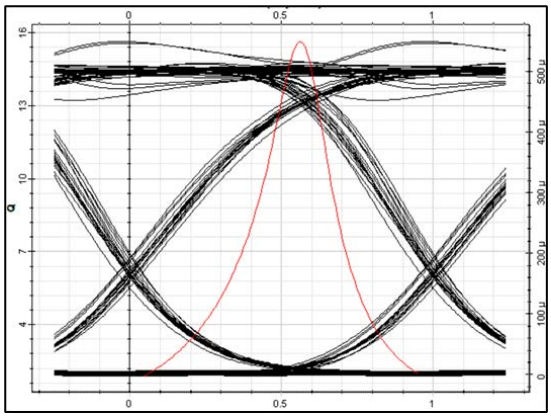

**Fig :(8)** eye diagram of the best result at 5Gbps with SMF+DCF cable

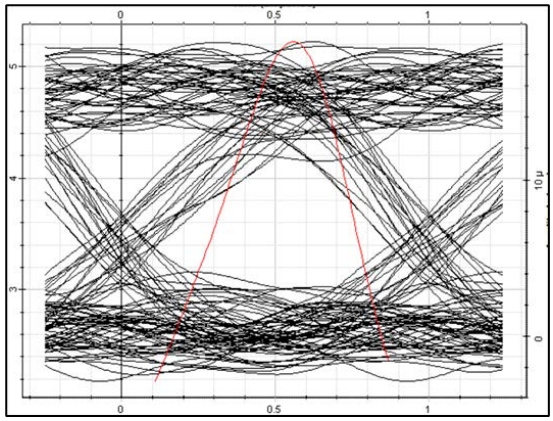

**Fig :(9)** eye diagram of the worst result at 5Gbps with SMF+DCF cable

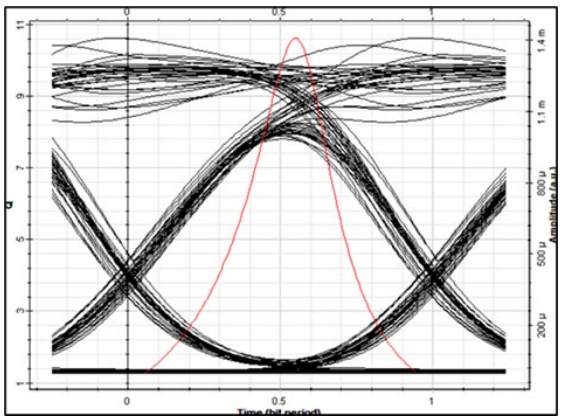

**Fig :(10)** eye diagram of the best result at 10Gbps with SMF+DCF cable

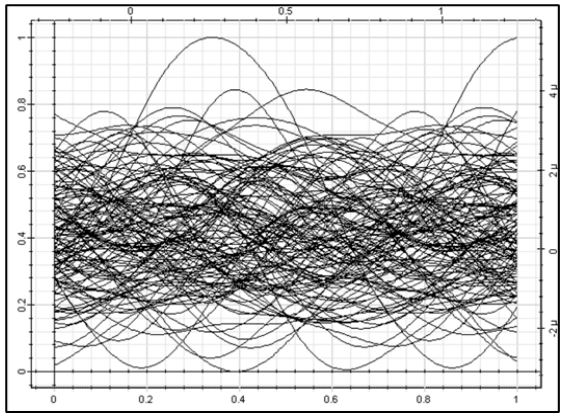

**Fig :(11)** eye diagram of the worst result at 10Gbps with SMF+DCF cab

At a bit rate (15Gbps), The results were poor and the data transmission mechanism was inefficient. Up to 150 km, the system exhibits a high degree of reliability. At bit rates of 5 Gbps, Q-FACTOR values were at their peak, and as bit rates rose to 10 Gbps, they started to decline considerably. However, at 15 Gbps, Q-FACTOR was not at all acceptable.

## CONCLUSION

The longest conceivable distance is examined in this paper. The two configurations were compared using different SMF lengths and DCF+SMF lengths, and it was discovered that the second configuration was more effective at transmitting data due to the presence of DCf, which serves as a dispersion compensation mechanism, as well as the presence of the second one when using a bit rate of 5Gbps. The configuration with only SMF is reliable up to 50 km, while the configuration with

DCF+SMF is reliable up to 150 km. When the wavelength varies within the same band, there is no difference in BER or Q-Factor.

**Duality of interest:** The authors declare that they have no duality of interest associated with this manuscript.

**Author contributions:** Contribution is equal between authors.

**Funding:** No specific funding was received for this work.

**REFERENCES**

A.F. Kaeib, O. A. (2022). Designing and Analysis of Underwater Optical Wireless communication system. *Designing and Analysis of Underwater Optical Wireless communication system, Department of Electric and Electronic Engineering, Faculty of Engineer 2022 IEEE 2nd International Maghreb* . Sabratha ,Libya : IEEE.

Abe, J. I. (2018, August). An In-Depth Analysis of Frequency Division Multiplexing, Time Division Multiplexing, and Time-Compression Multiplexing. Makurdi, Nigeria. Retrieved from https://www.academia.edu/38156174/MULTIPLEXING_FDM_TDM_AND_TCM_pdf

Barry Elliott, M. G. (2002). *Fiber Optic Cabling.* oxford: Newnes.

Bass, M. (2002). *FIBER OPTICS HANDBOOK, Fiber, Devices, and Systems for Optical Communications,.* United States of America: McGraw-Hill Professional.

Fauza Khair, I. W. (2018). Comparative Analysis of Dispersion Compensating Fiber in DWDM System Using . *International Conference on Information Technology* . Bali, Indonesia: IEEE.

Kahlon, N. K. (2014). "Various dispersion compensation techniques for optical system. *Open journal of communications and software 1.1* .

Kaur, K. a. (2016). Dispersion compensation techniques: A review. *An International Journal of Engineering Sciences, Special Issue 20*.

Vijayakumar, D. (2019). Retrieved from raserchgate: https://www.researchgate.net/publication/334056267_Multiplexing

Al-Mukhtar Journal of Engineering Research 08 (1): 11-26, 2024
Doi: https://doi.org/10.54172/fm5ryg72

Research Article Open Access

# Symbolic Regression for the Wall Effect on a Settling Sphere in a Circular Cylinder

**Husam A. Elghannay[1*] and Yousef M. F. El Hasadi[2]**

***Corresponding author:**
husam.elghannay@uob.edu.ly
Department of Mechanical Engineering, University of Benghazi, Benghazi, Libya

[2]Delft University of Technology, SX, Delft, the Netherlands.

**Received:**
13 January 2023

**Accepted:**
13 August 2023

**Publish online:**
31 December 2024

**Abstract**

The main contribution of the current paper is to provide symbolic regression-based correlations for the wall correction factor of a sphere settling in a static fluid confined in an infinitely long circular cylinder. The first correlation will be valid for the entire spectrum of the flow regimes that range from the creeping flow regime up to the turbulent flow regime. While the second correlation is compact and only valid in the creeping flow regime, it accurately reassembles Haberman and Sayre's complicated analytical formula (David Taylor Model Basin Report No. 1143, Washington, D. C, US Navy Dept, 1958). A review of the available data and correlations is made to justify the selection of the data used in generating the correlation. This is followed by feeding a representative data to a symbolic regression software, selecting a dependency of the parameter of interest, running the software and selecting a correlation that has a relatively small length with good accuracy among the resulting suggested formulas. We used a small volume of training data from experiments to feed the symbolic regression machine-learning algorithm. The developed formula compared reasonably well with the available data and can extrapolate beyond its training data range. For the correlation limited for the creeping flow regime, the training data was obtained by solving a set of equations that constitute the Haberman and Sayre analytical formula. The obtained expression compared well when compared to the exact solution.

**Keywords:** Wall effect; Machine learning; Symbolic regression; Sphere settling in a circular cylinder.

## INTRODUCTION

Analytical and experimental investigation of the motion of a moving sphere through otherwise quiescent fluid has been the subject of intensive research (Stokes 1851, Oseen 1910, Jones 1957, Satapathi 1960). Due to the sizable containers and tubes used, the experimental measurements are inevitably affected with the presence of a confining wall in many cases in which unbound fluid is assumed. When studying the drag on sphere in the presence of a confining wall it is found that the recirculatory wake formation is retarded along with the onset of separation (Clift, Grace et al. 1978). The fall velocity of a rigid sphere is retarded by the presence of confining walls as compared to the fall velocity at identical conditions in an unbound fluid (Chhabra 2006). The former observation is a consequence of the increase in the drag force felt by the falling sphere. Brown and Lawler (Brown and Lawler 2003) performed a detailed review of existing

experimental data on the drag force on rigid spheres, excluding data with large uncertainty. They applied a wall correction factor to some of the data and were able to confirm the theoretical solution of Stokes drag in the creeping flow regime.

There are three different definitions of the wall correction factor (Clift, Grace et al. 1978) the least common one of them is the ratio of a hypothetical viscosity to the actual viscosity of the fluid. The hypothetical viscosity assumes Stokes flow and uses the observed terminal viscosity. The former definition is found convenient to use in falling ball viscometry (Clift, Grace et al. 1978, Singh, Sharma et al. 2012). The second definition is the ratio of the drag coefficient of a single settling sphere in bounded fluid to the drag coefficient in infinite medium at identical conditions. The third wall correction factor definition is the ratio of the terminal velocity at bounded fluid to the terminal velocity of the same particle at unbounded fluid. The three wall correction coefficients are the same at low Reynolds numbers (creeping flow)(Clift, Grace et al. 1978). As compared to the other two definitions, the velocity ratio is more extensively studied because it is a simpler and more convenient parameter to look at [12]. Most of the experimental literature is focused towards the velocity correction factor (e.g. (Fidleris and Whitmore 1961, Uhlherr and Chhabra 1995, Kehlenbeck and Felice 1999)). So the current paper considers seeking a correlation for the velocity correction factor. Theoretically derived formulas for wall correction factor at the creeping regime are only a function of the ratio of the diameter of the sphere to the diameter of the cylinder ($\lambda=d/D$).

In the creeping flow regime there exist a number of experimentally and theoretically developed formulas which vary significantly as the diameter ratio increases as indicated by Iwaoka and Ishii (IWAOKA and ISHII 1979). Nevertheless, the limit at which the viscous regime ends is not quite obvious (Haberman and Sayre 1958, Clift, Grace et al. 1978, Chhabra, Agarwal et al. 2003) and may not extend to measureable/practical values. It is accepted that there will be dependency on Reynolds number beyond the creeping flow regime (Oseen 1910). It worth noting that Reynolds number used in the formulas is based on the diameter of the sphere and the terminal velocity of the sphere at unbound fluid conditions rather than the existing terminal velocity when bounding wall exists. Fidleris and Whitmore (Fidleris and Whitmore 1961) and later Uhleherr and Chhabra (Uhlherr and Chhabra 1995) presented their correction factor in graphical format which is not practical to use. Based on computational experiments Wham et al. (Wham, Basaran et al. 1996) developed a drag correction factor formula that is applicable for $Re \leq 200$ and diameter ratios of $\lambda \leq 0.7$. The suggested model recovers the theoretical solution of Heaberman and Sayre as Re gets smaller. Chhabra et al. (Chhabra, Agarwal et al. 2003) rewrote the Wham's formula in terms of a velocity coefficient formula, but the resulting formulation is implicit and not practical to use. Di Felice (Di Felice, Gibilaro et al. 1995) and later Kehlenbeck and De Flice (Kehlenbeck and Felice 1999) proposed alternative empirical correlations for the intermediate regime, with the latter being more complex and more accurate (Chhabra, Agarwal et al. 2003).

At the fully turbulent regime many researchers suggest that the correction factor becomes again independent of Reynolds number. Uhleherr and Chbbrah suggest that the wall correction factor becomes independent of Re as Re exceeds 1000 (Uhlherr and Chhabra 1995). Similar to the creeping flow regime, Many formulas are derived for the high Reynolds number regime and they show notable differences (Uhlherr and Chhabra 1995). In fact some of the correlations are based on very limited data points (<10 data points) (Uhlherr and Chhabra 1995).

In general the wall correction factor is higher in the viscous regime than at higher Reynolds numbers. Chhabra et al. (Chhabra, Agarwal et al. 2003) suggests that "*It is generally agreed that the wall factor is independent of the Reynolds number both at very low and at very high values of the Reynolds number, while in between these two limiting behaviors, the wall factor is a function of both $\lambda$ and Re in the intermediate transition regime*".

There are various correlations describing the wall effect, but they are scattered and inconsistent (IWAOKA and ISHII 1979, Chhabra, Agarwal et al. 2003). There is an opportunity to develop a new correlation using symbolic regression machine learning method. We propose that a generic function should depend on the diameter to wall ratio and the Reynolds number. This function can be developed in a similar way to the methods described in (Barati, Neyshabouri et al. 2014, El Hasadi and Padding 2019, El Hasadi and Padding 2023). Barati et al. (Barati, Neyshabouri et al. 2014) used symbolic regression to closely match almost all experimental data for the drag coefficient of a sphere for case of unbounded sphere. While, El Hasadi and Padding (El Hasadi and Padding 2023) used symbolic regression to investigate the underlying physics of the same problem. Li et al. (Li, Zhang et al. 2014), generated a generic formula of the wall correction factor for particles with different shapes settling in a cylindrical container filled with different medias (Newtonian and various non-Newtonian fluids) using artificial intelligence. The total number of experiments used to generate the generic formula was 513. Li et al. also worked on generating a wall correction factor of a sphere settling in a Newtonian fluid using a subset of their collected data. The generic model had only 55.5% of the data within 5% of uncertainty and 86% within 15% of uncertainty. The sphere in Newtonian fluid wall correction formula was found to have 99.4 % of the data within 5% of uncertainty. Although the sphere in a Newtonian fluid wall correction correlation is -thus- quite promising, no explicit formula is provided in the paper possibly because of the complicated form.

The main objectives of this paper are as follows:

- We aim to develop a generic correlation that depends on both $\lambda$ and Reynolds number and covers all flow regimes. The selection of the data used to train the symbolic regression algorithm is described in the next section.
- We aim to find a simpler formula that accurately represents the exact solution of the problem in the viscous flow regime.

In the next section, we review the most common expressions in all flow regimes, with emphasis of available correlations in the intermediate regime. This is followed by a comparison of experimental data in the intermediate flow regime to each other, as well as to existing correlations. In the results section, we provide an evaluation of the performance of the generated correlation. The results section also includes a brief overview of the method we used to reproduce the exact solution of Haberman and Sayre, which we used to generate data for our symbolic regression machine learning algorithm.

## MATERIALS AND METHODS

Recent reviews of the existing correlations that have been developed to estimate the drag coefficient can be found in (Chhabra, Agarwal et al. 2003, Arsenijević, Grbavčić et al. 2010, Singh, Sharma et al. 2012). Based on their extensive review of the bulk of the experimental work on the wall effect and its range of applicability, Chhabra et al. (Chhabra, Agarwal et al. 2003) recommended the use of the Haberman and Sayre equation (Haberman and Sayre 1958) in the

viscous regime, the Di Felice equation (Di Felice 1996) for the intermediate regime, and the Newton equation (Barr 1931) for the turbulent regime. The aforementioned equations, which describe each flow regime, are listed below. This is followed by a review of all previous efforts to correlate the wall correction factor in the intermediate regime Haberman and Sayre tabulated values of their –theoretically derived- analytical solution for λ values ranging from 0 - 0.8 with an increment of 0.1. Moreover, they provided an approximate solution which takes the following form:

$$K_v = \frac{1-0.75857\lambda^5}{1-2.105\lambda+2.0865\lambda^3-1.7068\lambda^5+0.72603\lambda^6} \quad (1)$$

Which is close enough to their exact analysis for up to λ =0.5. Numerical investigation by Bowen and Sharif (Bowen and Sharif 1994) found that the above formula to agree with numerical experiments data for up to λ =0.8 while Wham et al. (Wham, Basaran et al. 1996) found the agreement with the expression to extend for up to λ =0.5. Simulations performed by Tullock et al. (Tullock, Phan Thien et al. 1992) and Higdon and Muldowney (Higdon and Muldowney 1995) almost matched the exact analysis of Haberman and Sayre for up to λ=0.8.

Differences between Haberman and Sayre's expression with earlier analysis made by Ladenburg (Ladenburg 1907), and Faxen are almost identical. The superiority of HS solution comes from the wider applicability limits which extends much further than previous analysis (Haberman and Sayre 1958, Clift, Grace et al. 1978). The formula applicability limit also exceeds the theoretical analysis of Bohlin (Bohlin 1960) whom extended the original analysis of Faxen to formulate a more accurate expression for the wall correction factor (Bohlin 1960, Happel, Brenner et al. 1983).

Newton developed a semi-empirical formula (Barr 1931, Chandrasekhar 2003) for the fully turbulent flow regime can be expressed as:

$$K_v = (1-\lambda^2)(1-0.5\lambda^2)^{0.5} \quad (2)$$

However, Bougas and Stamatoudis (Bougas and Stamatoudis 1993) investigation of the transient behavior of settling spheres at high Reynolds number found Munore's (Munroe 1889) formula to have better agreement as compared to other proposed correlations. Monroe's formula takes the form:

$$K_v = (1-\lambda)^{3/2} \quad (3)$$

Bougas and Stamatoudis (Bougas and Stamatoudis 1993) applied Munore's (Munroe 1889) formula to their experimental work range ($0.11 \leq \lambda \leq 0.83$) and found a good agreement with the for values of λ up to 0.7 and Reynolds numbers ranging between 13500 - 70000.

**Data and Correlations at Intermediate Regime**

While many correlations exist in creeping flow and turbulent flow regimes, there is, however, a very limited attempts to find a correlation that covers the intermediate regime. Fidleres and Whitemore (Fidleris and Whitmore 1959, Fidleris and Whitmore 1961) pioneered the efforts to develop a correlation of the wall correction factor at intermediate regime as early as of late 50s of the last century but provided their results in graphical format. Their experimental data includes about 3000 experiments that covers a regime of Re ranging from 0.054 to 20000. Uhleherr and Chhabra (Uhlherr and Chhabra 1995) performed more than 220 experiments that covers almost the same Re range as of Fidleris and Whitmore. Their experimental results were

summarized in a graphical format and was found to be systematically higher than Fidleris and Whitmore but they are within the experimental uncertainty. The deviation with other correlations ranged between good agreement and up to 70% difference with no clear trend of the discrepancy. De Flice (Di Felice 1996) provided a correlation that has Re dependency and later Kehlenbeck and Di Flice (Kehlenbeck and Felice 1999) improved the correlation of De Flice (Di Felice 1996) in which two fitting parameters are introduced and estimated from the available experimental data from the literature along with their own experimental measurements. The improved correlation includes the use of two fitting parameters and can be summarized as follows:

$$K_v = \frac{1-\lambda^p}{1-(\lambda/\lambda_o)^p} \quad (4)$$

Where the first fitting ($\lambda_o$) parameter is found to have the following Re dependency

$$\frac{\lambda_o - 0.283}{1.2-\lambda_o} = 0.041Re^{0.524} \quad (5)$$

And the second fitting parameter ($p$) has the following Re dependencies

$$p = 1.44 + 0.5466Re^{0.434}, Re \leq 35 \quad (6a)$$

$$p = 2.4 + 37.3Re^{-0.8685}, Re \geq 35 \quad (6b)$$

Figure 1 presents the change of both fitting coefficients as Re changes (Eqs. (5 and 6)). Neither a physical interpretation of both coefficients was provided nor the significance of the assumed threshold of Re=35 was discussed in the paper. Although an alternative model in which an average value of p=2.2 was provided along with an optimized dependency of Re, the original model presented above agrees better with the experiments and will only be considered in the current work.

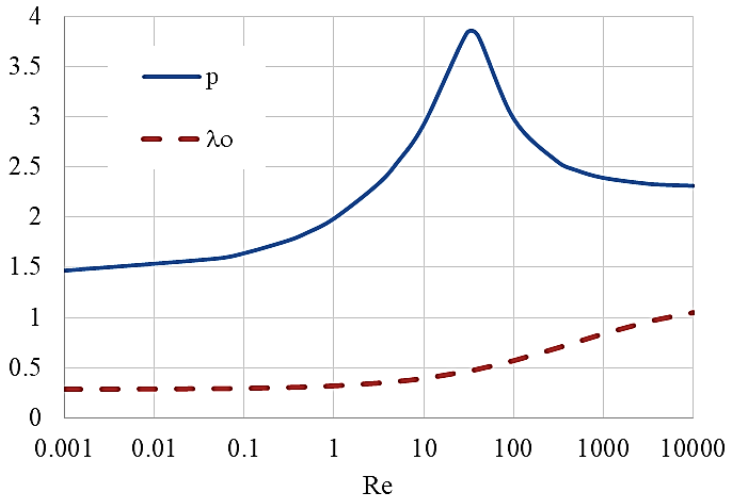


**Figure (1).** Graphical representation of fitting parameters used in Di Flice & Kehlenbeck correlation (Eqs. (5&6))

Figure 2 show the variation of the inverse of the velocity correction factor ($Kv^{-1}$) at different Re values. The solid lines are extracted from of Fidleris and Whitmore (FW) data along mapped

with both Uhleherr and Chhabrah (UC) graphical results and Kehlenbeck and Di Flice (KD) correlation. The lines of Fidleris and Whitmore (solid) along Kehlenbeck and Di Flice correlation (dash-dot) with are –from top to bottom - at $\lambda$ values of 0.05, 0.1, 0.2, 0.3, 0.4, 0.5 and 0.6 While those of Uhleherr and Chhabrah (dashed lines) are at $\lambda$ values of 0.2-0.5 at an increment of 0.1. Both Haberman and Sayre "exact solution" (HS) and Newton's formula are shown as limiting cases as diamonds and triangles respectively. The creeping flow limit was assigned to a Reynolds number of 0.004 whereas the turbulent flow limit of Newton is assumed at a Reynolds number of 20000.

Interestingly the graphical representation from Uhleherr and Chhabra are only qualitatively similar to those of Fidleris and Whitmore. Although FW data is made at about the same time as the theoretical solution of Haberman and Sayre they show very good agreement at low Reynolds number. The agreement is also good at the fully turbulent regime limit when assuming Newton's formula to be applicable at Reynolds number of 20000. Fidleris and Whitmore (Fidleris and Whitmore 1961) stated that *"Newton's equation increases in reliability when the highest Reynolds numbers reached in the experiments, which were about 10000, are approached"*.

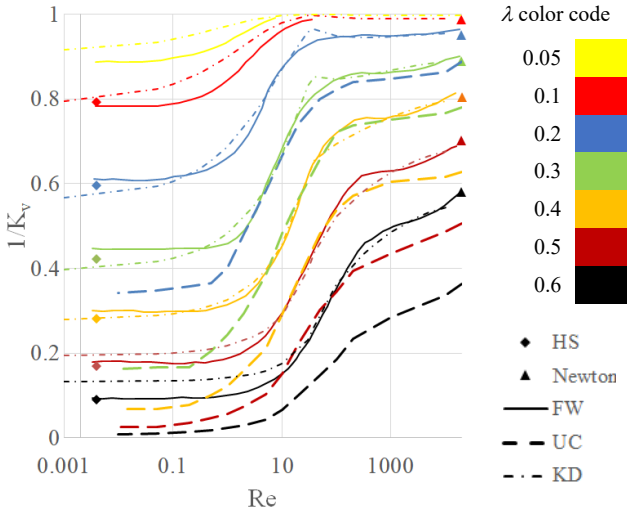


**Figure (2).** Graphical representation of data and correlations at intermediate regimes along with limiting formulas at creeping (Haberman & Sayre) and fully turbulent (Newton) regimes

Although the graphical representation of Fidleris and Whitmore show Re values of ~0.002 or so the smallest Re reported in the experiment is 0.054 so we suggest that F&W has extrapolated their plots a somewhat outside their experimental region. They assumed no further change with Reynolds number when extending their lines, however, by doing so there is a mismatch with the exact solution at most of the data points. On the other hand, Newton's formula agrees with the obtained trends at Re ~20000. If the trends would continue for another order of magnitude, chances are that even Newton's formula will lose its accuracy. In their investigation, Chhabra et al. (Chhabra, Agarwal et al. 2003) found the previously published data of (Uhlherr and Chhabra 1995) not to correlate well with the available empirical formulas at the intermediate flow regime. The justification was about the influence of non-verticality of the cylinder. Besides uncertainties that come from measurement of the different parameters, we suggest other experimental reasons such as sphericity, eccentricity between the sphere center and the cylinder center, estimating the

terminal velocity would contribute to the error in the experimental data. If –for some reason- the sphere starts to rotate them the error would be exaggerated

Kehlenbeck and Di Felice (Kehlenbeck and Felice 1999) formula agrees with Newton's formula of the fully turbulent flow regime. However, the agreement with Haberman and Sayre is not guaranteed for all values of λ. This can be noticed at λ values of 0.6 where the prediction stalls at a higher value of $K_v^{-1}$ (thus under predicts the wall correction factor) and goes below the Haberman and Sayre solution of $K_v^{-1}$ (over predicting) for λ value of 0.3 and less. The hump at Re=35 at λ values of 0.3 and 0.2 are an artifact of the behavior of the parameter *p* as shown in Figure 1.

Care should be taken when considering the data to be fed to the software since some of the data may has higher uncertainties when the diameter ratio goes to 0.9 (Chhabra, Agarwal et al. 2003). The data from Uhleherr and Chhabra (Uhlherr and Chhabra 1995) should thus not be considered due to the possible high uncertainty involved in it. The experimental data of Fidleris and Whitemore (Fidleris and Whitmore 1961) is to be used by itself to develop the correlation. In spite of some mismatch with the exact solution of Heaberman and Sayre at some λ values, the correlation of Kehlenbeck and Di Felice (Kehlenbeck and Felice 1999) has reasonably good agreement with Fidleris and Whimore (Fidleris and Whitmore 1961) data. Generating a data from Kehlenbeck and Di Felice is not an option to avoid confusing the process by inclusion of different sources of error. Data from numerical simulations which does not cover a wide range of flow regime (e.g., [10, 11]) are also excluded.

**Analysis software**

The regression is to be carried-out using the Demo version of TuringBot symbolic regression software. The Demo version limits the number of data points to 50 and the number of columns to three (so that a variable can only be a function of other two parameters). The software lists a number of possible fitting functions (starting from a bare average) and provide their accuracy based on selected parameters (the default is the rms value of the target parameter). The software keeps refining –sometimes replacing- the existing formulas and producing more accurate functions until the user decides to stop it. The software allows for shuffling the data and selecting the Test/Train ratios. TuringBot interface allows for visualization of the different suggested solutions and how they fit the original data.

## RESULTS

Here we present the regression formula obtained by the software and how it compares to the fed data and how it extrapolates outside the test/train regime. First, we seek a generic formula that properly describes the wall correction factor for viscous, inertia and extends to fully turbulent regime. Our goal is to find a functional dependency of the form $K_v=\phi(Re, \lambda)$. In the second section we will obtain a simple formula that is valid for the creeping flow regime using the training data from Haberman and Sayre's exact solution $HS=f(\lambda)$.

**Generic Formula**

In this part we seek a regression formula based on the graphical representation provided by Fidleris and Witmore (Fidleris and Whitmore 1961) and compare it with other available published data. Fidleris and Whitmore tabulated a small set of data (31 data points for Re of 0.1,

100, 1000, 3000, 10000) so we added some points from Kehlenbeck and De Flice at Re=10. Although the data is yet a small set we suggest that having the same systematic error –if any- would be more advantageous than using larger sets of different types of uncertainties. Fidleris and Whitemore provided their data for up to λ=0.6 thus there is a chance to judge correlations based on how they extrapolate when λ approaches 1 ($K_v{}^{-1}$ should go to zero).
Among many formulas generated by the software we select the following Equation

$$K_v{}^{-1} = (1-\lambda)^{\frac{1.3873}{0.7088+\emptyset}+1.1167\lambda} \qquad (7a)$$

where:

$$\emptyset = \left(-0.0542 + \frac{0.052}{\lambda}\right) \times (-0.2726 + Re)$$

is selected because simpler equations are not so accurate and more complicated functions are not encouraging for use because of their length and complexity. Eq. (7a) was obtained when all the data was used in the training with no data used in testing. This is because the sample of data point is limited especially when considering three parameters. Other functions were found to extrapolate poorly outside the training regime. As λ →1 (λ>0.95) Eq. (7a) has a singularity around Reynolds number of 1000 and was found to under-predict the correction factor at very low Reynolds numbers (Re → 0). Eq. (7a) has a good prediction for up to λ ~0.9 and may benefit from some refinement. By heuristic rounding of the coefficients of Eq. (7a) a modified version which gives almost the same prediction can be written as:

$$K_v{}^{-1} = (1-\lambda)^{\frac{1.4042}{0.7071+f}+1.1167\lambda} \qquad (7b)$$

where

$$f = \left(-0.053 + \left(\frac{0.053}{\lambda}\right)\right) \times Re$$

Figure 3 provides a comparison between the graphical representations of FW data with the current predictions of the current correlations (Eqs. (7a & 7b)). The mismatch between the data which was used and the digitized plot of FW data is because Fidleris and Whitmore's data is averaged between two different plots of $K_v$ and $K_v^{-1}$. We recommend not following the same strategy when looking at FW data but excluding the figure that show $K_v$ since it uses a logarithmic axis and will be more sensitive to inaccuracies when extracting the data. In fact Brown and Lawler (Brown and Lawler 2003) followed the same recommended strategy when correcting the drag on sphere data. In addition to that the HS exact solution is plotted (assumed at Re=0.004) as solid diamonds, and Newton solution at Re=20000 as solid triangles. Both HS and Newton solution are shown at λ values of 0.1-0.6 (color code is the same as in Figure 2). As can be noted from Figure 3, a quite good agreement is obtained in the tested regime ($\lambda$ up to 0.6). If there are any pitfalls, they would be that it misses Newton's formula at Re of 20000 at $\lambda$=0.6 and $\lambda$=0.5. The function fails to show the Re dependencies which are there is the experiment at Re>1000. Also, the exact solution at $\lambda$ =0.1 is also missed at very low Re but agrees with the graphical presentation of Fidleris and Whitemore which is used in the training process. In spite of the very careful set up of the experiment and the low uncertainty reported by Fileris and Whitemore (Fidleris and Whitmore 1959) we suggest that there is an error involved in the experimental results at this λ value.

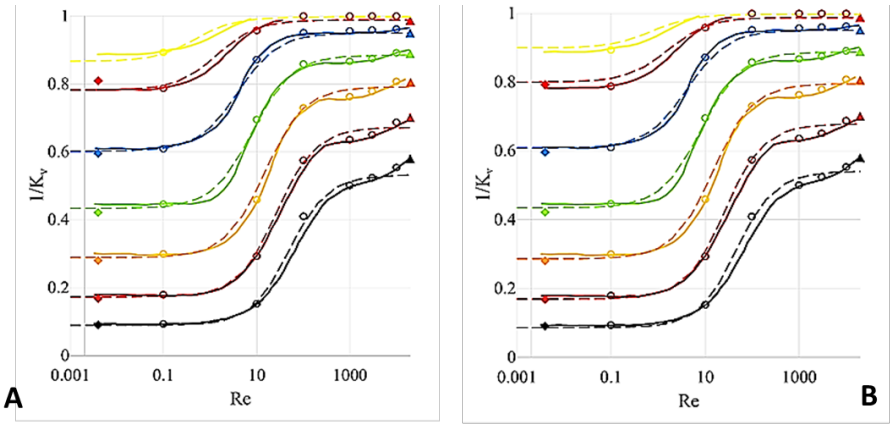


**Figure (3).** Agreement between the graphical representation of FW data along with limiting formulas at creeping (HS) and fully turbulent (Newton) regimes with (a) Eq. (7a) (b) Eq. (7b)

The only notable differences between Eqs. (7a) and (7b) are at low diameter ratios ($\lambda \leq 0.1$). In fact while the creeping flow limit of the inverse of the correction factor have been missed by both FW data and Eq. (7a), Eq. (7b) seem to be converging to the desired values as Re further reduced. The predictions of both Eqs. (7a) and (7b) are almost indistinguishable and only Eq. (7b) will be considered in further comparisons. Figure 4 provides a comparison of the predictions of Eq. (7b) at $\lambda$ value outside the training regime ($\lambda$>0.6). Eqn. (7b) gives reasonably good agreement as it goes to zero. The data diverts from Newton's formula. The deviation from Newtons' formula is because the experimental data used in generating the formula seemingly departs from Newton's formula as $\lambda$ extrapolates beyond $\lambda$=0.6. Further increase of Re beyond 10000 doesn't show a notable change in the predictions.

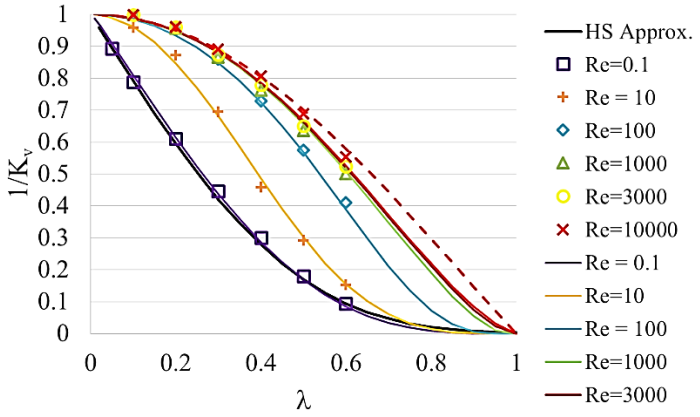


**Figure (4).** Predictions of Eq. (7b) at different diameter ratios.

So when excluding Reynolds numbers the only seen $\lambda$-terms that may appear in the exact solution–based on Eq. (7b) – would have the form of $\lambda$ and (1- $\lambda$). At very low Reynolds numbers equation (7b) can be approximated as:

$$K_v^{-1} = (1-\lambda)^{2.147+1.1167\lambda} \qquad (8)$$

The other limiting behavior at very high Reynolds numbers is given by the current formula:

$$K_v^{-1} = (1-\lambda)^{1.1167\lambda} \qquad (9)$$

A comparison of Eq. (8) with both Newton and Monrue's formulas (inverse of Eqs. 2 & 3 respectively) is provided in Figure 5. As can be seen Monure's predections are lower than predicted by Newton's formula since they might be based on experimental work that is possibly at higher Reynolds numbers than those of Newton. The current correlation is in better agreement with Newton's formula for up to λ=0.5 where it approaches Monrue's formula for up to λ=0.7. Beyond λ=0.8 both Newton and Monrue's predictions are about the same and both predicting a lower resistance by the wall than the current formula.

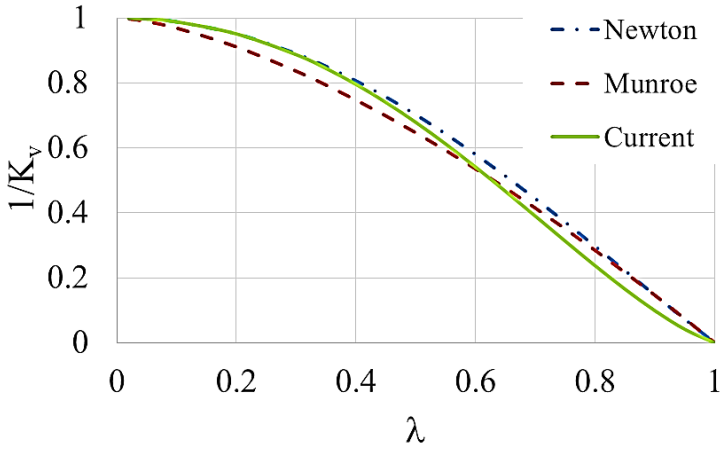


**Figure (5).** Comparison of limiting behavior of Eq. (9) with Newton and Monroe's formulas

**Alternate expression for the Haberman and Sayre's exact solution**

The suggested way of getting an alternative formula to the exact formula of Haberman and Sayre (Haberman and Sayre 1958) is to generate a large number of data from the exact solution itself. This means we should be able to solve the complicated exact solution, generate a large amount of data then feed it to the machine learning software to come-up with a simple formula.

Haberman and Sayre's (Haberman and Sayre 1958) solution is based on solving the Stokes stream function of a steady incompressible axisymmetric fluid in both cylindrical and spherical coordinates. Boundary conditions are applied to both solutions and the solution constants are relationship between the constants are obtained by direct comparison of terms. A linear algebraic system of equation is then constructed to obtain the constants. For the motion of a rigid sphere in a stationary liquid, the resulting system takes the form:

$$\begin{aligned}
&\frac{(2n-1)(n!)}{4(2n-3)}\frac{b_{n-2}}{R^{n-1}}\pi + \frac{n(n-1)(n!)}{4}\frac{b_n}{R^{n+1}}\pi \\
&+\sum_{m=0,2,\ldots}^{\infty}\left[\frac{1}{(n-2)!}S_3^{n+m-1} + \frac{n(n-1)}{(n-2)!\,(2n-3)}S_4^{n+m-2}\right]\frac{b_m}{R^{m+1}}\lambda^{n+m-1} \\
&+\frac{(2n+1)(n!)}{4}\frac{a_{n-1}}{R^{n+1}}\pi \\
&+\sum_{m=1,3,\ldots}^{\infty}\left[\frac{-1}{(n-2)!}S_4^{n+m-1} + \frac{1}{(n-4)!\,(2n-3)}S_2^{n+m-2}\right]\frac{a_m}{R^{m+2}}\lambda^{n+m} = \alpha
\end{aligned} \qquad (10a)$$

Where R is the radius of the cylinder and the parameters S are integrals of combinations of

$$\frac{n!}{4}\frac{b_{n-2}}{R^{n-1}}\pi+\frac{(2n-1)n(n-1)(n!)}{4(2n+1)}\frac{b_n}{R^{n+1}}\pi-\sum_{m=0,2,\dots}^{\infty}\left[\frac{S_4^{n+m}}{(n-2)!\,(2n+1)}\right]\frac{b_m}{R^{m+1}}\lambda^{n+m-1}$$
$$+\frac{(2n-1)(n!)}{4}\frac{a_{n-1}}{R^{n+1}}\pi-\sum_{m=1,3,\dots}^{\infty}\left[\frac{S_2^{n+m}}{(n-2)!\,(2n+1)}\right]\frac{a_m}{R^{m+2}}\lambda^{n+m+2}=0 \quad (10b)$$

modified Bessel functions of zeroth, first and second order. The reader is referred to the original report for detailed analysis and description of the solution technique. The constants $a_n$ and $b_n$ constitute the solution vector and can be solved to a higher degree of accuracy by increasing the number of solved equations *"n"*. Since two equations are solved simultaneously, n takes an even number (typically multiples of 2).

The parameter $\alpha$ in Eq. (7a) can be defined as follows:

$$\alpha=\begin{cases}-U & n=2\\ 0 & n>2\end{cases} \quad (11)$$

In fact, only $b_0$ is of interest in solving the wall correction factor. It can be shown that [17]:

$$Kv=\frac{-2}{3}\frac{b_0}{UR} \quad (12)$$

Similar to many exact solutions the analysis yielded some infinite series and the selection of number of terms (truncation) would affect the accuracy of the solution. The process of determination of $\boldsymbol{b_o}$ is described by Haberman and Sayre as:

*"Wall correction factors for rigid spheres moving in a still liquid inside an infinitely long cylinder have been determined by numerically solving the algebraic system (Equation [10]) for the coefficient* $\boldsymbol{b_o}$ *over a large range of diameter ratios. The number of equations of the algebraic system used was increased (at most up to eight) until only very small changes in the value of* $\boldsymbol{b_o}$ *were obtained".*

A computer program was developed to numerically compute the integrals $S_2$, $S_4$ and $S_3$ and construct the system of linear equations. The linear system is then solved using the buit-in Octave function (Octave 4.4.1 version is used) which produced the solution. The computed values of $b_0$ are then used to calculate the wall correction factor as defined by Eq. (9). Table (1) lists a comparison of the reported values of the exact and approximate solution along with the values of the obtained results at different system sizes. The 2x2 system in the above equation should recover the approximate solution which –physically- represents a situation where a slip boundary condition is imposed at the cylinder. The length of the system used to obtain the exact solution is 8x8 as per Haberman and Sayre reported.

*"The number of equations of the algebraic system used was increased (at most up to eight) until only very small changes in the value of* $b_o$ *were Obtained."*

A comparison of the results of the different systems is provided in Table (1) below

The second columns in Table (1) is borrowed from Haberman and Sayre report while the third column is generated using Eq. (1). Typically, there should be no difference between the third, fourth columns as well as the second and sixth columns and the existing differences are because of numerical differences in evaluating the integrals of S (although not shown these differences are not significant- ranging between 0.01% -0.5%) and because of how truncation error grow when solving the linear system. The built-in linear system solver is designed to find the efficient

method of solving a linear system and perform necessary operations such as scaling. In fact a 16x16 system had poor results at λ value > 0.5, this is because the values of S grows dramatically as *n* increases affecting the condition number of the matrix to values that could not be fixed by the linear solver. The solver is capable of getting a solution at lower λ values is because the integrals S is multiplied by powers of λ than alleviate this issue at small λ values. The difference between the solution of the 8x8 system is comparable to the exact solution with a maximum discrepancy of 1.5% at λ=0.8.

**Table (1).** Comparison of the numerical solution at different system sizes with HS solution

| λ | Exact HS | App. (Eq. 1) | 2x2 | 4x4 | 8x8 | %diff with Exact |
|---|---|---|---|---|---|---|
| 0 | 1.000 | 1 | 1 | 1 | 1 | 0 |
| 0.1 | 1.236 | 1.2633 | 1.2632 | 1.2632 | 1.2632 | 0.02 |
| 0.2 | 1.680 | 1.6797 | 1.6794 | 1.6795 | 1.6795 | -0.03 |
| 0.3 | 2.371 | 2.3697 | 2.3687 | 2.3700 | 2.3701 | -0.04 |
| 0.4 | 3.596 | 3.5816 | 3.579 | 3.5913 | 3.5914 | 0.63 |
| 0.5 | 5.970 | 5.8700 | 5.8596 | 5.9467 | 5.9474 | -0.38 |
| 0.6 | 11.135 | 10.593 | 10.55 | 11.082 | 11.092 | -0.39 |
| 0.7 | 24.955 | 21.425 | 21.215 | 24.519 | 24.676 | -1.12 |
| 0.8 | 73.555 | 49.023 | 47.711 | 71.387 | 74.648 | 1.49 |
| 0.9 | NA | 121.27 | 111.83 | 323.74 | 460.95 | NA |

41 data points were fed to the software ranging between 0-0.8 with a uniform increment of 0.02. Complicated formulas are excluded since we are seeking a simple expression. By assuming *Kv=f(λ,(1–λ)* ) and using test/train ratio of 50-50, the following function is selected:

$$K_v = (1-\lambda)^{-2.68945} - (\lambda + 0.4967)\lambda \quad (13a)$$

Which can be further simplified as:

$$K_v = (1-\lambda)^{-2.69} - (\lambda + 0.5)\lambda \quad (13b)$$

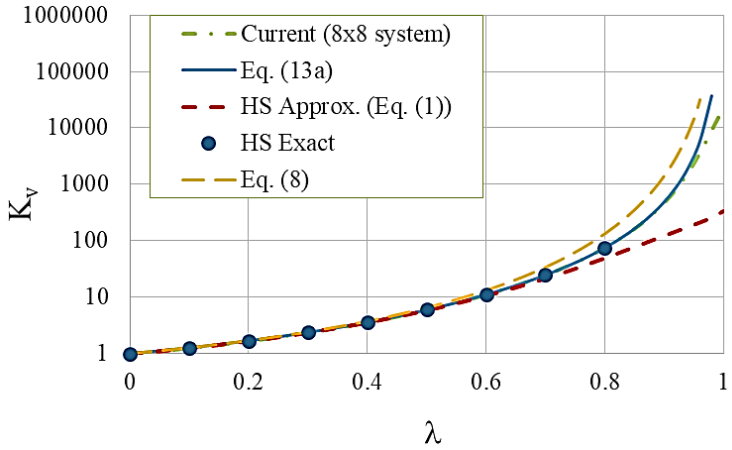


**Figure (5).** Comparison with Eq. (13a) along with HS exact and approximate analysis

Differences between Eqs. 13a and 13b are graphically indistinguishable. The agreement with the report exact solution from Haberman and Sayre's report along with the agreement with the 8x8 system result is listed in the Table (2).

Although a difference of ~ 6% can be seen at λ=0.9, we suggest that the behavior of the formula is acceptable and could be more realistic than the theoretical analysis which –to some extent- has numerical fingerprints. The formula has a singularity at λ =1 which is physically indicates that the sphere would cease its motion for infinitely long time if the sphere diameter is the same as the cylinder diameter. Such phenomena can be noticed in the falling ball viscometer for viscous liquids when λ approaches one. Indeed, the current expression agrees better with the exact solution reported by Haberman and Sayre than the limiting behavior of the generic function produced earlier (Eq. (8)).

**Table (2).** Comparison of current expressions with data fed to the software and HS exact solution

| λ | Exact HS | 8×8 | Eqn. 13a | Diff % | | Eqn. 13b | Diff % | |
|---|---|---|---|---|---|---|---|---|
| | | | | HS | 8×8 | | HS | 8×8 |
| 0 | 1 | 1 | 1 | 0 | 0 | 1 | 0 | 0 |
| 0.1 | 1.263 | 1.2632 | 1.2679 | 0.4 | 0.4 | 1.2677 | 0.4 | 0.4 |
| 0.2 | 1.68 | 1.6795 | 1.6830 | 0.2 | 0.2 | 1.6826 | 0.2 | 0.2 |
| 0.3 | 2.371 | 2.3701 | 2.3708 | -0.0 | 0.0 | 2.3703 | -0.0 | 0.0 |
| 0.4 | 3.596 | 3.5914 | 3.5918 | 0.6 | 0.0 | 3.5916 | 0.6 | 0.0 |
| 0.5 | 5.97 | 5.9474 | 5.9523 | -0.3 | 0.1 | 5.9531 | -0.3 | 0.1 |
| 0.6 | 11.135 | 11.092 | 11.098 | -0.3 | 0.1 | 11.101 | -0.3 | 0.1 |
| 0.7 | 24.955 | 24.676 | 24.646 | -1.2 | -0.1 | 24.660 | -1.2 | -0.1 |
| 0.8 | 73.555 | 74.648 | 74.794 | 1.7 | 0.2 | 74.858 | 1.8 | 0.3 |
| 0.9 | -- | 460.95 | 487.91 | -- | 5.9 | 488.52 | -- | 6.0 |
| 1 | -- | 22098 | NA | -- | NA | NA | -- | NA |

## CONCLUSIONS

A machine-learning-based symbolic regression was used to generate a generic wall correction formula. The formula, based on data reported by Fidleris and Whitmore, captures the general trend of the data and has good agreement with intermediate and limiting behavior in both creeping flow and fully turbulent regimes.

The generated formula (Eq. (7a)) was found applicable for λ values between 0.02 and 0.9 and Reynolds numbers up to 20000 whereas a slightly modified version (Eq. (7b)) is assumed applicable for almost the complete range of λ ($0 \leq \lambda \leq 1$) for the same Reynolds number. The exact solution of Haberman and Sayre was used to create a simple formula for the creeping flow regime, which was compared with the exact solution and found to be accurate up to λ =0.8. However, more data is needed at very high Reynolds numbers to confirm that the effect of Re diminishes as it approaches zero. Future work could include using more data from FW or running benchmark numerical simulations to improve the accuracy of the regression formula.

**Duality of interest:** The authors declare that they have no duality of interest associated with this manuscript.

**Author contributions:** Contribution is equal between authors.

**Funding:** No specific funding was received for this work.

## REFERENCES

Arsenijević, Z. L., Grbavčić, Ž., Garić-Grulović, R., & Bošković-Vragolović, N. (2010). Wall effects on the velocities of a single sphere settling in a stagnant and counter-current fluid and rising in a co-current fluid. *Powder Technology, 203*(2), 237-242.

Barati, R., Neyshabouri, S. A. A. S., & Ahmadi, G. (2014). Development of empirical models with high accuracy for estimation of drag coefficient of flow around a smooth sphere: An evolutionary approach. *Powder Technology, 257*, 11-19.

Barr, G. (1931). A Monograph of Viscometry. London: Oxford Univ. *Press, Humphrey Milford*.

Bohlin, T. (1960). On the drag on a rigid sphere moving in a viscous liquid in a cylindrical tube. *Trans. R. Inst. Tech.(Stockholm) No, 155*, 3-63.

Bougas, A., & Stamatoudis, M. (1993). Wall factor for acceleration and terminal velocity of falling spheres at high reynolds numbers. *Chemical Engineering & Technology: Industrial Chemistry‐Plant Equipment‐Process Engineering‐Biotechnology, 16*(5), 314-317.

Bowen, W. R., & Sharif, A. O. (1994). Transport through microfiltration membranes—particle hydrodynamics and flux reduction. *Journal of colloid and interface science, 168*(2), 414-421.

Brown, P. P., & Lawler, D. F. (2003). Sphere drag and settling velocity revisited. *Journal of environmental engineering, 129*(3), 222-231.

Chandrasekhar, S. (2003). *Newton's Principia for the common reader*: Oxford University Press.

Chhabra, R., Agarwal, S., & Chaudhary, K. (2003). A note on wall effect on the terminal falling velocity of a sphere in quiescent Newtonian media in cylindrical tubes. *Powder Technology, 129*(1-3), 53-58.

Chhabra, R. P. (2006). *Bubbles, drops, and particles in non-Newtonian fluids*: CRC press.

Clift, R., Grace, J., Weber, M., & Bubbles, D. (1978). Particles: Academic Press, New York.

Di Felice, R. (1996). A relationship for the wall effect on the settling velocity of a sphere at any flow regime. *International Journal of Multiphase Flow, 22*(3), 527-533.

Di Felice, R., Gibilaro, L., & Foscolo, P. (1995). On the hindered settling velocity of spheres in the inertial flow regime. *Chemical Engineering Science, 50*(18), 3005-3006.

El Hasadi, Y. M., & Padding, J. T. (2019). Solving fluid flow problems using semi-supervised symbolic regression on sparse data. *AIP Advances, 9*(11), 115218.

El Hasadi, Y. M., & Padding, J. T. (2023). Do logarithmic terms exist in the drag coefficient of a single sphere at high Reynolds numbers? *Chemical Engineering Science, 265*, 118195.

Fidleris, V., & Whitmore, R. (1959). Measurement of the falling velocity of particles in opaque fluids. *Journal of Scientific Instruments, 36*(1), 35.

Fidleris, V., & Whitmore, R. (1961). Experimental determination of the wall effect for spheres falling axially in cylindrical vessels. *British journal of applied physics, 12*(9), 490.

Haberman, W., & Sayre, R. (1958). David Taylor Model Basin Report No. 1143, Washington, D. *C, US Navy Dept*.

Happel, J., Brenner, H., & Low Reynolds Number Hydrodynamics, M. N. (1983). Publishers. *The Hague*.

Higdon, J., & Muldowney, G. (1995). Resistance functions for spherical particles, droplets and bubbles in cylindrical tubes. *Journal of Fluid Mechanics, 298*, 193-210.

IWAOKA, M., & ISHII, T. (1979). Experimental wall correction factors of single solid spheres in circular cylinders. *Journal of Chemical Engineering of Japan, 12*(3), 239-242.

Jones, A. M. (1957). Drag coefficients for flat plates, spheres, and cylinders moving at low Reynolds numbers in a viscous fluid.

Kehlenbeck, R., & Felice, R. D. (1999). Empirical relationships for the terminal settling velocity of spheres in cylindrical columns. *Chemical Engineering & Technology: Industrial Chemistry‐Plant Equipment‐Process Engineering‐Biotechnology, 22*(4), 303-308.

Ladenburg, R. (1907). Über den Einfluß von Wänden auf die Bewegung einer Kugel in einer reibenden Flüssigkeit. *Annalen der Physik, 328*(8), 447-458.

Li, M., Zhang, G., Xue, J., Li, Y., & Tang, S. (2014). Prediction of the wall factor of arbitrary particle settling through various fluid media in a cylindrical tube using artificial intelligence. *The Scientific World Journal, 2014*.

Munroe, H. S. (1889). *The English Versus the Continental System of Jigging: Is Close Sizing Advantageous?*

Oseen, C. W. (1910). Uber die Stokes' sche Formel und Uber eine verwandte Aufgabe in der Hydrodynamik. *Arkiv Mat., Astron. och Fysik, 6*, 1.

Satapathi, R. (1960). A study of the motion of solid spheres and liquid drops in liquids.

Singh, A. V., Sharma, L., & Gupta-Bhaya, P. (2012). Studies on falling ball viscometry. *arXiv preprint arXiv:1202.1400*.

Stokes, G. G. (1851). On the effect of the internal friction of fluids on the motion of pendulums.

Tullock, D., Phan Thien, N., & Graham, A. (1992). Boundary element simulations of spheres settling in circular, square and triangular conduits. *Rheologica acta, 31*(2), 139-150.

Uhlherr, P., & Chhabra, R. (1995). Wall effect for the fall of spheres in cylindrical tubes at high Reynolds number. *The Canadian Journal of Chemical Engineering, 73*(6), 918-923.

Wham, R., Basaran, O., & Byers, C. (1996). Wall effects on flow past solid spheres at finite Reynolds number. *Industrial & Engineering Chemistry Research, 35*(3), 864-874.

Al-Mukhtar Journal of Engineering Research 08 (1): 27-35, 2024
Doi: https://doi.org/10.54172/14qx1748

Research Article

Open Access

# Simulation of Dehydration Process by Using Ethylene Glycol Butyl Ether (Egbe)

**Abdualfatah S. Mahmod[1*], Abdrabba I. Hassan[2] and Rasha A. Alabd[3]**

***Corresponding author:** abdulfatah.suiliaman@omu.edu.ly , Department of Chemical Engineering, Faculty of Engineering, Omar Al-Mukhtar University.

[2, 3] Department of Chemical Engineering, Faculty of Engineering, Omar Al-Mukhtar University.

**Received:**
31 December 2023

**Accepted:**
28 January 2024

**Publish online:**
31 December 2024

## Abstract

The raw natural gas extracted from production wells contains many impurities such as oil, sulphur, carbon dioxide, nitrogen, and other impurities. Among these impurities that must be removed in order to achieve the specifications of the liquid natural gas (LNG) is a water vapor. Because free water causes hydrate formation in transport pipelines and in addition to corrosion when combine with acid gases, resulting in heavy losses in maintenance costs of transport pipelines. For these reasons, natural gas must be dehydrated. The most common methods is Glycol dehydration process, and this process has a good results. In this paper, we have suggested a solvent and simulated it and proof its effectiveness in dissolving the water and dehydration the gas instead of using Tri-ethylene Glycol (TEG). This solvent is Ethylene Glycol Butyl Ether (EGBE), It is used widely as a solvent in surface coatings, and used in metal and household cleaners. It isn't use in previously natural gas processing. The comparison between glycol types done by Aspen Hysys (glycol package model approach) and according to the dry gas specifications, the simulation results show that: the appropriate flow rate for EG, DEG, TEG, TREG and EGBE are 500 Kgmol/h, 429.5 Kgmol/h, 337.1 Kgmol/h, 80 Kgmol/h and 25.3 Kgmol/h, respectively. Ethylene Glycol Butyl Ether prove a high the efficiency it in dissolving the water with a little flow rate, as well as decrease the energy required for the operation. This paper looks to the use of EGBE as an alternative to TEG for its high efficacy in dissolving water, also significant decrease in the cost of dehydration gas about 98.7 x $10^9$ $/Year**]**.

**Keywords:** Glycol, Dehydration, Natural Gas, Software, Butyl Glycol, EGBE.

## INTRODUCTION

It is believed that natural gas was initially used for commercial purposes by the Chinese approximately 2,400 years ago. Shallow wells provided the gas, which was carried in bamboo pipes and utilized in gas-fired evaporators to create salt from brine. In the late 17th and early 18th centuries, the gas was also used in the United States for home lighting and streetlights. The second known usage of natural gas for commercial purposes was in 1821. In Fredonia, New York, William Hart dug a shallow 30-foot (9-meter) well, and he used wooden pipes to deliver the gas to nearby homes.

A few small-scale, local programs involving natural gas were implemented in the ensuing years, but large-scale activity didn't start until the early 1900s. The United States was the world's top consumer of natural gas (22.9 TCF) and the second-largest production (19.2 TCF) in 2004.

Natural gas is mostly used as fuel, but it is also a significant supply of elemental sulfur, a crucial industrial ingredient, and hydrocarbons for petrochemical manufacturing. One of the safest, most convenient, and cleanest sources of energy for daily use is natural gas (NG). As indicated in Table 1, its primary constituent is methane (CH4), although it also contains ethane, propane, butane, and other chemicals. You can find natural gas on its own or in combination with oil. When the gas is extracted from the earth, it may be contaminated with water, oil, sulphur, carbon dioxide, nitrogen, and other substances. The water vapor in the gas created issues since it caused the water to condense on cold surfaces such as pipeline walls or storage tanks if the temperature drops below the water vapor's dew point temperature (Tdew) (Arthur et al 2006).

Condensed water in the pipeline creates slug flow and erosion, water vapor increases the volume and lowers the heating value of the gas, and the dissolved water in NG is corrosive, particularly when it contains CO2 and/or H2S (Francis et al 1991). Finally, NG in combination with liquid water can form methane hydrate. Gas hydrates are formed at high pressures and low temperatures when water lattice with cavities trap gas molecules such as methane (Kelly et al 2019). By employing a physical absorption technique in which the gas is in contact with a liquid that selectively absorbs the water vapor, the amount of water in NG can be lowered to the 10 ppmv level.

**Table:(1).** The main constituents of natural gas

| Class | Compnent | Formuls |
|---|---|---|
| Hydrocarbon | Methane | $CH_4$ |
| | Ethane | $C_2H_6$ |
| | Propane | $C_3H_8$ |
| | i-Butane | i-$C_4H_{10}$ |
| | n-Butane | n-$C_4H_{10}$ |
| | i-Pentane | i-$C_5H_{12}$ |
| | n-Pentane | n-$C_5H_{12}$ |
| | Cyclopentane | $C_5H_{10}$ |
| | Hexane and ggheavier | $C_{6+}$ |
| Inert Gases | Nitrogen | $N_2$ |
| | Helium | He |
| | Argon | Ar |
| | Hydrogen | $H_2$ |
| | Oxygen | $O_2$ |
| Aicd Gases | Hydrogen-Solifide | $H_2S$ |
| | Carbon Dioxide | $CO_2$ |
| Sulfur | Mercaptans | R-SH |
| Compounds | Sulfides | R-S- R' |
| | Disulfides | R-S-S-R' |
| Water Vapor | | $H_2O$ |
| Liquid sluges | Free water or Brine | |
| | Corrosion inhibitores | $CH_3OH$ |
| | Methanol | |
| Solids | Millescale and rust | |
| | Iron sulfide | FeS |
| | Reservior fines | |

The most widely used absorbents are ethylene glycol (EG), diethylene glycol (DEG), tri-ethylene glycol (TEG), tetra-ethylene glycol (TREG), and propylene glycol; tri-ethylene glycol is the glycol of choice in most cases. The process of removing water is called the glycol dehydration process. (Arthur et al 2006).

This paper presents a novel approach in which we demonstrate the efficacy of butyl glycol as a solvent for absorbing water vapor. Additionally, we will compare ethylene glycol (EG), diethylene glycol (DEG), tri-ethylene glycol (TEG), tetra-ethylene glycol (TREG), and ethylene glycol butyl ether (EGBE).

## DESCRIPTION OF TRADITIONAL PROCESS

**In** order to exclude any liquid hydrocarbons from the gas stream, wet natural gas normally first passes through an input separator, as illustrated in figure 1. The gas then travels to a contractor, or absorber, where the lean glycol comes into contact with it and dries it. The dry gas exiting the absorber passes through a gas/glycol heat exchanger and then into the sales line.

**Rich** glycol exiting the absorber flows through a valve to decrease the pressure, and then rich glycol is flashed to remove dissolved hydrocarbons and can be used for fuel and/or stripping gas. Heat exchange between the cool rich glycol and the hot lean glycol is improved by using two or more shell and tube heat exchangers in series.

**The** stripper's top is where the desorbed natural gas and water vapor are released. After exiting the reboiler, the hot, regenerated lean glycol is cooled by cross-exchange with returning rich glycol. It is then pushed to a glycol/gas heat exchanger and returns to the absorber's top. Must add a TEG solution makeup before feeding it to the contactor column. (Fabrizio et al 2016/2017).

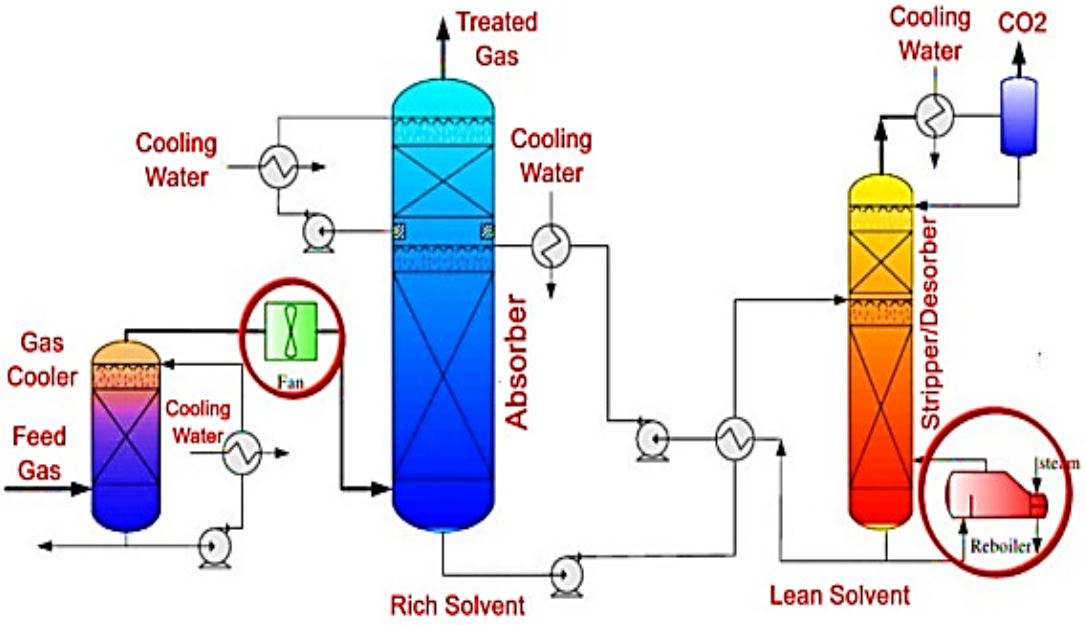


**Figure: (1).** Typical glycol dehydration unit

In simulation of the process, there are two different streams exist in the Plant. The inlet streams for the process were: Wet Gas and the other is lean glycol. The basis for the simulation was 50 MMSCFD of wet gas, where the data of NG from Arabian Gulf Oil Company (AGOCO). The specification of these streams is existent in Table 2 and as shown in figure 2 after the simulation.

**Table :( 2).** Characteristics of streams' physical attributes

| Name | Wet Gas ( Feed 1) | Lean Glycol ( Feed 2) |
|---|---|---|
| Temperature | 35 | 41 |
| Pressure | 24.82 | 24.82 |
| Mole Flow | 50 MMSCFD | 208 Kmol/h |
| | Composition | |
| $CH_4$ | 0.715700 | 0 |
| $C_2H_6$ | 0.102160 | 0 |
| $C_3H_8$ | 0.069694 | 0 |
| n-$C_4H_{10}$ | 0.029119 | 0 |
| i-$C_4H_{10}$ | 0.014414 | 0 |
| n-$C_5H_{12}$ | 0.008293 | 0 |
| i-$C_5H_{12}$ | 0.006934 | 0 |
| n-$C_6H_{14}$ | 0.005462 | 0 |
| n-$C_7H_{16}$ | 0.002684 | 0 |
| n-$C_8H_{18}$ | 0.000556 | 0 |
| n-$C_9H_{20}$ | 0.000015 | 0 |
| $H_2O$ | 0.002500 | 0.005 |
| $CO_2$ | 0.016907 | 0 |
| $H_2S$ | 0.001300 | 0 |
| $N_2$ | 0.028060 | 0 |
| Glycol (TEG) | 0 | 0.995 |

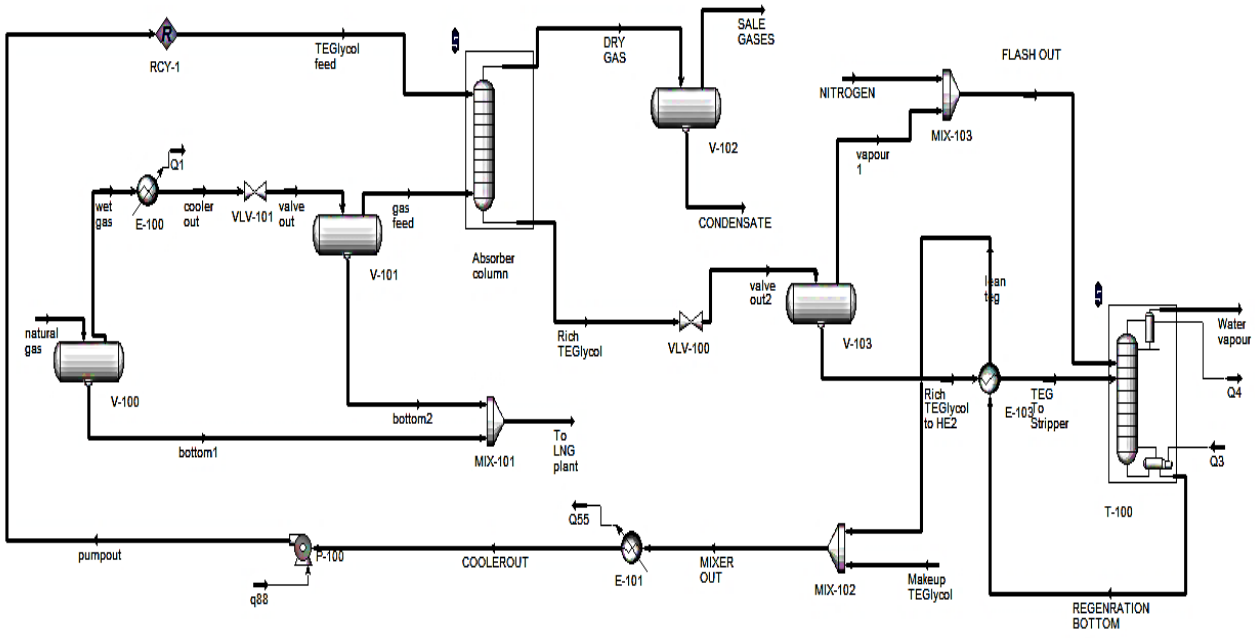


**Figure: (2).** Simulation of dehydration unit

## COMARISON OF ABSORPTION PROCESSES BY DIFFERENT TYPES OF GLYCOL

Some types of glycol ethers have been widely utilized for about half a century, having first been developed in the 1930s. Typically, they dissolve in both water and oil, and they include a diverse family of over thirty solvents. Due to their miscibility in a wide range of organic solvents including water.

**Absorption Process by Mono-ethylene Glycol (MEG):**
The most basic glycol is ethylene glycol, which is the adduct of ethylene oxide (EO) and water. Because MEG has a high viscosity at low temperatures, it is employed more as an inhibitor (to stop the formation of hydrates) than as a solvent.

**Absorption Process by Diethylene Glycol (DEG):**
Although diethylene glycol is low efficiency to absorb the water only to is uses for gas dehydration in colder climates (e.g., the North Sea) because of its lower viscosity (Arthur et al 2006).

**Absorption Process by Tri-ethylene Glycol:**
Tri-ethylene glycol (TEG) is the most common absorbent for gas dehydration, and it is traditional process for dehydration of the gas. It is easy to regenerate it and we can get about 98-99 percent purity of the TEG after regeneration.

**Tetra-ethylene Glycol (TREG):**
Tetra-ethylene glycol is the high efficiency absorbent for dehydration, but due to more expensive than TEG, therefore it is not a lot used for this purpose.

**Absorption Process by Butyl Glycol:**
Trade names for Butyl Cellosolve, O-Butyl Ethylene Glycol, Butyl Glysolv, Butyl Oxital EB, and Glycol Ether EB are examples of Ethylene Glycol Butyl Ether (EGBE).

EGBE is colorless organic liquid with a mild, non-residual odor, a sweetish odor, or a mild ether odor (Michael 1993). Solubility of EGBE in water can be considered as highly miscible in water up to about 100 g/l. It is extensively utilized as a solvent in surface coatings, including quick-dry and spray lacquers, enamels, varnishes, varnish removers, and latex paint. It is also used in metal and household cleaners (Ms J.Wess et al 1998).

Most glycol ethers have minimal acute toxicity (Brussels 2005). During 2003, the production of EGBE in the European Union was approximately 161,000 tonnes. Ethylene oxide and n-butyl alcohol are added to create EGBE. The properties of TEG, BG and the water are present in Table 3.
As shown in Figure 3, the butyl glycol has lowest boiling point, that's mean the energy needed for the dehydration process of NG will be low.

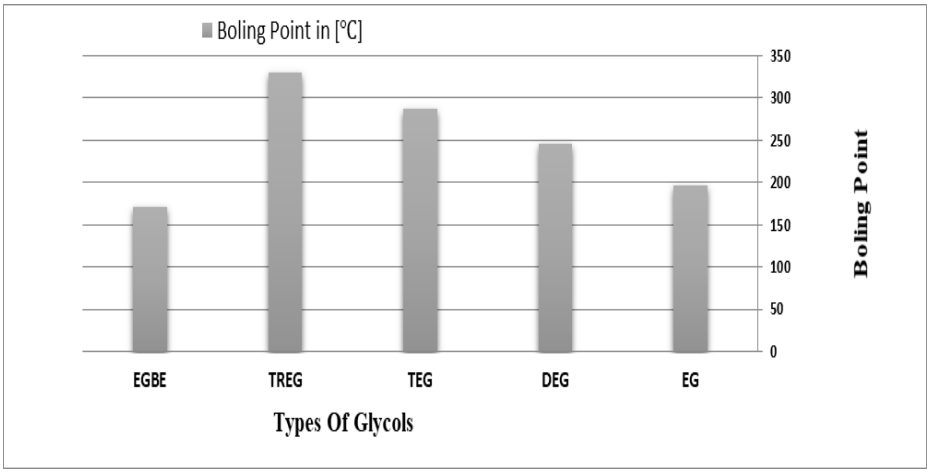


**Figure: (3).** Boiling of Glycols

**Table :(3).** Properties of TEG, BG and the water

| Properties | MEG | DEG | TEG | TREG | Butyl Glycol | Water |
|---|---|---|---|---|---|---|
| Formula | $C_2H_6O_2$ | $C_4H_{10}O_3$ | $C_6H_{14}O_4$ | $C_8H_{18}O_5$ | $C_4H_9OCH_2CH_2OH$ | $H_2O$ |
| Molar Mass [Kg/Kmol] | 62.07 | 106.12 | 150.17 | 194.23 | 118.2 | 18.015 |
| Normal Boiling Point [℃] | 197.1 | 245.3 | 288.0 | 329.7 | 171 | 100.0 |
| Vapor Pressure@ 20 ℃ $[Pa]$ | 8.3 | 0.34 | 0.05 | 0.007 | 0.117 | 3170 |
| Density @ 20 ℃ $[kg\ /\ m^3$ | 1113 | 1120 | 1126 | 1126 | 902 | 55.56 |
| Viscosity @ 20 ℃ $[mPa.s\ ]$ | 16 | 38 | 48 | 52 | 3.3 | 0.894 |
| Maximum recommended regeneration temperature [°C] | 163 | 177 | 204 | 224 | 140 | - |

The butyl glycol star brightened in 2010 as it contributes for solved the Gulf of Mexico disaster, as a result of the leakage of approximately 4.9 million barrels in its water at a depth of 1500 m below sea level.

## MATERIALS AND METHODS

In this paper we will use a substitute for Tri-ethylene glycol for dehydration of natural gas. The study done on jest absorber column as shown in figure 4, with same specification that existent in Table 2.

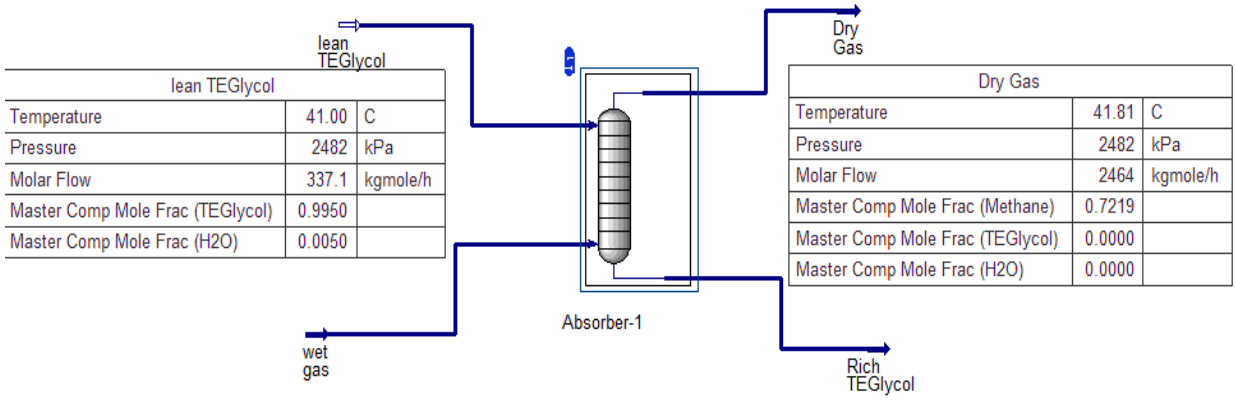


**Figure: (4).** Absorber column

## DISCUSSION AND RESULT

From figure 5, it can be deduced the appropriate flow rate for each type of glycols, also we note that, when we use the butyl glycol (EGBE) as a replacement for tri-ethylene glycol (TEG), it has much lower flow rate about [4 – 7 lb/MMSCF]) with retaining the natural gas specifications as a dry gas.

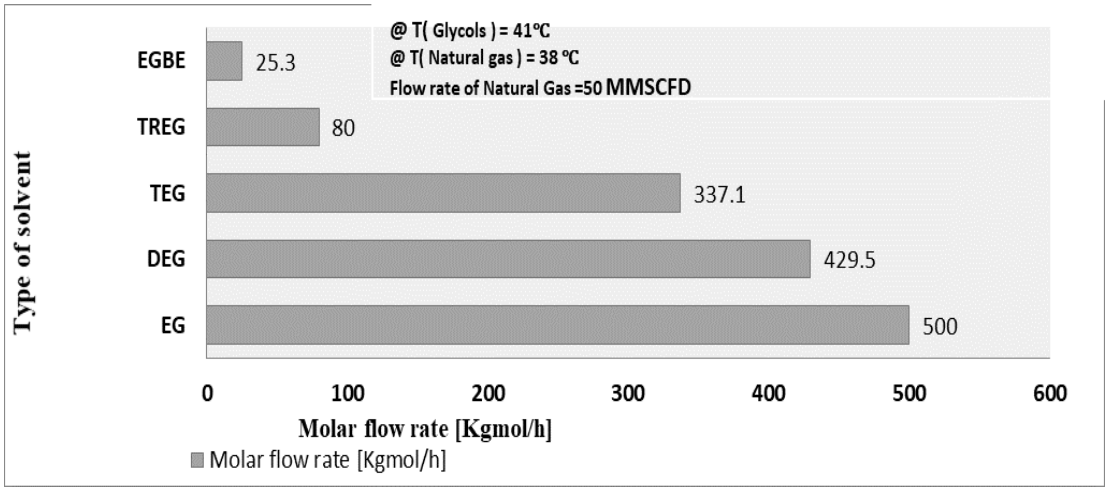


**Figure: (5).** The Quantity suitable for all Glycol types

Through figure 6, evidently, the effect of the EGBE in dissolving the water and dehydrate the natural gas.

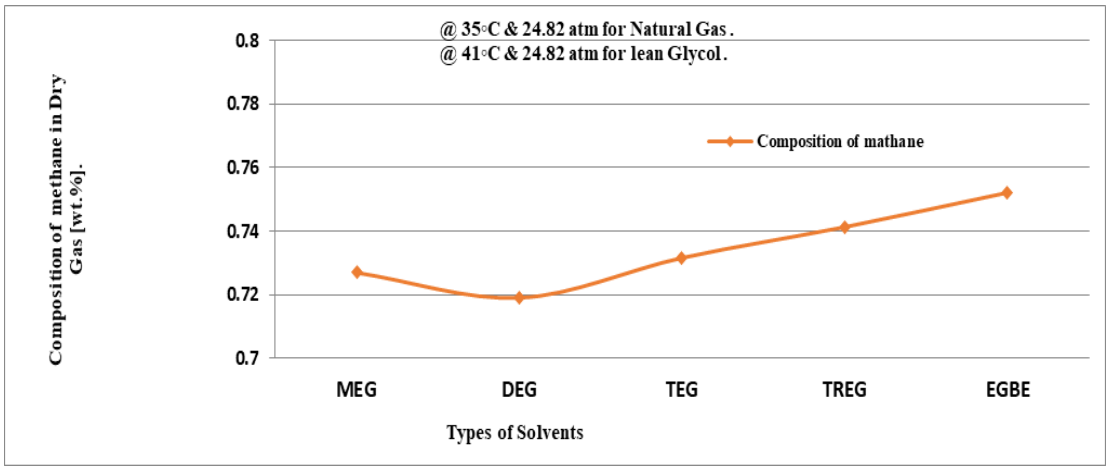


**Figure: (6).** Composition of Methane in Dry Gas. Vs Types of Solvents

## SOLVENTS COST

Additionally, based on each solvent's flow rate during the process, as shown in Table 4 cost of the solvents at current prices (2021) was compared.

**Table :(4).** Price of Glycol and the cost of glycols

| Type of Solvent: | The price in [$/ 1 Kg] | The Cost | |
|---|---|---|---|
| | | In [$ /h] | In [$/Year] |
| MEG | 0.86[9] | 0.86 * 3.092 x $10^4$ =26608.4 | 233 x $10^6$ |
| DEG | 40.5[10] | 40.5 * 6.421 x $10^4$ =26 x $10^5$ | 228 x $10^8$ |
| TEG | 200[11] | 200*5.638 x$10^4$ = 11.2 x $10^5$ | 988 x $10^8$ |
| TREG | 142[12] | 142*1.547x$10^4$ = 22 x $10^6$ | 192x $10^9$ |
| EGBE | 4[13] | 4 * 2977 = 11908 | 104 x $10^6$ |

Figure 7 compares the costs of the solvents and shows that the EGBE is more economically viable.

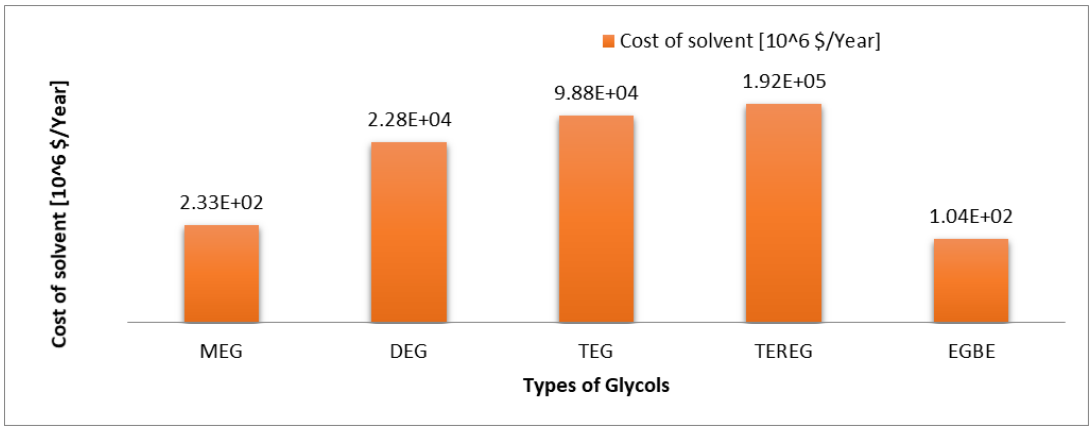


**Figure: (7).** Comparison between the Costs of Solvents

## CONCULSION

The dehydration process is important part in treatment of the natural gas, because the water dissolved in the NG made many of problems such as dehydrate formation, corrosion specially when combine with $CO_2$ and/or $H_2S$. In view of this, it concludes with the following:

- TEG has a good efficiency for dehydration the gas.
- TREG has a high efficiency, but also needs to high cost for this reason, therefore it is not a lot used for this purpose.
- Since the molecule contains both functional groups, glycol mono-ethers (EGBE) are a liquid that combine the solubility properties of ethers and alcohols. They are therefore widely used in solvent application, including formulations such a paints, inks and cleaning fluids.
- EGBE prove a high the efficiency it in dissolving the water, and in the same time reduce the cost of dehydration of natural gas.

**Duality of interest:** The authors declare that they have no duality of interest associated with this manuscript.

**Author contributions:** Contribution is equal between authors.

**Funding:** No specific funding was received for this work.

## REFERENCES

Dieter, M. (1993). NTP technical report on the toxicity studies of Ethylene Glycol Ethers: 2-Methoxyethanol, 2-Ethoxyethanol, 2-Butoxyethanol (CAS Nos. 109-86-4, 110-80-5, 111-76-2) Administered in Drinking Water to F344/N Rats and B6C3F1 Mice. *Toxicity report series, 26*, 1-G15.

Gribble, M. (2005). *The toxicology of glycol ethers and its relevance to man*. ECETOC.

Huot, K., White, M., & Acharya, T. (2019). Natural Gas Hydrates: A Review of Formation, and Prevention/Mitigation in Subsea Pipelines. *Advanced Science, Engineering and Medicine, 11*(6), 453-464.

Kidnay, A. J., & Parrish, W. R. (2006). Fundamentals of Natural Gas Processing.

Manning, F. S., & Thompson, R. E. (1991). Oilfield processing of petroleum.

Panizzolo Terrin, F. (2017/2017). Modelling of natural gas sweetening and dehydration processes. *UniversitÀ Degli Studi Di Padova Anno Accademico*.

Wess, J., Ahlers, H., Dobson, S., & Organization, W. H. (1998). *2-Butoxyethanol*. World health organization.

Document/Report from Website:
http://ec.europa.eu/health/ph_risk/risk_en.htm.
https://m.chemicalbook.com/price/Ethylene-glycol-1_3.htm.
https://m.chemicalbook.com/price/Diethylene-.htm.
https://m.alibaba.com/amp/showroom/Triethylene+glycol++TEG+.html.
https://m.chemicalbook.com/price/Tetraethylene-glycol-dimethyl- ether_3.htm

Al-Mukhtar Journal of Engineering Research 08 (1): 36-50, 2024
Doi: https://doi.org/10.54172/nkr1d641

Research Article

Open Access

# Top Glass Cover Effect On The Performance of a Parabolic Trough Solar Receiver

**Mohamed A. Eltarkawe[1]*, Ali A.A. Adam[2] and Hasan A. H. Husayn[3]**

***Corresponding author:** mohamed.eltarkawe@omu.ly.edu, Department of Mechanical Engineering, Faculty of Engineering, Omar Al-Mukhtar University, Libya.

[2] Department of Mechanical Engineering, Faculty of Engineering, Omar Al-Mukhtar University, Libya.

[3] Department of Renewable Energy Engineering, Faculty of Engineering, Omar Al-Mukhtar University, Libya

**Received:**
21 January 2024

**Accepted:**
19 November 2024

**Publish online:**
31 December 2024

**Abstract**

Solar energy is a promising solution to the rapidly increasing energy consumption. The parabolic trough collector (PTC) can be a practical solution, particularly in providing domestic water heating in developing countries. The impact of the glass envelope on PTC performance has been investigated extensively. However, only a few studies have investigated the effects of a flat-top glass cover. This study examines the impact of a top glass cover on the PTC performance by manufacturing two identical PTCs, one with a top glass cover and the other without a top cover. The top-covered collector showed a higher maximum absorber surface temperature (11%) and higher maximum water temperature (4%) than the temperatures of uncovered PTC. The results also showed that the theoretical efficiency was %56.9 and the experimental efficiency was %50.4. Installing the glass cover has led to a gain in theoretical thermal efficiency by 5% and in experimental thermal efficiency by 4%. The study recommends that future studies improve the reflecting mirrors and increase the size of the prototype.

**Keywords:** Parabolic Solar Collector; Solar Energy; Thermal Efficiency; Top-Glass Cover; Energy Balance.

## INTRODUCTION

Due to the fast increase in population worldwide, energy consumption has significantly increased, leading to high emissions levels. In addition, these conventional sources of energy will become extinct soon (Islam et al., 2018). Finding and developing alternative sources of energy have become inevitable (Ibrahim, 2020; de Oliveira Siqueira et al., 2014). Among the different renewable energy sources, solar energy is a promising solution to many challenges (Tian & Zhao, 2013; Brooks, 2005). Thermal solar collectors provide practical solutions to many applications ranging from electricity production to hot water supply for domestic usage (Maree & Ismaeel, 2019).

Depending on the concentration ratios, solar collectors are often divided into two categories: non-concentrating collectors and concentrating collectors. In a non-concentrating collector, the intercepting area equals the collector's absorbing area, while a concentrating solar collector often has concave reflecting surfaces larger than the intercepting area. The concentrating collec-

tors can be classified into two groups: point concentrating and line concentrating (Tian & Zhao, 2013; Fernández-García et al., 2010; Hachicha, 2013). Point-concentrating technologies focus solar radiation on a single point. The most common applications of this method are the dish/engine systems and central receiver systems (Hachicha, 2013). On the other hand, line concentration systems collect the incoming energy from the sun using long rectangular or curved mirrors. These mirrors reflect and concentrate the sunlight on tubes (or absorbers). A fluid flowing inside the tubes will then be heated and transferred to a storage or steam turbine generator to produce electricity. An example of a concentrating collector is the Parabolic trough collector (PTCs), which consists of a trough mirror that concentrates the incoming solar energy onto an absorber tube, which transports the energy to the working fluid passing inside it (Tian & Zhao, 2013; Fernández-García et al., 2010; Abed & Afgan, 2020; Ahmed et al., 2016).

The PTC systems have proven to be a feasible and promising technology for the future of renewable energy in many places around the world, including developing countries. The positive impact of a glass annulus envelope on the PTC performance is well-known and extensively investigated. However, glass annulus envelope technology increases the cost of the solar collector significantly. For the PTC technology to succeed particularly in developing countries, the cost must be reduced even with slightly compromising efficiency. Using a flat-top glass cover instead of a glass annulus envelope (Bhujangrao, 2015) will significantly reduce the manufacturing cost. Low-cost PTCs can be a practical solution to the energy challenge in Libya, which has been suffering from power outages and rolling blackouts due to the high demand and limited power production.

Only a few studies have investigated the impact of a flat-top-glass cover on PTC performance (Maree & Ismaeel, 2019; Ahmed et al., 2016). However, to our knowledge, none of the previous studies have compared the performance of a flat-top-glass-covered collector using two identical collectors working simultaneously on the same day. Bhujangrao used only one collector to take the measurements on two different days, which could affect the study results (Bhujangrao, 2015).

This work aims to investigate the effect of the top glass cover on the performance of a PTC prototype in Al-Bayda, Libya. This objective can be achieved by studying the temperature behavior of the absorber outer surface and heat transfer fluid of a covered and an uncovered PTC. The effect of the top cover on the thermal efficiency will also be investigated. The two identical parabolic solar collectors are run simultaneously with the same characteristics.

## MATERIALS AND METHODS

### Experimental work

Two identical prototype PTCs were designed and manufactured at the mechanical engineering laboratories at Omar Al-Mukhtar University. One of the PTCs was covered with a flat-top glass cover, and the other PTC was left without a glass cover (Figure 1). The parabola surface formula used for the designing and manufacturing of the reflecting surface is represented by equation (1) (Abed & Afgan, 2020; Ahmed et al., 2016; Price et al., 2002).

$$Y = \left(\frac{1}{4f}\right) X^2 \qquad (1)$$

Each PTC was made of a wood frame with an aperture area of 920 $cm^2$ (40 cm × 23 cm). The reflectors were glass mirror strips (40 cm × 2.5 cm) (Woodrow, 2016). The absorbers were made of

copper and had a 10 mm inside diameter and a 12 mm outside diameter. The heat transfer fluid used in both collectors was water flowing in a closed loop, from an iron tank to the collector and circulating back to the tank. Ambient temperature was measured using a liquid-in-glass thermometer, and the wind was measured using an Anemometer (TENMA 72-6638), while solar radiation was measured using a solar power meter (CEM- LA- 1017) in units of W/m$^2$. For the top covered collector, six thermocouples (k-type) were connected to the service unit, recording receiver inner and outer surface temperatures, inner and outer glass cover surface temperatures, and water temperatures at the inlet and outlet of the solar collector. The uncovered solar collector was connected to four thermocouples: receiver inner and outer surface and water temperatures at the inlet and outlet. To ensure that the flow rate in both collectors is the same, two identical internal liquid filter pumps (JY-600F) were used. At the beginning of the experiment, the flow rate was measured by dividing a collected volume in a bucket by the filling time to verify that the flow rate in both collectors was the same. All measuring devices used during the experimental work are detailed in Supplementary section S1, and all thermocouples, the service unit, the solar radiation meter, and the anemometer were calibrated at the beginning of this study.

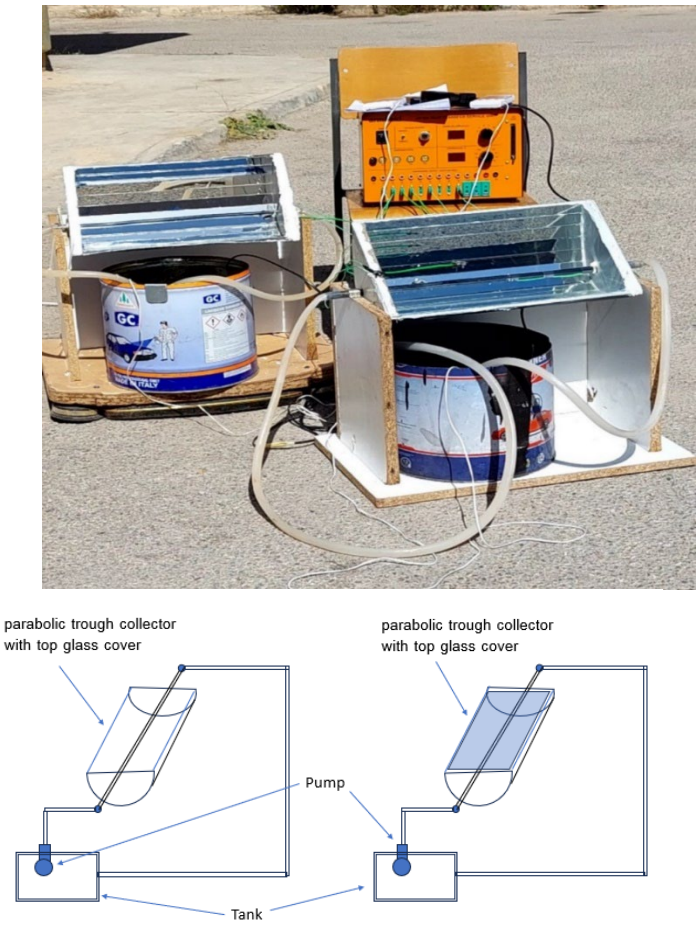


**Figure: (1).** Two identical PTC prototypes with and without a top glass cover during operation are shown schematically and in the testing setup.

One day was selected to conduct the measurements every month, preferably a blue-sky day. No measurements were taken for April because of the weather conditions. For the selected day, the tilt angle was calculated using equation (2), and the used MATLAB code is shown in supplementary C1 (Yadav & Chandel, 2013; Handoyo & Ichsani, 2013; Benghanem, 2011). More specifically, the

declination angle was first calculated based on the day number in the year, n. Secondly, since the collectors were oriented to the south, a zero-surface azimuth angle was used in calculations. The geographical latitude of 32.76272N (Al Bayda City) was used, and the hour angle was selected to be solar noon. As a result, the calculated tilt angle for both collectors will be identical and fixed for the entire day but change daily.

Both collectors were provided by protractors placed on the frame at the moving axis of the collector. The protractors give an accurate reading of the tilt angle for both collectors. After setting the collectors to the desired tilt and surface azimuth angle, measurements of receiver inner and outer surface temperatures, inner and outer glass cover surface temperatures, water temperatures at the inlet and outlet of the solar collector, wind speed, and solar radiation were recorded every 5 minutes. The volumetric flow rate was measured once in every experiment.

$$\tan\beta = \frac{(\cos\delta \sin\gamma \sin\omega - \sin\delta \cos\varphi \cos\gamma + \cos\delta \sin\varphi \cos\gamma \cos\omega)}{(\sin\delta \sin\varphi + \cos\delta \cos\varphi \cos\omega)} \qquad (2)$$

where,

$\beta$ Tilt angle
$\varphi$ Latitude
$\delta$ Declination angle
γ Surface azimuth angle
ω Hour angle
γ Solar azimuth angle

**Energy balance**

Equilibrium energy equations have been used to compare inlet solar energy with outlet valuable energy reaching the water tank to investigate the top glass cover effect on the parabolic trough solar receiver performance. Figure 2 and Figure 3 show schemes of two parabolic solar collectors, one with a top glass cover and the other without a top glass cover. Similarly, Figure 4 and Figure 5 show the thermal resistance network of heat flow (Forristall, 2003; Qu et al., 2007; Gong et al., 2010).

When the top glass is attached, the solar energy ($Q_i$) reaches the solar collector and hits the top glass. Some of this energy passes to the receiver tube, defined as actual solar energy ($Q_{act}$), while the rest of the energy is lost as optical losses. It is important to mention that the system is assumed to be in equilibrium, and all thermodynamic properties are uniformly distributed around the absorber. The optical losses are due to many factors, such as accumulating dust on the mirrors, blocking, and mirror reflectivity (Forristall, 2003).

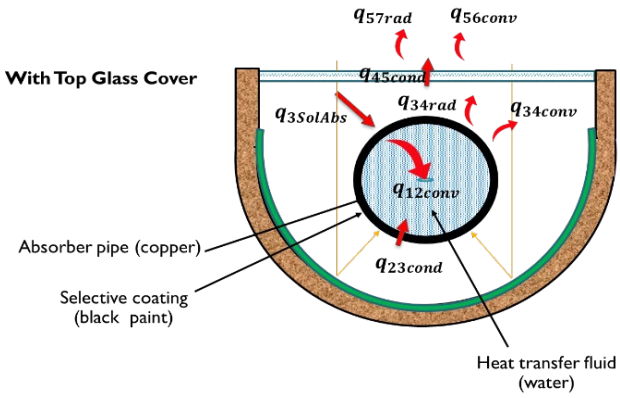


**Figure: (2).** Scheme of a parabolic solar collector covered with a top glass cover.

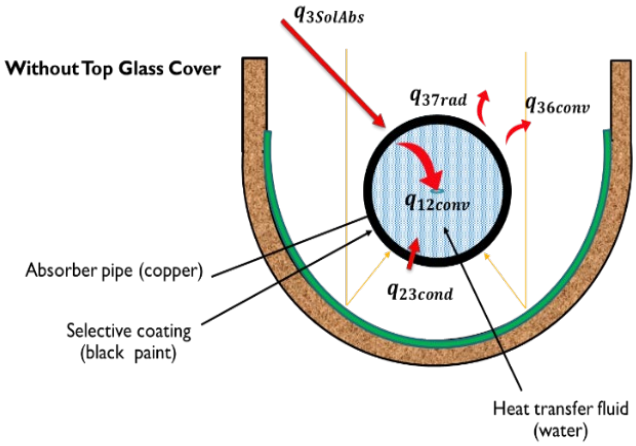


**Figure: (3).** Scheme of a parabolic solar collector without a top glass cover.

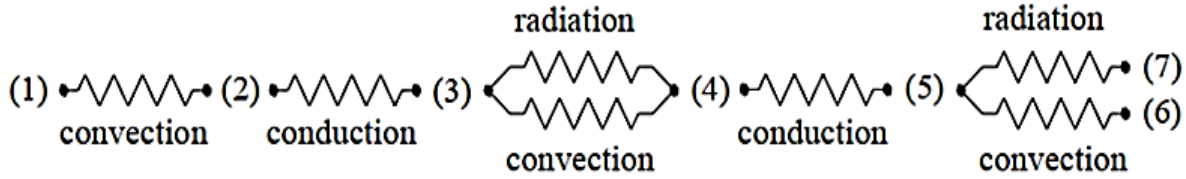


**Figure: (4).** Thermal resistance model of a 1-Dimension for a to glass covered parabolic solar collector.

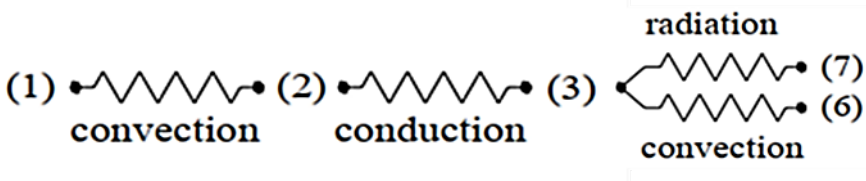


**Figure: (5).** Thermal resistance model of a 1- Dimension for a parabolic solar collector without a top glass cover

**Solar collector with a top glass cover**

In the case when the top glass cover is attached, the one-dimensional heat transfer equations are presented below (Brooks, 2005, Forristall, 2003):

$$Q_{12convection} = Q_{23conduction} \quad (3)$$
$$Q_{act} = Q_{34convection} + Q_{34radiation} + Q_{23conduction} \quad (4)$$
$$Q_{34convection} + Q_{34radiation} = Q_{45conduction} \quad (5)$$
$$Q_{45conduction} = Q_{56convection} + Q_{57radiation} \quad (6)$$
$$Q_{Heatloss} = Q_{56convection} + Q_{57radiation} \quad (7)$$

However, when no top glass cover is attached, the heat transfer model is reduced since the heat transfers from the receiver to the atmosphere directly:

$$Q_{12convection} = Q_{23conduction} \quad (8)$$
$$Q_{act} = Q_{36convection} + Q_{37radiation} + Q_{23conduction} \quad (9)$$
$$Q_{Heatloss} = Q_{36convection} + Q_{37radiation} \quad (10)$$

**Convective heat from the tube to water**

Heat is transferred from the inner surface of the receiver to the water via convection, as given by the following equation (Forristall, 2003):

$$Q_{12convection} = U_1 D_2 \pi (T_2 - T_1) \quad (11)$$

$$U_{1=} N_{uD_2} \frac{K_1}{D_2} \quad (12)$$

where,
$U_1$ = Coefficient of convection heat transfer
$D_2$ = Receiver inner diameter
$K_1$ = Water conductivity at $T_1$
$T_1$= Water average temperature
$T_2$= Inner surface temperature of the receiver
$Nu_{D2}$= Nusselt number based on inner diameter.

Based on the flow type (turbulent, transitional, or laminar), the model uses a suitable Nusselt number. In case of turbulent and transitional flow, the following equations are used to calculate the Nusselt number (de Oliveira Siqueira et al., 2014; Abed & Afgan, 2020; Forristall, 2003):

$$Nu_{D2} = \frac{Df_2/8 (Re_{D2} - 1000) Pr_1}{1 + 12.7 \sqrt{Df_2/8} \left( Pr_1^{\frac{2}{3}} - 1 \right)} \left( \frac{Pr_1}{Pr_2} \right)^{0.11} \quad (13)$$

$$Df_2 = \left( 1.82 \log_{10}(Re_{D_2}) - 1.64 \right)^{-2} \quad (14)$$

where,
$Df_2$ = Darcy–Weisbach friction factor
$Re_{D_2}$= Reynolds number
$Pr_1$ *and* $Pr_2$ = Prandtl number at the receiver's centerline and inner surface, respectively.

There are some important assumptions regarding the above equations. For example, the inner surface of the absorber is smooth, the turbulent range of the Reynolds number should be less than 5000000, and the Prandtl number, $Pr_1$, range should be less than 2000 (Forristall, 2003). If the flow is laminar (Re < 2300), the Nusselt number will be selected as 4.4 (Forristall, 2003).

**Heat conduction through the receiver tube**

The heat conduction through the wall of the receiver tube can be calculated using the following equation (Forristall, 2003; Gong et al., 2010):

$$Q_{23conduction} = 2\pi K_{23} (T_2 - T_3) / \ln \left( D_3 / D_2 \right) \quad (15)$$

where,
$K_{23}$= Copper thermal conductivity.
$D_3$ = Receiver outer diameter
$T_3$ = Outer surface temperature of the receiver

The thermal conductivity of copper used in the calculation is 400 W/m-K (Forristall, 2003).

**Heat flow from the receiver to the inner surface of the top glass cover**

Heat loss from the absorber to the inner surface of the top glass cover is caused by convection and radiation. Due to the presence of the top glass, the convection will be considered natural heat transfer only. The radiation heat flow also happens between the receiver and the top glass cover because of the temperature difference.

**Convection heat transfer from the receiver to the inside surface of the top glass cover**

The convection heat moving from the receiver's outer surface to the top glass cover is given by the equation below:

$$Q_{34convection} = U_{34} D_3 \pi (T_4 - T_3) \quad (16)$$

$$U_{34} = N_{uD_3} \frac{K_{34}}{D_3} \quad (17)$$

where,
$U_{34}$ = Ceofficient of convection heat transferCoefficient of convection heat transfer
$K_{34}$ = Air thermal conductivity
$T_4$ = Inner glass cover surface temperature
$N_{uD_3}$ = Nusselt number based on $D_3$ Nusselt number based on $D_3$

The following correlation can estimate the Nusselt number:

$$N_{uD_3} = \left( 0.60 + \frac{0.387 Ra_{D_3}{}^{1/6}}{\left(1 + \left(0.559/P_{r34}\right)^{9/16}\right)^{8/27}} \right)^2 \quad (18)$$

$$Ra_{D_3} = \frac{g\beta(T_4 - T_3) D_3{}^3}{\alpha_{34} v_{34}} \quad (19)$$

$$\beta = \frac{1}{T_{34}} \quad (20)$$

$$P_{r34} = \frac{v_{34}}{\alpha_{34}} \quad (21)$$

where,
$Ra_{D_3}$ = Rayleigh no. for air based on $D_3$.
$v_{34}$ = Kinematic viscosity for air at $T_{34}$
$\beta$ = Volumetric thermal expansion coeff.
$g$ = Gravitational constant
$\alpha_{34}$ = Thermal diffusivity for air at $T_{34}$
$P_{r34}$ = The prandtl number for air at $T_{34}$.

It is assumed that equation 16 is valid for Rayleigh numbers ranging from 500000 to $10^{12}$ (Forristall, 2003).

**Radiation heat moving from the receiver to the inside surface of the top glass cover**
The Radiation heat flow from the receiver to the top glass cover can be estimated by the equation below:

$$Q_{34radiation} = \sigma \pi \varepsilon_3 D_3 \left( T_3{}^4 - T_4{}^4 \right) \quad (22)$$

where,
$\sigma$ = Stefan-Boltzmann constant
$\varepsilon_3$ = The absorber selective coating emissivity

**Conduction heat transfer across the top cover**
Equation (21) estimates the flow of heat through the glass cover thickness.

$$q_{45conduction} = K_{45} A \frac{(T_4 - T_5)}{\Delta x} \quad (23)$$

where,
$K_{45}$ = Thermal conductance of glass at $T_{45}$
T5 = Outer glass cover surface temperature
$\Delta x$ = Glass cover thickness
A = Area of glass cover

**Heat between the top glass cover and the atmosphere**

The heat transferred from the outer surface of the top glass cover to the atmosphere is by convection and radiation. The convection will be forced if the wind blows on the top glass cover. If there is no wind, the convection will be natural (Forristall, 2003).

**Convection heat transfer from the outer surface of the top glass cover to the atmosphere**

Equation (22) is used to calculate the convection heat flow from the outside surface of the top glass cover to the the atmosphere as can be seen below:

$$q_{56convection} = UA(T_5 - T_6) \quad (24)$$

$$U = \frac{N_u K}{L} \quad (25)$$

where,

$K_5$ = Air thermal conductivity

$T_6$ = Ambient temperature

L = Length of glass cover

U = Convection heat transfer coefficient

**Convection heat transfer when wind is present**

The presence of the wind forces convection on the top glass cover. The Nusselt number will mainly depend on the flow type:

For Laminar case

$$N_u = \frac{hL}{K} = 0.332 {R_{e5}}^{1/2} {P_{r5}}^{1/3} \quad (26)$$

For Turbulent case

$$N_u = \frac{hL}{K} = {P_{r5}}^{1/3}(0.037 {R_{e5}}^{0.8} - 871) \quad (27)$$

where,

$Pr_5$ = Prandtl number evaluated at $T_5$.

$Re_{T_5}$= The Reynolds number based on $T_5$.

**Convection heat transfer when no wind is present**

When air is calm, the convection heat flow from the top cover to the atmosphere is considered free convection. In this case, the Nusselt number can be estimated via the following equation ($G_{r5}P_{r5} < 2 \times 10^8$ ) :

$$N_u = 0.13(G_{r5}P_{r5})^{1/3} \quad (28)$$

$G_{r5}$= The Grashof number based on $T_5$.

**Radiation heat transfer from the outside surface of the top glass cover to the surroundings**

The radiation from the top cover to the atmosphere is calculated using the equation below:

$$Q_{57radiation} = \sigma \varepsilon_5 A\left({T_5}^4 - {T_7}^4\right) \quad (29)$$

where,

$\varepsilon_5$ = Absorber selective coating emissivity

$T_7$ = sky temperature

It is important to mention that the sky temperature is calculated as eight degrees Celsius lower than the ambient temperature (Forristall, 2003).

**Solar collector without glass cover**

The convection and radiation heat transfer are lost directly to the environment without the glass

cover. With no wind, the convection is considered natural, and the equations (14 to 19) will be used. If wind is present, the convection heat flow from the receiving tube to the atmosphere is considered forced convection. In this case, the Nusselt number is calculated using the equation below (Forristall, 2003):

$$\bar{N}_{u_{D3}} = A\, Re_{D3}{}^{B} Pr_4{}^{C} \left(\frac{Pr_4}{Pr_3}\right)^{1/4} \qquad (30)$$

where,
$P_{r3}$ and $P_{r4}$ = The Prandtl number for air at $T_3$ and $T_4$ respectively
$Re_{D_3}$ = Reynolds no. for air based on D3

In equation (28), Reynolds number determines the variables A and B: For 1 < Re < 40, A = 0.75 and B = 0.4. For 40 < Re < 1000, A = 0.51 and B = 0.5. For 1000 < Re < 200000, A = 0.26 and B = 0.6. For 200000 < Re < 1000000, A = 0.076 and B = 0.7. The value depends on the Prandtl number. It is 0.37 when Prandtl equals or less than ten, and 0.36 when Prandtl is equal to or greater than 10.

**Theoretical and Experimental Efficiency**

The theoretical efficiency is the useful energy or heat gain ratio to the solar energy reaching the solar collector. The solar energy reaching the solar collector is calculated using the following equation (Abed & Afgan, 2020):

$$Q_i = I_b * A_{aperture} \qquad (31)$$

where,
$I_b$ = Solar radiation
$A_{aperture}$ = Area of the collector

Only a fraction of solar energy is received by the absorber. This fraction is called adequate solar energy. The rest of the solar energy is lost due to the optical efficiency of the collector, which depends on glass cover properties, mirror properties, and metal tube properties. Glass is not perfectly transparent, with some losses from reflection and absorption. The reflective losses depend on the incidence angle of the solar irradiation. Therefore, to understand the performance of a glass cover, it is essential to consider the following three valuable metrics: transmittance (τ), reflectance (ρ), and absorptance (α). For more information about solar radiation measurements and data, see supplementary D1.

The equation for the adequate solar energy becomes:

$$Q_{act} = Q_i * \eta_{opt} \qquad (32)$$

where,
Qi = Solar energy
$\eta_{opt}$ = Optical efficiency

Theoretical heat gain is the effective solar energy minus the heat transfer losses. Therefore, the theoretical heat gain is calculated using the equations:

$$Q_{Gain} = Q_{act} - Q_{loss} \qquad (33)$$
$$Q_{loss} = Q_{34convection} + Q_{34radiation} \qquad (34)$$

where,
$Q_{loss}$ = Heat losses
$Q_{34convection}$ = Convection heat transfer from the receiver to the inside surface of the top cover

$Q_{34radiation}$ = Radiation heat transfer from the receiver to the inside surface of the top cover

Finally, the theoretical efficiency can be estimated using the following equation (Abed & Afgan, 2020):

$$\eta_{Theoretical} = \frac{Q_{Gain}}{Qi} \quad (35)$$

To calculate the experimental efficiency, the solar energy reaching the collector is estimated using the same equation (29)(Brooks, 2005; Abed & Afgan, 2020; Kalogirou & Panayiotou, 2013). The experimental heat gain is calculated using the following equation:

$$Q_{Gain} = \dot{m} * C_p * (T_{in} - T_{out}) \quad (36)$$

where,

$\dot{m}$ = The flow rate of mass

$T_{in}$ = Water temperature at the outlet

$T_{out}$ = Water temperature at the inlet

$C_p$ = Water specific heat

The experimental efficiency of the PTC is the ratio of the heat gained to the solar energy reached by the collector. The experimental efficiency is calculated using equation 38 (Brooks, 2005; Kalogirou & Panayiotou, 2013):

$$\eta_{Experimental} = \frac{Q_{Gain}}{Qi} \quad (38)$$

## RESULTS AND DISCUSSION

### The water and absorber outside surface temperatures for the covered collectors

For the top-covered solar collector, measurements were taken during ten months in 2022, from February to December (except April). Figure 6 shows the water and absorber temperature change over time in February. See supplementary (S2) for water and absorber temperatures from March to December. In general, both water and absorber temperatures increased gradually with time. The absorber temperature was mainly higher than the water temperature.

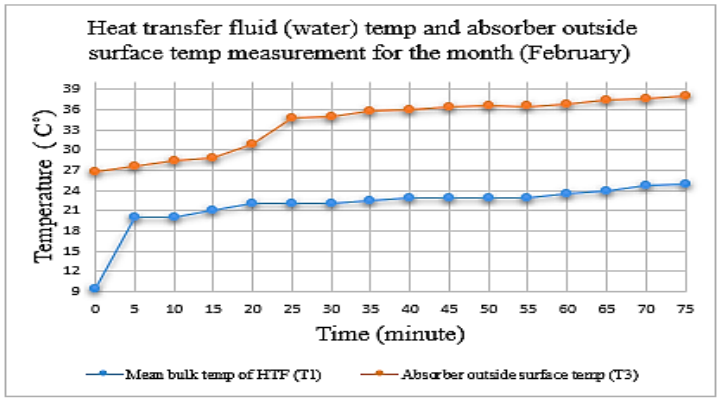


**Figure: (6).** Temperature of water and absorber outside surface during February.

### The impact of top glass cover on absorber outside surface temperature and heat transfer temperature

The two identical solar collectors were run simultaneously during October, November, and December. Figure 7 shows the impact of top glass cover on absorber outside surface temperature during December. Both absorber surface temperatures increased with time, as expected, but the top-covered collector showed a more stable temperature increase, while the solar collector without a

glass cover showed a fluctuating temperature increase. This is due to the impact of wind on the uncovered absorber. Supplementary S3 compares absorber outside surface temperatures of covered and uncovered PTCs for October and November.

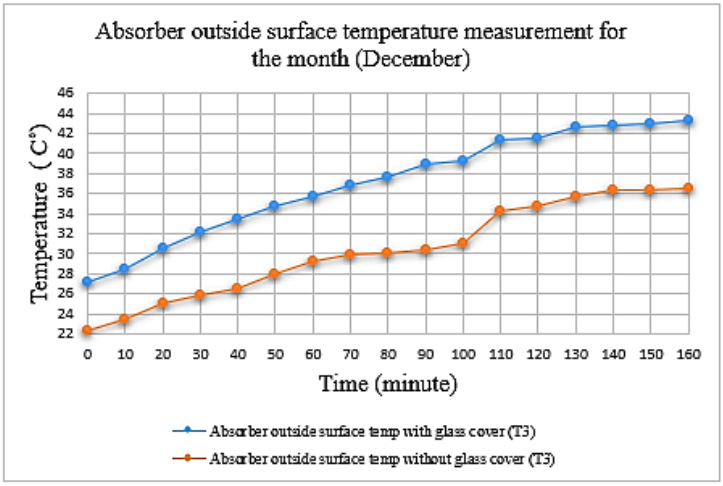


**Figure: (7).** Absorber outside surface temperature for the covered and uncovered collectors during December

Similarly, the top glass cover led to a higher water temperature than the uncovered PTC. Figure 8 shows the water temperature increase in a PTC with a top cover and an uncovered PTC during December. Similar comparisons for October and November are shown in the supplementary (S4).

The results showed that the top glass cover has a more significant effect on the absorber surface temperature than the water. The absorber surface temperature increased by 11%, while the water temperature increased by only 4% due to the presence of the top cover.

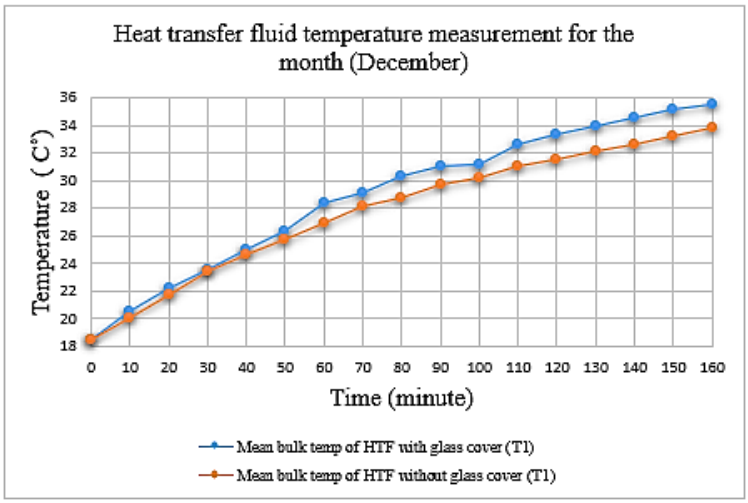


**Figure: (8).** Water temperature for the covered and uncovered collectors during December.

## The results of the PTC thermal efficiency

Another important objective of this work is to investigate the effect of the top glass cover on the thermal efficiency of the parabolic solar collector. All parameters used in the efficiency calculations were during November 2022. Figure 9 compares the theoretical thermal efficiency of a covered and uncovered parabolic trough solar collector. The maximum theoretical thermal efficiency was 56.9%, and the maximum experimental efficiency was 50.4%. The theoretical thermal efficien-

cy increases by 5% due to the presence of the top glass cover. The experimental thermal efficiency increased by less than 4% when the top cover was attached (Figure 10).

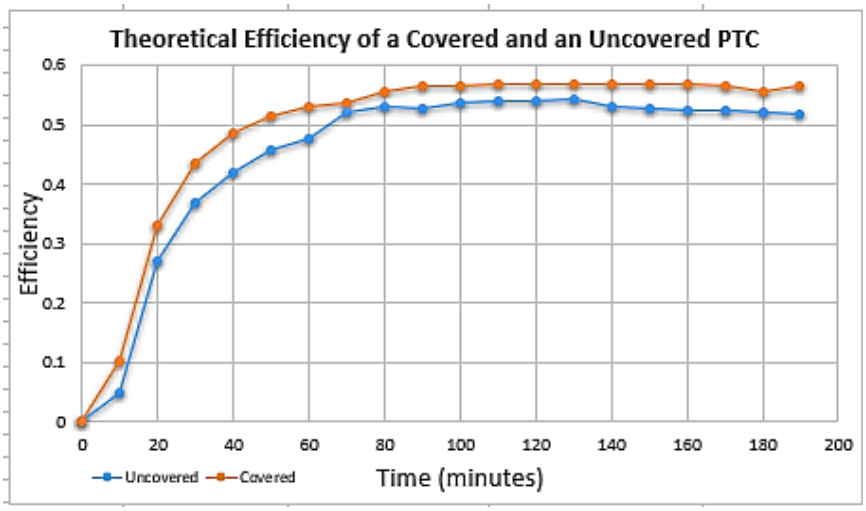


**Figure: (9).** Theoretical thermal efficiency of the covered and uncovered PTC

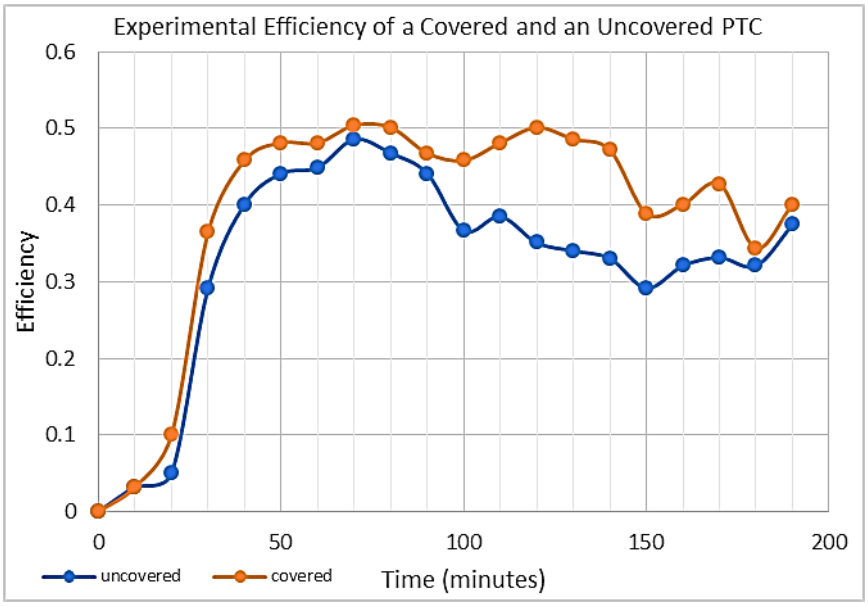


**Figure: (10).** Experimental thermal efficiency of the covered and uncovered PTC

Even though the temperature continuously increases with time, as shown in Figures 6,7, and 8, the theoretical thermal efficiency remains almost constant after about 80 minutes. Initially, the temperature is slightly low, meaning low heat loss. Therefore, the efficiency increases since the ratio of energy gained to available energy increases. On the other hand, as the temperature increases (after 80 minutes), the heat loss also increases, leading to a constant overall efficiency value. This is not entirely unusual; several previous studies have reported a significant correlation between thermal efficiency and solar radiation, indicated by an increase before noon, which remains almost constant for a short period before it decreases when the solar radiation becomes weaker. Singh et al. (2012), who designed an aluminum-framed parabolic trough collector with a reflecting mirror (1.2 m × 0.05 m), found that the efficiency increased until 10 am. It decreased until 1 pm. The maximum efficiency was relatively low (21%) (Singh et al., 2012).

The findings of this study about the maximum efficiency value are also consistent with previous studies. Brooks (2005) studied the performance of a PTC and found the maximum efficiency was 55.2% for an unshielded absorber (Brooks, 2005), Qu et al. (2006) reported that the maximum efficiency was 55% (Qu et al., 2007). Ahmed et al. (2016) found that the maximum efficiency of a PTC installed in Sabratha, Libya, was 43.9% (Ahmed et al., 2016). In Erbil, a city in Iraq, Maree and Ismaeel (2019) studied theoretical and experimental efficiency. They showed that the thermal efficiency decreased with time, and the maximum efficiency was pretty high (74%) (Maree & Ismaeel, 2019).

A closer look at Figure 10 shows a fluctuating decrease in the experimental thermal efficiency after about 80 minutes. There are a number of possibilities that could explain this unexpected behavior. Since thermal efficiency is strongly dependent on solar radiation, operating conditions, and optical losses, the efficiency decrease may be associated–in part–with the decrease in solar radiation that happened after 10:30 am (80 minutes) on Nov 10th, 2022 (please see supplementary D1 for the solar radiation data). However, this decrease does not explain the two drops at 100 and 150 minutes, which happened for covered and uncovered collectors, indicating that this was not due to the wind effect. These drops could be due to operation conditions such as laminar and turbulent flows.

## CONCLUSION

The study aimed to design and manufacture two identical parabolic trough solar collectors with and without a top glass cover. The two collectors were manufactured and tested in the Mechanical Engineering Laboratories at the University of Omar Al-Mukhtar in Albayda, Libya. The effect of the top glass was studied, and the theoretical and experimental thermal efficiency of the solar collector was studied when the top glass was attached.

The results showed that both the absorber surface and the water temperatures gradually increased with time in both collectors. The top-covered collector showed a higher maximum absorber surface temperature (11%) and higher maximum water temperature (4%) than the temperatures of the uncovered collector. As expected, the absorber surface temperature was always higher than the water temperature.

The thermal efficiency comparison was conducted in November 2022. Installing the top-glass cover led to a gain in theoretical thermal efficiency by 5% and in experimental thermal efficiency by 4%. The results also showed that the maximum theoretical efficiency was 56.9%, and the maximum experimental efficiency was 50.4%. The efficiency values obtained in this study were consistent with many lab-manufactured PTCs but lower than some commercial PTCs. The findings provided in this study are crucial in providing a cost-effective PTC that can be an alternative energy source, especially in developing countries such as Libya. We recommend that future studies improve the reflecting mirrors and increase the size of the prototype. To reduce the experimental cost of the improved design, it is recommended that the collector efficiency or the output temperature is predicted using either statistical modeling or independent variables from artificial neural networks such as solar radiation, input temperature, and ambient temperature.

## ACKNOWLEDGEMENT

The authors would like to thank the Mechanical Engineering Department at Omar Al-Mukhtar University for supporting the project. The authors thank Mr. Fadeel Al-Areeda for lending the solar power meter.

**Duality of interest:** The authors declare that they have no duality of interest associated with this manuscript.

**Author contributions:** Hasan A. H. Husayn: performed, Conceptualization, Methodology, Software, Validation, Formal analysis, Resources, Data curation, Writing – original draft, review and editing. Mohamed Eltarkawe: performed, Conceptualization, Methodology, Writing – review & editing, Supervision, Project administration.

**Funding:** No specific funding was received for this work.

## REFERENCES

Abed, N., & Afgan, I. (2020). An extensive review of various technologies for enhancing the thermal and optical performances of parabolic trough collectors. *International Journal of Energy Research*, *44*(7), 5117-5164.

Ahmed, A. M., Albusefi, A. A., & Izweik, H. T. (2016). Experimental Evaluation of a Solar Parabolic Trough Collector under Libyan climate. *Int. J. Eng. Trends Technol*, *38*(1), 32.

Benghanem, M. J. A. E. (2011). Optimization of tilt angle for solar panel: Case study for Madinah, Saudi Arabia. *Applied Energy*, *88*(4), 1427-1433.

Bhujangrao, K. H. (2015). Effect of top glass cover on thermal performance of cylindrical parabolic collector. *International Research Journal of Engineering and Technology*, *2*(8), 2015.

Brooks, M. J. (2005). *Performance of a parabolic trough solar collector* (Doctoral dissertation, Stellenbosch: University of Stellenbosch).

de Oliveira Siqueira, A. M., Gomes, P. E. N., Torrezani, L., Lucas, E. O., & da Cruz Pereira, G. M. (2014). Heat transfer analysis and modeling of a parabolic trough solar collector: an analysis. Energy Procedia, 57, 401-410.

Fernández-García, A., Zarza, E., Valenzuela, L., & Pérez, M. (2010). Parabolic-trough solar collectors and their applications. *Renewable and sustainable energy reviews*, *14*(7), 1695-1721.

Forristall, R. (2003). *Heat transfer analysis and modeling of a parabolic trough solar receiver implemented in engineering equation solver* (No. NREL/TP-550-34169). National Renewable Energy Lab.(NREL), Golden, CO (United States).

Gong, G., Huang, X., Wang, J., & Hao, M. (2010). An optimized model and test of the China's first high temperature parabolic trough solar receiver. *Solar Energy*, *84*(12), 2230-2245.

Hachicha, A. A. (2013). Numerical modelling of a parabolic trough solar collector.

Handoyo, E. A., & Ichsani, D. (2013). The optimal tilt angle of a solar collector. *Energy Procedia*, *32*, 166-175.

Ibrahim, I. D. (2020). Development of Smart Parabolic Trough Solar Collector for Water Heating and Hybrid Polymeric Composite Water Storage Tank. *Université Paris-Saclay; Tshwane University of Technology*.

Islam, M. T., Huda, N., Abdullah, A., and Saidur, R. (2018). A comprehensive review of state-of-the-art concentrating solar power (CSP) technologies: Current status and research trends. *Renewable and Sustainable Energy Reviews*, 91, 987-1018.

Kalogirou, S. A., & Panayiotou, G. (2013). Experimental investigation of the performance of a Parabolic Trough Collector (PTC) installed in Cyprus. *In 2nd Conference on Power Options for the Eastern Mediterranean Region*.

Maree, I. E., & Ismaeel, A. G. (2019). Experimental and theoretical calculation of efficiency for flat plate solar collectors in Erbil City. *Periodicals of Engineering and Natural Sciences*, *7*(2), 786-793.

Price, H., Lu¨ pfert, E., Kearney, D., Zarza, E., Cohen, G., Gee, R., & Mahoney, R. (2002). Advances in parabolic trough solar power technology. *J. Sol. Energy Eng.*, *124*(2), 109-125.

Qu, M., Archer, D. H., & Yin, H. (2007, January). A linear parabolic trough solar collector performance model. In *Energy Sustainability* (Vol. 47977, pp. 663-670).

Singh, S. K., Singh, A. K., & Yadav, S. K. (2012). Design and fabrication of parabolic trough solar water heater for hot water generation. *International Journal of Engineering Research & Technology (IJERT)*, *1*(10), 1-9.

Tian, Y., & Zhao, C. Y. (2013). A review of solar collectors and thermal energy storage in solar thermal applications. Applied energy, 104, 538-553.

Woodrow, O. R. (2016). *Characterisation of a Parabolic Trough Collector Using Sheet Metal and Glass Mirror Strips*. University of Pretoria (South Africa).

Yadav, A. K., & Chandel, S. S. (2013). Tilt angle optimization to maximize incident solar radiation: A review. *Renewable and sustainable energy reviews*, *23*, 503-513.

Al-Mukhtar Journal of Engineering Research 08 (1): 51-64, 2024
Doi: https://doi.org/10.54172/95e7n966

Research Article

Open Access

# The effect of Curing time and temperature on Cathodic Disbondment Behavior of Epoxy-Coated Steel in Marine Environments

**Rafaa M. R. Esmaael *, Dawod H. Elabar [2], Mohamed A. Gebril [3], Farag Haidar [4]**

***Corresponding author:** rafaa.esmaael@omu.edu.ly, Department of Material Science and Engineering, Faculty of Engineering, Omar Al-Mukhtar University, Libya

[2] Environmental and biological chemistry research center (EBCRC), Tocra, University of Benghazi, Libya

[3, 4] Department of Mechanical Engineering, Faculty of Engineering, University of Benghazi, Libya

**Received:**
09 September 2024

**Accepted:**
05 December 2024

**Publish online:**
31 December 2024

## Abstract

Protecting steel structures from corrosion in various environments typically involves coating and cathodic protection. Multiple factors affect the rate at which a coating disbonds, including curing time, temperature, surface preparation, and coating thickness. Numerous research studies have investigated the mechanisms behind blister formation and growth. This study focuses on how the curing temperature affects the number of blisters, blister diameters, and disbanded steel coated with a 100µm epoxy resin. The results show that as the curing time increases for cathodically protected and unprotected samples, the time taken for initial disbonding is prolonged. It is worth noting that the blistering time is longer in polarized samples than in non-polarized ones, regardless of the curing temperature. In addition, blister formation is less frequent in polarized samples than non-polarised ones. As the curing temperature increases, the disbonding area decreases in protected and cathodically unprotected conditions. It has been observed that the size of blisters decreases with higher curing temperatures in protected samples. At the same time, it increases with rising cure temperatures when the system is in protection mode. Notably, the disbonding rates in unprotected samples exceed those in protected samples at all curing temperatures.

**Keywords:** Epoxy Resin, Coating Disbonding, Sacrificial Anode, Cure Temperature, Marine Environment, Cathodic Protection.

## INTRODUCTION

The primary purpose of applying anticorrosive coatings to metallic surfaces, such as steel, is to slow down or impede the natural occurrence of corrosion when exposed to corrosive environments. These coatings comprise several crucial elements, including binders, pigments, fillers, additives, and carriers. They are created using a combination of chemicals and materials in various formulations. Additives can be included in small amounts to improve specific coating properties or address technical problems (Cheng, Fu, Dou, Chen, & Liu, 2023). The carrier acts as a vehicle for the uncured paint constituents but does not play a critical role in the protective mechanisms of the coatings. Besides breaking down the components, the carrier lowers the viscosity of the coating, making it easier to spray or dip. The carrier can be an organic solvent, water, or gas, depending on the type of coating. In liquid form, the carrier is mainly responsible for ensuring adequate coating wetness, thereby controlling film uniformity. Insufficient wetting can result in unprotected areas and film holes (Njoku, Cui, Xiao, Shang, & Li, 2017; Thierry, 2020; Zhang et al., 2018).

The binder provides physical support and containment for pigments and additives, binding these components to the metal surface. Besides providing structure, the binder is crucial for a coating's fundamental properties, such as adhesion to metal, internal cohesion, high mechanical strength, and low permeability. (Knudsen & Forsgren, 2017) .Selecting the correct binder is crucial, as its properties depend on its chemical composition and curing process. The advantages and disadvantages of the chosen binder family play a significant role in coating performance. (Ma, Ammar, Kumar, Ramesh, & Ramesh, 2022) Three pigments are used in anticorrosive coatings: barrier, sacrificial, and inhibitive. They differ in their protective mechanisms and the quantities used in the coating. Sacrificial coatings, such as zinc-rich coatings, need a significant amount of pigment to establish electrical conductivity between the particle and the substrate for protection. Inhibitive pigments rely on the formation of soluble salts at the substrate/paint interface, so they must be present in adequate quantities to facilitate dissolution mechanisms.

Pigments in barrier coatings are chemically inert and act as a barrier against corrosion. (Agwa, Iyalla, & Abu, 2017; Ashassi-Sorkhabi, Moradi-Haghighi, Zarrini, & Javaherdashti, 2012). The quantity and type of pigments significantly influence the mode of protection offered by the coatings, highlighting the importance of selecting the appropriate pigment type and quantity based on the desired protective mechanisms and coating performance. (Kumar & Bhattacharya, 2020; Ramezanzadeh, Bahlakeh, Ramezanzadeh, & Rostami, 2019) Organic coatings are one of the most widely utilized corrosion reduction techniques, and they stand as a prevalent method for inhibiting corrosion in various environments. Adhesion to the substrate is a crucial factor that significantly influences the efficiency of organic coatings as corrosion inhibitors. It is a critical aspect affecting the performance of the coating. (Yu et al., 2021) In recent years, significant efforts have been directed towards enhancing the interaction between surfaces and composite material matrices. Various strategies have been explored for surface modifications aimed at improving interfacial adhesion.

Several methods to achieve the desired result include coatings, in-situ synthesis, and chemical grafting. Several researchers have suggested that hydroxyl ions formed beneath the disbonded coating are responsible for disrupting the bond between the coating and the substrate. (Eyckens et al., 2020; Leng, Streckel, & Stratmann, 1998; Qian & Cheng, 2018). Furthermore, it has been proposed that the diffusion of alkali metal cations accelerates disbonding by supplying them to the disbonding front through the aqueous phase at the interface of the polymer coating. (Rozenfel'd, Rubinshtein, & Zhygalova, 1987; Zhu & Van Ooij, 2002) The initial phase of the cathodic disbonding process is believed to involve water permeation, with the pathway for water movement speculated to occur through channels, capillaries, or pores within the coating. These structural irregularities may arise from the inhomogeneity of curing, impurity particles, or the solubilization of constituents in the coating. (Sato, 1981)

Paint films are not entirely barriers against corrosion agents such as water, oxygen, and ions. They are not impervious to these agents (Hammond, Holubka, DeVries, & Dickie, 1981; Shi et al., 2021) In some cases, the coating film allows too much water and oxygen to pass through, even more than what is typically observed in unpainted metals' corrosion rates. This excessive permeation indicates that factors other than water and oxygen penetration may also contribute to the corrosion rate. If the films of a metal-paint system have low ion diffusion characteristics, it could cause the accumulation of ions at the metal-paint interface due to corrosion reactions. In this case, the formation of hydroxyl ions can result in localized blistering and adhesion issues. This is because the ions struggle to diffuse out easily. Although the corrosion rate may not

be determined by water penetration, it can result in loss of adhesion in a wet state, which could be the deciding factor. Some researchers have suggested that there is a link between the start time and the infiltration of water into the interface. They propose that this infiltration must happen before the disbonding occurs (Chen, Li, Du, & Cheng, 2009; Gaylarde, Morton, Loh, & Shirakawa, 2011; H Leidheiser & Funke, 1987; Leidheiser Jr, Wang, & Igetoft, 1983; Schwenk, 1981; Tsay, 1988)

When steel is polarised cathodically in aerated water, it triggers reactions of oxygen reduction or hydrogen evolution. Two reactions increase pH near the electrode surface.(Babić & Metikoš-Huković, 1993; Esquivel, Olivares, Gayosso, & Trejo, 2011; Jovancicevic & Bockris, 1986) Studies show that the pH in blisters can reach 14. It has been suggested that the disbonding process is associated with a highly alkaline solution (high pH) that exists between the coating and the metal substrate (Koehler, 1984; Henry Leidheiser, 1981) Degradation and potential failure can occur during service due to several factors. There are several reasons why coatings on steel substrates can fail. These may include insufficient surface preparation, inadequate coating application, mechanical damage from backfilling, and stress, among other possible factors. (LeBozec, Thierry, & Pelissier, 2018).

This study aims to investigate how the curing time of epoxy resin, when used on a steel substrate and combined with cathodic protection in seawater, impacts the disbonding process. The presence or absence of a connection to an aluminum alloy sacrificial anode is also considered. Specifically, a 6 mm defect deliberately created in the coating facilitates ingressing water, oxygen, and reactive ions to the metal substrate. This condition leads to easier cathodic disbonding, which varies among samples due to differences in curing temperatures and whether the sample was subjected to polarization. The investigation examines the impact of curing temperatures and polarization while keeping coating thickness, potential, bath temperature, coating type, and substrate nature constant across all samples. The results show a clear correlation between initiation time and curing temperature.

## MATERIALS AND METHODS

### Working electrode

In electrochemical experiments, the working electrode is where redox reactions occur. Cold-rolled mild steel plates measuring 0.8mm in thickness, 15mm in length, and 7.5mm in width were used for this experimental investigation. This study chose mild steel plates based on their frequent use as the primary construction material in marine environments.

### Reference electrode

The reference electrode is an essential component in electrochemical experiments. It stabilizes and produces a known electrical potential against which the working electrode's potential is measured. The study utilized a standard laboratory-type saturated calomel electrode (SCE) as a reference electrode to ensure accurate and reproducible electrochemical measurements. The Standard Calomel Electrode (SCE) is a widely used reference electrode in electrochemical measurements owing to its stability and precise potential value. It plays a crucial role in maintaining a consistent electrical potential, against which the working electrode's potential can be accurately measured in various electrochemical analyses and experiments.

### Sacrificial anode

A sacrificial anode is a metal component intentionally placed within a system or structure to protect other important metal surfaces from corrosion. It functions as a sacrificial element by

readily corroding instead of the metal it is meant to protect. This effectively prevents corrosion on the protected surface and prolongs the life of the metal structure. Usually made of a metal or alloy that naturally corrodes, the sacrificial anode is connected electrically to the metal it protects. When an object is submerged in an electrolyte like seawater or soil, the sacrificial anode corrodes preferentially, releasing electrons that flow to the protected metal, effectively suppressing its corrosion. In this work, aluminum sacrificial anodes were used. The table below shows the anode composition provided by Trident Alloys Ltd for Imp Alloy III, an Al-Zn-In alloy.

**Table (1).** Composition of anode alloy

| Element | Zn | In | Fe | Si | Cu | Ga | Ti | Al |
|---|---|---|---|---|---|---|---|---|
| Composition wt.% | 4.5 | 0.0175 | 0.083 | 0.086 | 0.0024 | 0.0082 | 0.0198 | Remainder |

## Paint

During the experiments, epoxy resin paint from H. MARCEL GUEST Ltd have been used. To apply the paint, the base lacquer mixed with the hardening or curing agent in a 3:1 weight ratio, following the supplier's recommended instructions for preparation and application. The applied paint consisted of a chlorinated rubber "high build-up protective coating" and a mixture of beeswax and colophony resin in a ratio of 3:1. The experiment's electrolyte was a 3% sodium chloride solution.

## Equipment

For the experiments, the potential difference was measured using a high-resistance digital voltmeter. The electrochemical cell was made by using a 15-liter plastic tank, which is shown in Figure 1. To measure the thickness of the dry paint, an Elcometer 256FN instrument was used.

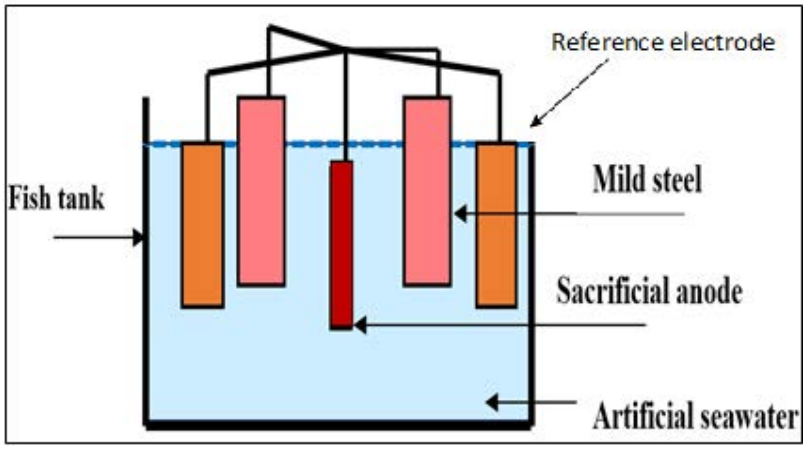


**Figure.(1).** The electrochemical cell

## Sample preparation

The process involved a necessary degreasing step to eliminate all traces of grease from the plates. This was achieved by wiping all the plates multiple times with ethanol and drying them using a stream of hot air until completely dry.

## Coating procedures

After blending the lacquer and hardener in a 3:1 ratio, entrapped air bubbles were eliminated by gently mixing the mixture and leaving it undisturbed for 10 to 15 minutes before application. In

order to achieve a smooth and even surface for application, a waiting period was necessary. To attach the plate to the steel plate and achieve the desired wet film thickness, two pieces of cellophane tape were overlapped on both sides of the panel. A small quantity of paint was poured onto the top edge of the plates. Then, a drawbar spreads the paint evenly, ensuring a consistent and reproducible coating thickness. The painted plates were left to cure at room temperature for one hour. Four samples underwent two different conditions:

1. Four samples were left at room temperature for three days.
2. four samples were subjected to 50°C in an oven for three days.
3- Four samples underwent different heating conditions: two sets were placed in an oven at 80°C and 100°C for two days, and another set was placed in an oven at 100°C for three days.
4- Three samples were placed in an oven at 100°C for four days.

The impact of different curing temperatures and durations on painted plates was examined under varying conditions.

**Thickness measurement**

The dry paint thickness for each sample was measured at various points across the coated panels, and the average was calculated to fall within the range of 100µm. The Elcometer model number 256FN was used to measure paint thickness accurately.

**Final Sample Preparation**

An intentional defect was created in the coated samples by drilling a 6mm diameter hole in the paint. Three coats of chlorinated rubber were applied to protect the edges and rear of the painted plates, with drying time allowed between each coat. A layer of beeswax mixed with colophony resin was applied over the chlorinated rubber, protecting only the painted area from the bath environment. "To investigate the effect of curing temperature on the disbonding rate, all aspects related to the material and preparation of specimens, including the type and thickness of the coating, the sodium chloride bath, the sacrificial anode, and other variables, were kept consistent across all test sets." The only variables that changed were the curing temperature and whether the samples were polarized through the aluminum sacrificial anode or were left unpolarized.

**Cathodic Polarization**

The schematic diagram in Fig.1 shows the experimental setup. The samples were connected to the sacrificial anode. In contrast, one sample from each curing condition was left unconnected to the sacrificial anode, which is left in an "open circuit" condition. The painted samples were subjected to an electrochemical cell setup using an aluminum alloy sacrificial anode to induce cathodic polarization. This polarization occurred at approximately -1.1 volts concerning the saturated calomel electrode (SCE) while maintaining room temperature.

**Cathodic Disbonding Measurement**

After a certain period, the samples that had been coated were removed from the bath and rinsed with distilled water. Then, they were gently wiped with tissue paper. Transparency sheets were placed over the samples to trace the disbonded areas accurately. Systematic measurements and tracing of disbanding areas were conducted to monitor their progression over time.

## RESULTS AND DISCUSSION

Table 2 shows the time it takes for blisters to form at different curing temperatures. The samples were tested with and without connection to a sacrificial anode.

**Table (2).** Effect of curing temperature on the blistering initiation time

| Blister initiation time (hours) | Curing temperature | | |
|---|---|---|---|
| | Room temperature | 50 °C | 100 °C |
| $T_o$ hours "polarized samples" | 108 | 240 | 288 |
| $T_o$ hours "not polarized samples" | 48 | 98 | 144* |

$T_o$ is blistering initiation time per hours
* for this cure temperature, no blister appeared during the experiment, but the artificial defect diameter gradually increased.

Table (2) shows that curing temperature significantly affects blister initiation time for polarized and nonpolarized systems. The data indicates that blister initiation time increases with higher curing temperatures. It was observed that the samples that were not polarized started to disbond earlier than the polarized samples. This shows that polarization effectively delayed the disbonding process, making it clear that it had a protective influence in this experimental setup. The change in blister number with time (dn/dt) as a function of curing temperatures is presented in Table (3). It shows a distinct pattern in the number of blisters observed in polarized samples.

**Table (3).** Change in blister number as a function of curing temperatures

| Change in blister Number | Curing temperature | | |
|---|---|---|---|
| | Room temperature | 50 °C | 100 °C |
| dn/dt "polarized samples" | 0.09 | 0.08 | 0.015 |
| dn/dt "not polarized samples" | 0.104 | 0.11 | ---* |

dn/dt is the change in blister number as a function of immersion time
*No blisters appeared, and the diameter of the defect increased gradually.

As the curing temperature increases, the number of blisters decreases. On the other hand, in the open circuit system, the number of blisters remains relatively consistent between samples cured at room temperature and those cured at 50 °C. Interestingly, there were no blisters observed in samples that were cured at 100 °C in the open circuit system during this experiment. This difference in blister formation between the two curing temperatures suggests that temperature varies depending on blister formation, especially when no polarization is present. In this specific experiment for the open circuit system, it was observed that no blisters appeared in samples cured at 100 °C. This discrepancy in the blister formation between curing temperatures may suggest that temperature has varying effects on blister formation, especially when there is no polarization. For all samples and different cured temperatures, the number of blisters increased with immersion time, regardless of whether the samples were polarized with the sacrificial anode or at the open circuit with the sacrificial anode, as shown in Fig. 2. The observed trends in blister initiation for the polarized and open circuit systems, at varying curing temperatures, reveal unexpected findings.

In the polarized system, samples cured at room temperature initiated more disbonding than those cured at 50 °C and 100 °C, with the latter exhibiting the least initial blistering. This trend contradicts the assumption that samples cured at higher temperatures should have fewer initial blisters, as the unprotected system shows. Samples cured at 50 °C in the open circuit showed a higher number of initial blisters as compared to those cured at room temperature. This finding contradicts the conventional expectation that samples cured at room temperature should have more initial blisters than those cured at 50 °C. These unexpected observations may indicate intricate interactions among curing temperature, polarization, and the blister initiation process. Other factors in this experimental setup that are not yet fully understood could have an influence as well. Samples that were polarized and cured at room temperature started to disbond with more initial blisters than those cured in an open circuit at the same temperature. However,

samples cured at 50 °C in a polarized system started to disbond with the same number of initial blisters as those cured in an open circuit system. Blisters increased more in an open circuit system than in the polarized system at all curing temperatures over time.

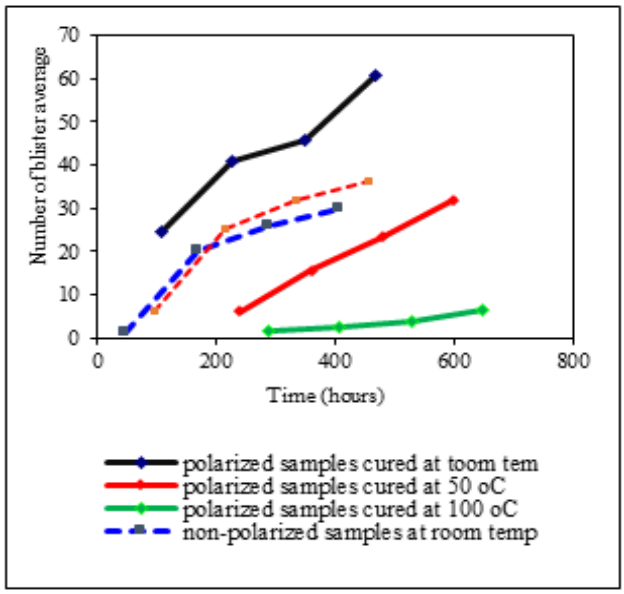


**Figure (2).** Average number of blisters as a function of time

Fig. 3 shows a significant impact of curing temperature on initial disbonding areas observed in the samples. Disbonding started after 108 hours in the polarized samples cured at room temperature, with an initial disbonding area of approximately 67 mm². Samples cured at 50 °C showed disbanding initiation after 240 hours, with a disbonding area of 39 mm², whereas those cured at 100 °C displayed disbanding after 288 hours with an approximate disbonding area of 7 mm². In the samples where the sacrificial anode was used, disbonding started after 48 hours, and the initial disbonding area was three mm². For the samples cured at 50 °C, disbonding started after 96 hours, and the disbonding area was 64 mm². However, disbanding was not observed in the samples cured at 100 °C during the experimental duration.

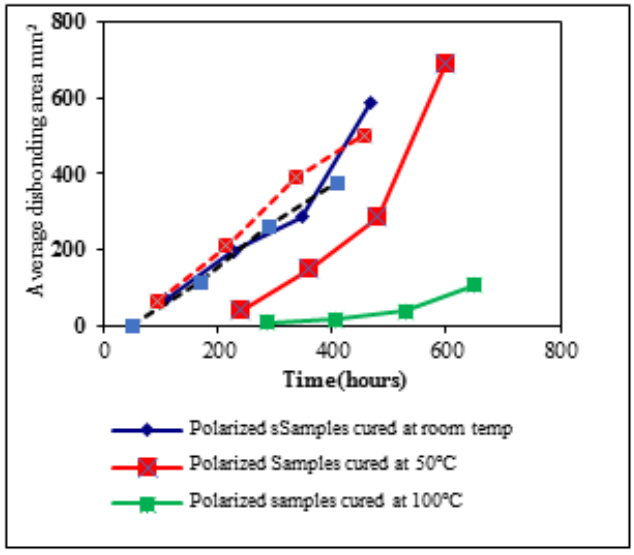


**Figure (3).** Average desponding area as a function of time

The results highlight the significant effect of the curing temperature on the initiation and extent of disbonding. These findings indicate a consistent pattern where higher curing temperatures lead to delayed disbonding initiation and reduced initial disbonding areas in both open circuit and polarized systems.

Fig.3 shows that samples cured at room temperature disbonded earlier than polarized samples despite exhibiting similar disbonding rates initially. After around 350 hours, there was a noticeable rise in disbonding rate for the polarized samples. However, the disbonding rate for the open-circuit samples remained pretty consistent. Additionally, the open circuit samples cured at 50 °C started to disband earlier and with a larger initial area than the polarized samples. Initially, both systems had a similar disbonding rate. However, after 480 hours, the polarized samples showed a significant increase in disbonding rate, diverging from the consistent rate observed in the open circuit samples.

The polarized and open circuit samples showed divergent disbonding behavior over time despite their initial similarities in disbonding rates. This shift became particularly evident during extended durations, showcasing a distinct change in disbonding rates between the two systems. The pivotal moment was the significant increase observed in the disbonding rate of the polarized samples. The disbonding rate in closed-circuit samples showed a significant increase, in contrast to the relatively consistent and sustained disbonding rate observed in open-circuit samples. This difference highlights the dynamic nature of disbonding behavior and how factors like polarization status and other variables can influence it. It also emphasizes that the evolution of disbonding rates over time can be significantly influenced by these factors in this experimental context. The information presented in Table 4 illustrates the effect of curing temperature on disbonding rates (dA/dt).

The samples were cured over three days. The results indicate that polarized samples cured at 100°C exhibited a lower disbonding rate than those cured at 50°C and ambient temperature. However, there was only a marginal difference in disbonding rates between samples cured at 50°C and those cured at ambient temperature. This experiment demonstrates that a higher curing temperature of 100°C significantly reduces the disbonding rate in polarized samples. This highlights the importance of curing conditions on disbonding behavior in this experimental setup.

**Table (4).** Change in disbonding rate with relation to curing temperature

| Curing temperature | Room temperature | 50ºC | 100ºC |
|---|---|---|---|
| (dA/dt) $mm^2$/hrs “polarized samples” | 1.63 | 1.44 | 0.33 |
| (dA/dt) $mm^2$/hrs “not polarized samples” | 2 | 1.54 | ---* |

*The change in the artificial defect diameter was tiny

The table data indicates that curing temperature significantly impacts the disbonding rate in open circuit samples. A clear trend exists where the disbonding rate decreases with increasing curing temperature. Higher curing temperatures are linked to lower disbonding rates in open-circuit samples. Furthermore, comparing open circuit and polarized samples reveals interesting findings. In particular, when the samples were cured at room temperature, it was observed that the rate of disbonding in the open circuit samples was significantly higher than that in the polarized samples. However, when the samples were cured at 50°C, the data did not show a significant difference in the disbonding rates between the open circuit and polarized samples. This highlights the intricate relationship among curing temperature, polarization status, and their im-

pact on disbonding rates, demonstrating varying effects in diverse scenarios. Table 5 shows how the average blister diameter changed over time for all samples under different conditions as a function of curing temperature. Consistent with all samples and conditions tested in the experiment, the observed trend shows that blister diameter increases with time. This implies that blister diameters grow or enlarge consistently and progressively over time, regardless of curing temperature or other studied variables.

**Table (5).** Blister diameter changes as a function of curing temperature

| Curing temperature | Room temperature | 50 °C | 100 °C |
|---|---|---|---|
| (db/dt) mm/hrs "polarized samples" | $6.15x10^{-3}$ | $4.3x10^{-3}$ | $5.3x10^{-3}$ |
| (db/dt) mm/hrs "not polarized samples" | $6.06x10^{-3}$ | $1.2x10^{-3}$ | * |

*No blisters appeared; the diameter of the defect increased gradually.

Based on the given information, it seems that Table 5 shows the rate of change in the average size of blisters for polarized samples. This suggests that the rate does not depend on the curing temperature. It appears that Fig. 4 visually represents the initial blister sizes for samples cured at different temperatures. The initial blister diameter is lower at room temperature than at 100°C. Samples cured at 50°C display intermediate diameter.

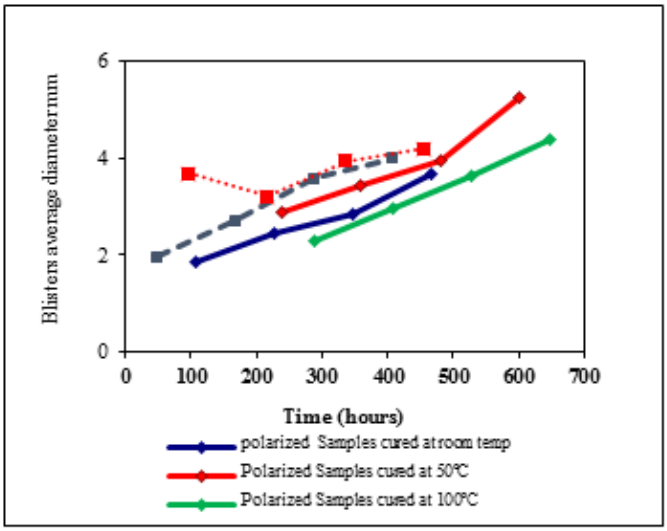


**Figure (4).** Blisters' average diameter as a function of time

This observation highlights that while the rate of change in blister diameter over time may not be directly associated with curing temperatures in polarized samples, the initial blister diameter does exhibit variation concerning curing temperatures. According to the trend observed, the samples cured at room temperature show the lowest initial blister diameter, followed by those cured at 100 °C, and then by samples cured at 50 °C. This distinction emphasizes the potential impact of curing temperature on the initial development or formation of blisters in the experimental setup. The information provided shows stimulating observations regarding the blister diameter changes in curing temperature and polarization status. Samples cured at room temperature and in an open circuit system exhibit a faster blister diameter increase than samples cured at 50 °C. Fig. 4 shows that samples cured at 50 °C have a larger average blister diameter than those cured at room temperature and in an open circuit.

The size of blisters, the rate of change, and polarization status have intricate relationships with curing temperature. Blister diameter changes and initial diameters vary between samples cured

at different temperatures and under varying polarization, indicating the complexity of factors influencing blister formation and growth. Based on the description in Fig. 4, there are noticeable differences in the initial blister average diameter between polarized samples cured at room temperature and those cured in an open circuit system. The graph displays encouraging patterns in the evolution of blister diameters as time passes. Samples treated with polarized curing at room temperature demonstrate an initial average blister diameter smaller than the samples in an open circuit system. It's important to note that blister diameters behave differently over time. After approximately 288 hours, the average blister diameter stabilizes or reaches a steady state in an open circuit system. However, for polarized samples, the average blister diameter continues to increase beyond 348 hours.

These observations suggest that initial blister sizes differ between polarized samples cured at room temperature and those in an open circuit. However, there are also divergent trends in blister diameter behavior over time. This may suggest that the polarization status and curing temperature influence the initial sizes and the long-term behavior or growth patterns of blisters in the experimental setup. This observation emphasizes that although the rate of change in blister diameter over time might not be directly associated with curing temperatures in polarized samples, the initial blister diameter does showcase variation concerning curing temperatures. The data suggests that the size of initial blisters is smallest in samples cured at room temperature, followed by those cured at 100°C, and then by samples cured at 50°C. This observation indicates that curing temperature may impact the formation of blisters in the experiment. Based on the information provided, there are interesting findings regarding the changes in blister diameter related to curing temperature and polarization status. Samples cured at room temperature and in an open circuit system displayed a faster increase in blister diameter compared to samples cured at 50°C. Fig. 4 shows that samples cured at room temperature and in open circuit initially have a smaller average blister diameter than samples cured at 50°C.

These results indicate complex relationships between curing temperature, polarization status, rate of change, and initial blister sizes. The observed differences in blister diameter changes and initial diameters among samples cured at various temperatures and under different polarization statuses highlight the complexity of factors influencing blister formation and growth in this experimental context. Based on the information provided in the description of Figure 4, there seem to be significant variations in the average diameter of blisters at the beginning between the polarized samples cured at room temperature and the samples in an open circuit system. The figure also depicts encouraging patterns in how these blister diameters change over time. Polarized samples cured at room temperature display a smaller initial average blister diameter compared to samples in open circuit systems. Notably, there is a difference in blister diameter behavior over time. In an open circuit system, the average blister diameter of samples usually reaches a steady state after about 288 hours. On the other hand, for polarized samples, the average blister diameter tends to keep increasing even after 348 hours. Upon curing at room temperature, polarized samples exhibit differences in initial blister sizes and varying trends in blister diameter behavior over time. This suggests that the polarization status and curing temperature affect the initial blister size and their long-term growth patterns in the experiment.

It seems that the samples cured at 50°C exhibit a behavior similar to those cured at room temperature, as shown in Fig. 4, concerning the trends in blister diameter. The key difference is the timing at which particular changes occur in these blister diameters. Blister average diameter behavior in polarized and open circuit systems for samples cured at 50°C follows a trend similar to that observed in room-temperature cured samples. However, there is a difference in the tim-

ing of significant changes. In samples with polarization, the average diameter of blisters tends to increase after being cured for 480 hours at 50°C. However, in samples with an open circuit system cured at the same temperature, the blister diameter reaches a steady state or plateau much earlier, at around 338 hours. This finding suggests that although the blister diameter behavior of samples cured at room temperature and 50°C may appear similar, the timing of crucial changes in blister growth or stabilization varies. This indicates that the curing temperature and polarization status may nuanced the blister evolution over time. After curing at 100°C and polarization, the samples were tested by immersing them in brine water. The results showed that blisters appeared after 288 hours of immersion.

The samples that were cured at room temperature and 50°C had larger blister diameters (compared to those cured at 100°C), and the average blister diameters increased steadily with an increase in immersion time. The most minor blister diameters observed were 2.2 $mm^2$. The samples that were cured at a temperature of 100°C with an open circuit and a sacrificial anode did not develop any blisters on their surface. In all cases, the initial blisters appeared near the defect and then spread to the rest of the sample. In summary, while mechanical and chemical processes can contribute to blister expansion, the experiment suggests hydrostatic pressure is the predominant driving force. It is believed that the consistent growth rates of blisters, regardless of polarization status, support the inference that regions at the interface have varying degrees of adhesion, ranging from good to poor. Likely, blisters form initially in areas where the adhesion is relatively weaker. This suggests that the degree of adhesion is a key factor in the formation of blisters. As blisters form in certain areas, the water that diffuses from existing blisters will open new blister sites. When the temperature reaches 100 C, the epoxy must be more cross-linked, and the adhesion should be improved. Furthermore, any residual solvent will be evaporated at this temperature. This explains the improvement in performance by reducing oxygen, water, and ion transport due to improved barrier properties.

## CONCLUSION

The current work's key conclusions can be presented as follows:

1. The initial blistering time significantly increases with higher curing temperatures in unprotected and protected samples.
2. Polarized samples consistently exhibit longer initial blistering times than non-protected samples at all curing temperatures.
3. Blister development rates increase with curing temperature for protected and non-protected samples.
4. The rate of change in blister number is higher for non-protected samples than protected ones at all curing temperatures. In protected samples, initial blister numbers decrease with higher curing temperatures, while blister numbers increase in nonprotected samples with increased curing temperature.
5. The rate of disbonding increases as the curing temperature rises for protected and unprotected samples. Unprotected samples show higher disbonding rates than protected samples. However, the disbonding rate for protected samples tends to increase to higher rates after a specific time.
6. The rate of blister diameter change is higher in protected samples than in unprotected samples.
7. Average blister diameter decreases with time in unprotected samples but increases in protected samples.

These conclusions demonstrate the intricate relationship among curing temperatures, polariza-

tion, and various factors that affect blistering, disbonding, and changes in blister diameter over time.

**Duality of interest:** The authors declare that they have no duality of interest associated with this manuscript.

**Author contributions:** Contribution is equal between authors.

**Funding:** No specific funding was received for this work.

## REFERENCES

Agwa, O., Iyalla, D., & Abu, G. (2017). Inhibition of bio corrosion of steel coupon by sulphate reducing bacteria and Iron oxidizing bacteria using Aloe Vera (Aloe barbadensis) extracts. *Journal of Applied Sciences and Environmental Management, 21*(5), 833-838.

Ashassi-Sorkhabi, H., Moradi-Haghighi, M., Zarrini, G., & Javaherdashti, R. (2012). Corrosion behavior of carbon steel in the presence of two novel iron-oxidizing bacteria isolated from sewage treatment plants. *Biodegradation, 23*, 69-79.

Babić, R., & Metikoš-Huković, M. (1993). Oxygen reduction on stainless steel. *Journal of applied electrochemistry, 23*, 352-357.

Chen, X., Li, X., Du, C., & Cheng, Y. (2009). Effect of cathodic protection on corrosion of pipeline steel under disbonded coating. *Corrosion Science, 51*(9), 2242-2245.

Cheng, X., Fu, M., Dou, W., Chen, S., & Liu, G. (2023). Accelerated degradation of cathodic protected epoxy coating by Pseudomonas aeruginosa in seawater. *Construction and Building Materials, 408*, 133640.

Esquivel, R. G., Olivares, G. Z., Gayosso, M. H., & Trejo, A. G. (2011). Cathodic protection of XL 52 steel under the influence of sulfate reducing bacteria. *Materials and Corrosion, 62*(1), 61-67.

Eyckens, D. J., Demir, B., Randall, J. D., Gengenbach, T. R., Servinis, L., Walsh, T. R., & Henderson, L. C. (2020). Using molecular entanglement as a strategy to enhance carbon fiber-epoxy composite interfaces. *Composites Science and Technology, 196*, 108225.

Gaylarde, C., Morton, L., Loh, K., & Shirakawa, M. (2011). Biodeterioration of external architectural paint films–a review. *International Biodeterioration & Biodegradation, 65*(8), 1189-1198.

Hammond, J., Holubka, J., DeVries, J., & Dickie, R. (1981). The application of x-ray photo-electron spectroscopy to a study of interfacial composition in corrosion-induced paint de-adhesion. *Corrosion Science, 21*(3), 239-253.

Jovancicevic, V., & Bockris, J. M. (1986). The mechanism of oxygen reduction on iron in neutral solutions. *Journal of the Electrochemical Society, 133*(9), 1797.

Knudsen, O. Ø., & Forsgren, A. (2017). *Corrosion control through organic coatings*: CRC press.

Koehler, E. (1984). The mechanism of cathodic disbondment of protective organic coatings—aqueous displacement at elevated pH. *Corrosion, 40*(1), 5-8.

Kumar, V., & Bhattacharya, A. (2020). Demand for Low-VOC Coatings Continues to Rise. *Paint & Coatings Industry*.

LeBozec, N., Thierry, D., & Pelissier, K. (2018). A new accelerated corrosion test for marine paint systems used for ship's topsides and superstructures. *Materials and Corrosion, 69*(4), 447-459.

Leidheiser, H. (1981). Corrosion control by organic coatings.

Leidheiser, H., & Funke, W. (1987). Water disbondment and wet adhesion of organic coatings on metals: A review and interpretation. *Journal of the Oil and Colour Chemists' Association, 70*(5), 121-132.

Leidheiser Jr, H., Wang, W., & Igetoft, L. (1983). The mechanism for the cathodic delamination of organic coatings from a metal surface. *Progress in Organic Coatings, 11*(1), 19-40.

Leng, A., Streckel, H., & Stratmann, M. (1998). The delamination of polymeric coatings from steel. Part 2: First stage of delamination, effect of type and concentration of cations on delamination, chemical analysis of the interface. *Corrosion Science, 41*(3), 579-597.

Ma, I. W., Ammar, S., Kumar, S. S., Ramesh, K., & Ramesh, S. (2022). A concise review on corrosion inhibitors: types, mechanisms and electrochemical evaluation studies. *Journal of Coatings Technology and Research*, 1-28.

Njoku, D. I., Cui, M., Xiao, H., Shang, B., & Li, Y. (2017). Understanding the anticorrosive protective mechanisms of modified epoxy coatings with improved barrier, active and self-healing functionalities: EIS and spectroscopic techniques. *Scientific reports, 7*(1), 15597.

Qian, S., & Cheng, Y. F. (2018). Degradation of fusion bonded epoxy pipeline coatings in the presence of direct current interference. *Progress in Organic Coatings, 120*, 79-87.

Ramezanzadeh, M., Bahlakeh, G., Ramezanzadeh, B., & Rostami, M. (2019). Mild steel surface eco-friendly treatment by Neodymium-based nanofilm for fusion bonded epoxy coating anti-corrosion/adhesion properties enhancement in simulated seawater. *Journal of Industrial and Engineering Chemistry, 72*, 474-490.

Rozenfel'd, I., Rubinshtein, F., & Zhygalova, K. (1987). Corrosion Protection of Metals by Paint Coatings: Khimiya, Moscow.

Sato, Y. (1981). Mechanism and evaluation of protective properties of paints. *Progress in Organic Coatings, 9*(1), 85-104.

Schwenk, W. (1981). Corrosion Control by Organic Coatings. *Adhesion Loss of Organic Coatings—Causes and Consequences for Corrosion Protection*, 103.

Shi, L., Song, G., Li, P., Li, X., Pan, D., Huang, Y., . . . Guo, Z. (2021). Enhancing interfacial performance of epoxy resin composites via in-situ nucleophilic addition polymerization

modification of carbon fibers with hyperbranched polyimidazole. *Composites Science and Technology, 201*, 108522.

Thierry, D. (2020). Powder and High-Solid Coatings as Anticorrosive Solutions for Marine and Offshore Applications? A Review. *Coatings, 10*(10), 916.

Tsay, K. (1988). *The failure of organic coatings during cathodic protection.* University of Manchester.

Yu, M., Fan, C., Ge, F., Lu, Q., Wang, X., & Cui, Z. (2021). Anticorrosion behavior of organic offshore coating systems in UV, salt spray and low temperature alternation simulated Arctic offshore environment. *Materials Today Communications*, *28*, 102545.

Zhang, F., Ju, P., Pan, M., Zhang, D., Huang, Y., Li, G., & Li, X. (2018). Self-healing mechanisms in smart protective coatings: A review. *Corrosion Science*, *144*, 74-88.

Zhu, D., & Van Ooij, W. J. (2002). Structural characterization of bis-[triethoxysilylpropyl] tetrasulfide and bis-[trimethoxysilylpropyl] amine silanes by Fourier-transform infrared spectroscopy and electrochemical impedance spectroscopy. *Journal of adhesion science and technology*, *16*(9), 1235-1260.

Al-Mukhtar Journal of Sciences 08 (1): 65-74, 2024
Doi: https://doi.org/10.54172/1jpfs115

Research Article Open Access

# Robust Detection Technique in Cooperative Radio Networks

**Mahmoud Ali Ammar[1], Abderazag Masoud[2] and Ali F. kaeib[3]**

**Corresponding author:** M.ammar@zu.edu.ly, Department of Computer, Faculty of Computer Technology University of Zawia, Libya

[2, 3] Department of Computer, Faculty of Computer Technology, University of Zawia, Libya

**Received:**
21 September 2024

**Accepted:**
05 December 2024

**Publish online:**
31 December 2024

**Abstract**
Traditional spectrum management reserves most of the spectrum for licensed users with exclusive access. To address spectrum scarcity, it is crucial to explore unlicensed operations in licensed bands so the interference between the Primary Users (PU) and Secondary Users (SU) is prevented. The success of Cognitive Radio (CR) networks depends on robust security measures to avoid misuse and to ensure trust among nodes, requiring mechanisms to distinguish primary from secondary user signals. While secondary users enhance spectrum utilization by sensing and accessing available frequencies, this capability introduces security risks. Malicious users can exploit the system to disrupt operations and degrade frequency determination performance. To mitigate these issues, the proposed scheme integrates advanced security measures based on trust and weight values to ensure secure spectrum access. It evaluated the trustworthiness of each SU using location coordinates and received signal strength. SUs performs independent frequency determination and submit data to a Fusion Center (FC) The FC combines local sensing results with trust weights and applies some rules to detect primary user presence reliably. A Limited Threshold Range (LTR) mechanism is proposed to minimize the impact of low-trust users by reducing their influence on decision-making. The LTR ensures that users from the threshold value contribute less to the decision and the visa-versa. This approach leads to enhancing decision accuracy.

**Keywords:** Cognitive Radio, Primary Users, Secondary Users, Primary User Emulation Attack , Cooperative Spectrum Sensing, Frequency Determination, Fusion Center.

## INTRODUCTION

Frequency determination and sharing free bands are crucial functions of cognitive radio that allow secondary nodes to access the free bands and to identify available spectrums to be occupied (Chen & Park, 2006). Along with these capabilities, addressing the security and reliability challenges within cognitive radio networks is essential. One example of cognitive radio application is using unused spectrum (often referred to as white spaces) in television bands, where the television transmitter serves as the master node and the TV frequency is used by the secondary users.

In a cognitive radio network, users are divided into two groups; group one is for the primary nodes, while the other is for the secondary nodes. The main purpose of frequency determination in such networks is to detect unused spectral frequencies, also referred to as "white spaces," to be used by

the cognitive radio nodes (Letaief & Zhang, 2009). In this step, the legitimate nodes have the chance to use the spectrum, while the other nodes must relinquish their turn of the spectrum if primary users need it with no interference occurring.

If a node starts transmitting on a frequency used by another secondary node, the secondary node is expected to leave the frequency quickly. However, when no primary user is actively communicating, all other users are permitted to access the unoccupied spectrum. In some cases, secondary users may attempt to copy the primary node information to have unauthorized access to the spectrum. This can lead to malicious behavior where secondary users are mistaken for primary users, causing other secondary users to vacate the spectrum for the malicious actor (Letaief & Zhang, 2009). A PUEA occurs when a lousy node uses the details of the signal of a primary node to occupy idle channels, thereby obstructing access to the spectrum. Such attacks can create significant problems in cognitive radio networks. PUEA can be initiated during frequency determination through various detection methods, including cyclostationary, energy, or matched filter detection techniques (Hossain & Bhargava, 2007). Among these, the based method is the most widely used.

This research proposes a Limited Threshold Range (LTR) approach to combat PUEA. The idea behind LTR is that the farther away a user is from the threshold, the more likely the correct decision is made. This technique helps prevent low-trust users from influencing the decision-making process regarding the PU and SU in the network.

Cooperative frequency determination can be employed to address the uncertainty inherent in frequency determination within CRN. Several techniques for cooperative frequency determination have been used. The simplest approach involves using OR or AND operations on the sensing results from multiple nodes. For another example, the maximal ratio combination has been explored (Simon & Alouini, 2005). A cooperation using a Likelihood Ratio Test was suggested by (Digham et al., 2003). (Ghasemi & Sousa, 2007) proposed a sensor technique for cooperative frequency determination to save energy, and (Akyildiz et al., 2011) suggested using fuzzy logic. However, a trust cooperative frequency determination method using a majority rule is introduced in our proposed scheme for CRN. In this approach, individual users conclude the local result about the PU status; thus, a Fusion Center concludes the overall result about the PU presence. This scheme enhances sensing accuracy while conserving the energy of the nodes.

This work is based on two stages which are:

**Stage 1: Conventional technique for Detection**

Advanced techniques such as cooperative sensing, authentication-based schemes, machine learning, and cryptographic methods are used to counter PUE attacks and enhance detection and resilience. Cooperative frequency determination further supports identifying and mitigating PUE attacks for secure Cognitive Radio Network (CRN) operations. In this section, we explain the conventional mechanism for detecting PUEA.

**The conventional technique for PUEA**

In the conventional algorithms of PUEA Detection, the source of the spectrum information is validated as depicted in Figure 1 below. The key aspect of this method is its ability to verify the authenticity of a signal source based on its location. If the calculated distance, determined by two different techniques, matches, the user is considered trustworthy. Conversely, if there is a distance discrepancy, the user is deemed malicious.

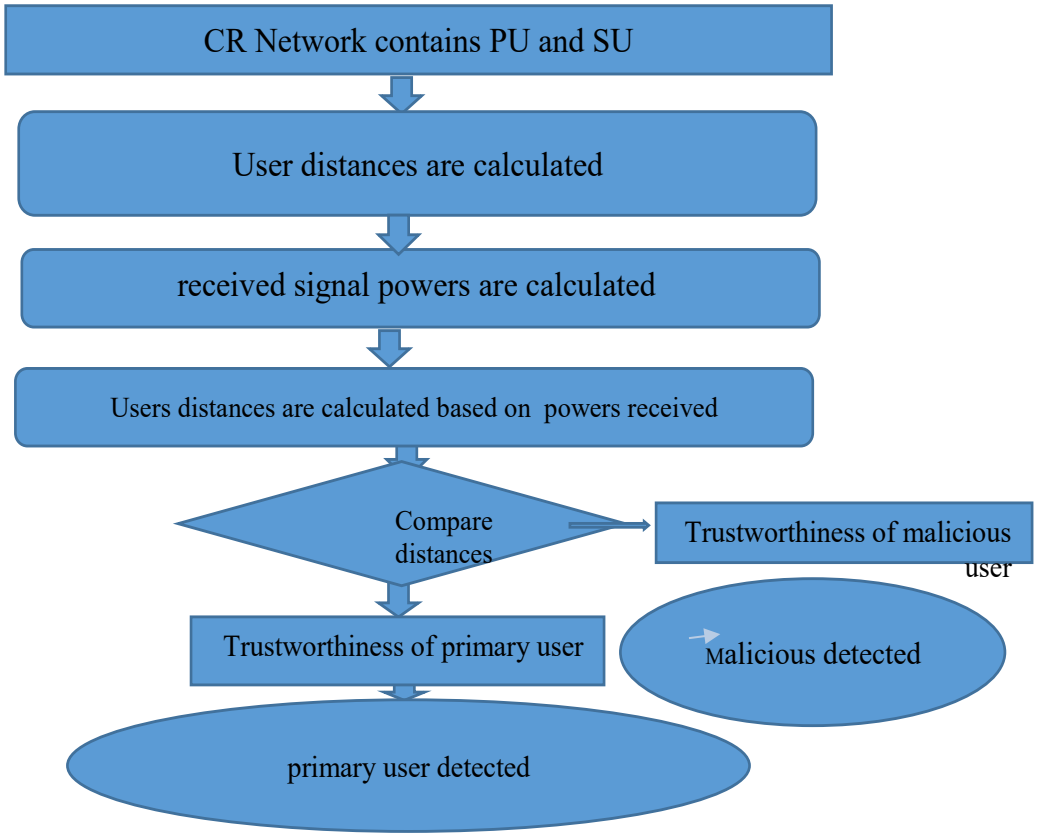


**Figure (1).** The conventional Technique for PUEA Detection

The cognitive radio (CR) network follows a specific set of steps, with one key condition: if the calculated distances match, the signal source is considered legitimate. If the distances do not align, the transmitter is regarded as unauthorized.

**Using users' locations**

The nodes distance Y is computed based on their geographical coordinates. For example, if (A, B) are the points of user location and (C, D) are the points of the primary user, a

$$Y= ( (A-C)^2+(B-D)^2 )^{1/2} \quad * \qquad (1)$$

In this work, it is assumed that all nodes (primary and secondary users) broadcast their location coordinates to be used in the calculation.

**Using signal power**

The concept of measuring distance based on received signal strength (RSS) or received power is grounded in the assumption that received power is related to both the transmitting power and the distance between the two radio devices. The distance between a secondary user and another device can be estimated by measuring the received signal power and knowing the transmit power level. The received power $P_r$ with a given transmit power $P_t$ is described by:

$$P_r = \frac{P_t G_t G_r h_t^2 h_r^2}{d^4 L} \quad * \qquad (2)$$

$G_t$ and Gr = gain of the signal , $h_t$, $h_r$ = the transmitter and receiver length , L= loss factor It's considered that all variables above in equation 2 are assumed to be 1 except Pr , $P_t$ and d , so $P_r$ is .

$$P_r = \frac{P_t}{d^4} \quad * \tag{3}$$

$$D = \sqrt[4]{\frac{P_t}{P_r}} \quad * \tag{4}$$

While this method provides an estimate, it is not always accurate due to noise and channel impairments and uncertainties in the signal propagation environment. Despite these limitations, many researchers still favor this approach due to its effectiveness.

**Received Signals:**
$P_r$ is considered to be without noise is calculated by:

$$( P_r = P_t / d^4 ) * \tag{5}$$

If the noise is considered, then the power $p_r$ is determined by:

$$( P_r = (P_t + \text{noise}) / d^4 ) * \tag{6}$$

**Nodes Authentication**
In this method, a malicious user cannot simultaneously mimic the primary user's coordinates and power level. Consider two distances: d1 is calculated from location coordinates, and d2 is calculated from the received power level. The relative trustworthiness Z of the user is calculated as:

$$Z = \text{Minimum of } (d1/d2 \ , d2/d1) * \tag{7}$$

If both distances match, the user is deemed trustworthy; otherwise, the user is considered malicious. Due to noise, the distance based on received power might not be 100% accurate, but both methods should yield similar results statistically. Trustworthy users will have a trust value close to 1, while untrustworthy users will have lower values.

**Stage 2: Proposed algorithm based on the Limited Threshold Range LTR of users trust**
Unlike traditional wireless networks, ensuring reliable frequency determination in (CRNs) is crucial for practical deployment. Secondary users (SUs) must accurately detect primary users (PUs) across a wide spectrum with minimal wrong acts. Because the nodes use many modulation methods, it is not easy to detect such acts (Unnikrishnan & Veeravalli, 2008). Energy detection is often chosen when secondary users have limited information about the PU signal because it is simple and computationally inexpensive. However, energy detection can be degraded by issues like (SNR) limitations.

Secondary nodes can work together to improve network outcomes. Cooperative frequency determination is strong to significantly improve the primary users detections (Mishra et al., 2006).

**Trust Factor and Limited Threshold Range (LTR)**
An SU is allocated with a trust value; if these values are high, it indicates a greater likelihood that the user is legitimate. Users with high trust values are allowed to have more control over the fusion center decision. Unlike conventional cooperative sensing approaches, the proposed method uses a Limited Threshold Range (LTR) for user trust values. This approach enhances network security by distinguishing between legitimate and malicious users. When a user's trust value falls outside the

acceptable range, the Fusion Center excludes that user from contributing to the final decision. The Fusion Center stores the trust values and ensures that suspicious users are excluded from the final decision process. In cases where a collision occurs between a PU and an SU, the PU system is compensated, and the exclusion procedure is applied to the SU system (Ganesan & Li, 2007). If a collision happens and all SUs follow the controller's spectrum-access policy, they will share the penalty. However, if a specific SU violates the policy, the penalty will be applied solely to that user.

The design of the LTR algorithm directly improves detection by using only the appropriate data needed to make the correct decision while ignoring suspected data collected from malicious users. The FC design provides data that strongly supports the research hypothesis. The sampling method is generalized and large data samples are conducted to improve the reliability.

**Mechanism of the Cooperative Frequency Determination**

We describe the scenario of cooperative frequency determination in (CRNs) and discuss the impact of trust weights and majority rule.

**Local Frequency Determination**

A CRN is assumed to consist of a primary user, n secondary users, and a Fusion Center; as Figure 2 below explains, each CRN node uses energy detection to sense the spectrum. The hypotheses for whether a PU ($H_1$) or there is no PU ($H_0$) :

$$\text{If } X_i(t) = N_i(t) \text{ then } H_o, \text{ or if } X_i(t) = S(t) + N_i(t) \text{ then } H_1 * \quad (8)$$

$$x_{Ei} = \sum_{k=0}^{N-1} |x_i(k)|^2 \quad , i = 1,2,...,M \quad * \quad (9)$$

$X_i(t)$= Received signal for the $i^{th}$ user, $X_{EI}$= Energy detection Statics at the user i, N= added noise, S is the received signal , M= Users number , N=Samples number , $X_i(k)$= Sample $K^{th}$ of the Received Signal at $i^{th}$ user ,

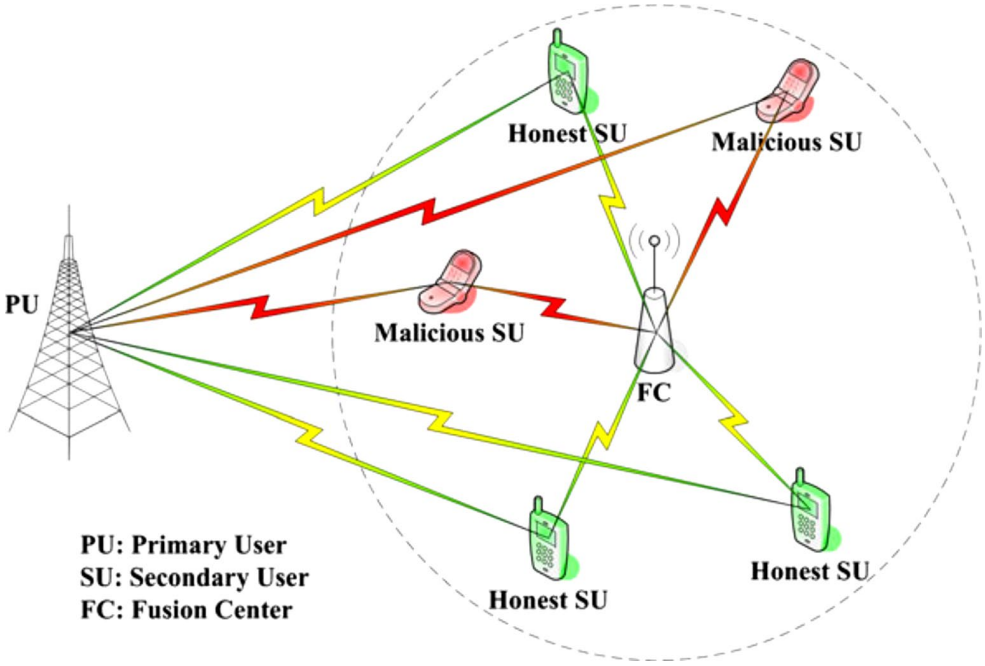


**Figure (2).** Scenario model of cooperative frequency determination

The decision $Ld_i$ is for the i user. $Ld_i$ =1 primary user is found ($H_1$), while $Ld_i$=0 there is no PU ($H_0$). The energy detection value $x_{Ei}$ and $H_0$ and $H_1$, and is expressed as:

$$\begin{cases} x_{Ei} \cong N(\mu_{0i}, \sigma_{0i}^2) & H_0 \\ x_{Ei} \cong N(\mu_{1i}, \sigma_{1i}^2) & H_1 \end{cases}^* \quad (10)$$

$\sigma_{0i}^2$ , $\sigma_{1i}^2$ represents the variances of $H_0$ and $H_1$

**LTR Approach**

The proposed mechanism enhances frequency determination by utilizing a Limit-Based Trusted Reputation (LTR) method. Unlike traditional majority-based methods that rely solely on the number of users, this model incorporates user reputation scores to make decisions. The key principle is leveraging the input of highly trusted nodes to ensure accuracy and mitigate the influence of malicious or unreliable users.

This approach assigns different weights to nodes based on the assigned score: highly reliable nodes are given greater influence, while unreliable nodes are assigned lower values. Reputation scores, determined by observing behavioral patterns, distinguish between users exceeding a predefined reputation threshold and those deemed reliable, contributing more significantly to the decision-making process. By reducing the impact of unreliable nodes, this scheme improves decision robustness. The algorithm effectively counters the shortcomings of traditional methods, offering a flexible and efficient solution for distributed cooperative frequency determination.

We have added extra security procedures by considering the LTR in addition to the reputation of the user; the central concept of this LTR is that the further away and avoiding being close to the LTR and despite the increase in low-trust users, the more the decision is correct.

**LTR Mechanism:** The Mechanism of the Proposed LTR Approach is as follows:

λ1, λ2 the lower and upper limit of the range of the Threshold

If User_Reputation $R_i$<= λ1 and $R_i$ >= λ2

then

$$\left( \text{final\_decision} = \begin{cases} H_1 : \sum_{i=1}^{N} Ld_i R_i > 0 \\ H_0 \quad otherwise \end{cases} \right)$$

When $R_i$= Node i Reputation, Ldi = Node i decision

**RESULTS DISCUSSION**

Monte Carlo simulations were conducted using 50,000 samples across varying SNRs to assess the LTR approach. The simulations were run with different numbers of CRN nodes, and Matlab was used to simulate and verify the algorithm. To understand the influence of system parameters on the LTR scheme, the simulations incorporated different penalty factors, with SNR values ranging from -10 to 50 in increments of 5.

(i.e.,-10, -5, 0, 5, 10, 15, 20, 25, 30, 35, 40, 45, 50). As shown in Figure 3 below, the simulation results illustrate the LTR scheme as the number of malicious nodes increases, with varying numbers

of trustworthy users. First, we will examine the outcomes of the conventional majority rule to compare it with the proposed LTR-based method.

**Result of the Conventional Mechanism**

The mechanisms were simulated with different numbers of reasonable, legitimate, and unreliable nodes to compare both the conventional mechanism rule and the reputation score mechanism. The conventional majority scheme, as shown in Figure 3, operates without assigning reputation values and relies on the number of nodes of the sensing process. The results examine how the number of nodes influences the correct range, taking into account changes in the number of illegitimate nodes.

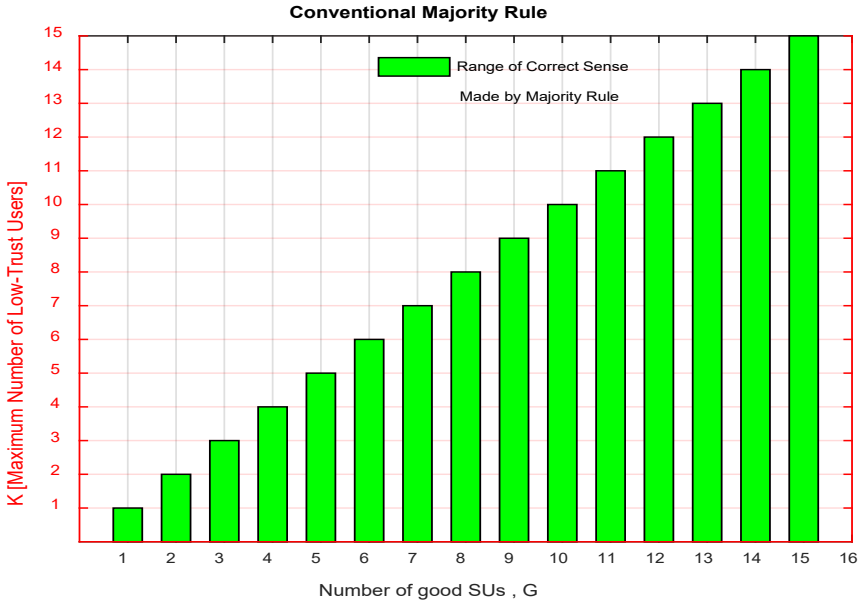


**Figure (3).** Range of correct sense for different G and K

Figure 3 above is the result of the majority mechanism. For instance, If the number of malicious nodes = 8, then a robust detection is possible only if the bad nodes number <=8. i.e., 50% rule.

**Results of LTR Mechanism**

The nodes reputation values and the LTR boundary are used. If the malicious nodes number outcomes the good SU nodes, then a corrected detection is still possible.

First, as shown in Figure 4, the good and malicious nodes reputations are set to 0.8 and 0.3, respectively, and The LTR boundaries are set to $\lambda1=0.4$ $\lambda2= 0.6$. It is noticeable that ten secondary nodes out of 37 nodes are found. This means at least 27% of good users can make a correct decision. The LTR rule is evaluated and simulated by considering the model when the number of nodes M is 34, as explained with the orange bar in Figure 4.

The result in Figure 5 below is obtained when the LTR values are set to ($\lambda1=0.4$ and $\lambda2=0.6$), which means all users whose trust values are in this range are excluded from the decision-making rule.

First, the scheme is evaluated with $\alpha =0.7$ and $\lambda1=0.4$, $\lambda2=0.6$, and it is assumed that the network consists of 34 users with a variant number of low-trust users (malicious users). Figure 5 shows that the correct decision is made when the ratio of low-trust users is up to 0.65, i.e., more than 0.65 of malicious users in the cooperative radio network will lead to a wrong detection.

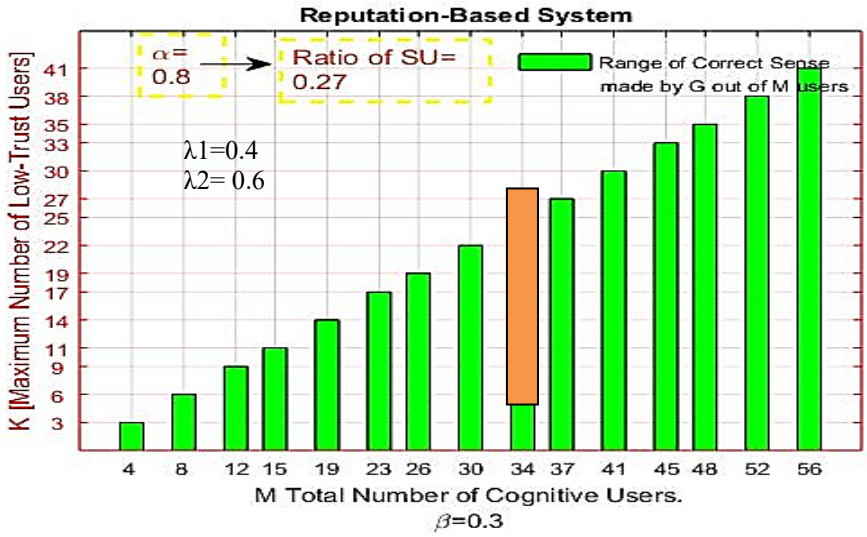


**Figure(4)** Reputation System

In comparison with the results obtained by (Letaief & Zhang, 2009), our results outperform theirs in terms of the number of users required to make the correct decision.

Secondly, the scheme is evaluated with α =0.8 and λ1=0.4, λ2=0.6, i.e. the users trust value is changed and set farther from the LTR values. It is noticed that from Figure 5. The correct decision is made even when the ratio of low-trust users is up to 0.71, i.e. increasing the good users trust value makes the network able to tolerate the presence of up to 0.71 of malicious users in the cooperative radio network, more than that ratio of malicious users will also lead to a wrong decision.

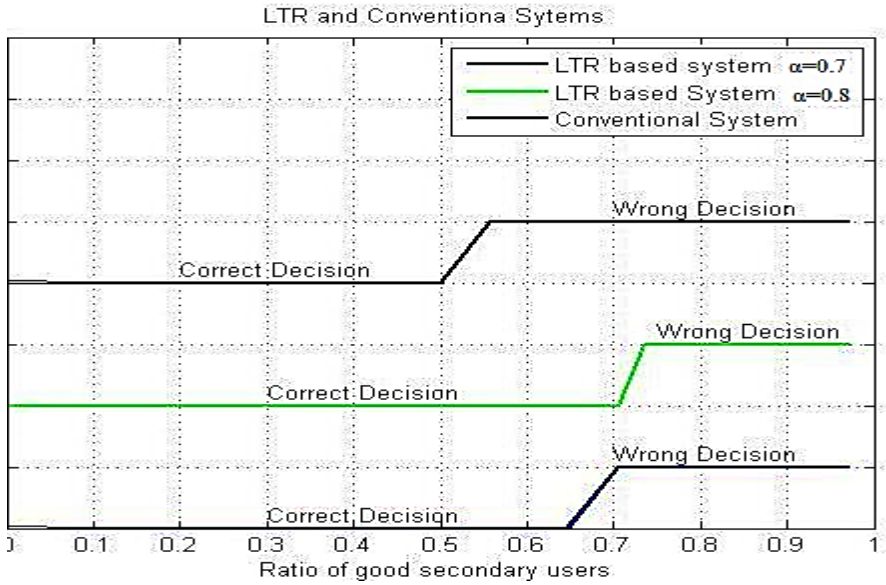


**Figure (5).** Proposed LTR Scheme

The conventional scheme could only tolerate up to 50% of malicious users. As shown in Figure 5 above i.e., more than 50% of malicious users will lead to a wrong decision according to the conventional scheme.

## CONCLUSION

The Limited Threshold Range (LTR)--based cooperative frequency determination approach offers an effective mechanism for the challenges of the limited spectrum. reallocating the spectrum to secondary users without causing interference with primary users. by utilizing cooperative frequency determination, the overall efficiency of spectrum usage can be significantly enhanced. However, secondary users must ensure the reliability and legitimacy of the spectrum occupancy information they rely on. To address this concern, we have proposed schemes incorporating reputation-based mechanisms and penalties to ensure secure access to the spectrum in cognitive radio networks.

In this work, each node independently determines frequency and forwards its local sensing data to a primary central node. The schemes effectively minimize the influence of low-reputation users while enhancing the contribution of high-reputation users.

The LTR scheme improves the performance of cooperative frequency determination, even in networks with varying numbers of trustworthy and unreliable users. The scheme significantly enhances decision accuracy by excluding low-trust users from the decision-making process. Simulation outcomes show that the LTR scheme outperforms the traditional majority-based approach.

### Future Research Directions

The proposed scheme can be refined through practical, experimental, and laboratory testing. Future developments could focus on the following directions:

- **Distributed Frequency determination (DSS):** Incorporating DSS to detect primary nodes accurately.
- **Evaluation of RSSI-Based Transmitter Identification using USRP:** To defend against Primary User Emulation Attacks (PUEA) experimentally, we suggest conducting hardware experiments with software-defined radio (SDR). A transmitter identification method based on a Received Signal Strength Indicator (RSSI) at varying frequencies could be used to identify transmitters at different locations. The method can be validated in indoor environments using USRP devices.

**Duality of interest:** The authors declare that they have no duality of interest associated with this manuscript.

**Author contributions:** Contribution is equal between authors.

**Funding:** No specific funding was received for this work.

## REFERENCES

Akyildiz, I. F., Lo, B. F., & Balakrishnan, R. (2011). Cooperative spectrum sensing in cognitive radio networks: A survey. *Physical communication, 4*(1), 40-62.

Chen, R., & Park, J.-M. (2006). Ensuring trustworthy spectrum sensing in cognitive radio networks. 2006 1st IEEE Workshop on Networking Technologies for Software Defined Radio Networks,

Digham, F. F., Alouini, M.-S., & Simon, M. K. (2003). On the energy detection of unknown signals over fading channels. IEEE International Conference on Communications, 2003. ICC'03.,

Ganesan, G., & Li, Y. (2007). Cooperative spectrum sensing in cognitive radio, part II: multiuser networks. *IEEE Transactions on wireless communications, 6*(6), 2214-2222.

Ghasemi, A., & Sousa, E. S. (2007). Opportunistic spectrum access in fading channels through collaborative sensing. *J. Commun., 2*(2), 71-82.

Hossain, E., & Bhargava, V. K. (2007). *Cognitive wireless communication networks*. Springer Science & Business Media.

Letaief, K. B., & Zhang, W. (2009). Cooperative communications for cognitive radio networks. *Proceedings of the IEEE, 97*(5), 878-893.

Mishra, S. M., Sahai, A., & Brodersen, R. W. (2006). Cooperative sensing among cognitive radios. 2006 IEEE International conference on communications,

Simon, M. K., & Alouini, M.-S. (2005). Digital Communication over Fading Channels, John Wiley & Sons. *Inc., Publication*.

Unnikrishnan, J., & Veeravalli, V. V. (2008). Cooperative sensing for primary detection in cognitive radio. *IEEE Journal of selected topics in signal processing, 2*(1), 18-27.